

**TALKACTIVE CONTROL OF A DIFFRACTION GRATING  
INTERFEROMETER FOR MICROSCALE DEVICES**

A Thesis Presented to

The Academic Faculty

By

Michael C. Schmittiel

In Partial Fulfillment of the Requirements for the Degree

Master of Science in Mechanical Engineering

Georgia Institute of Technology

June, 2004

**ACTIVE CONTROL OF A DIFFRACTION GRATING INTERFEROMETER  
FOR MICROSCALE DEVICES**

Approved:

Dr. Thomas R. Kurfess, Chair

Dr. F. Levent Degertekin

Dr. William P. King

07/12/2004

## ACKNOWLEDGEMENTS

First and foremost, I would like to thank my primary advisor, Professor Thomas Kurfess for allowing me to join his lab group here at Georgia Tech and perform the work presented in this thesis. I would also like to thank Professor Levent Degertekin for his indispensable technical expertise and assistance with the work done toward this thesis. I would like to thank the final member of the thesis reading committee, Professor William King, for agreeing to be a member of the committee and giving me feedback on my work.

A number of students helped me perform this work. Special recognition must go to Dr. Byungki Kim, who worked in conjunction with me on this project. Also, I would like to thank Ryan Krauss for his assistance with the controls aspect of this work, and Guclu Onoran for this help with the analog electronics used in this project. I would like to acknowledge my office mates and lab mates in Professor Kurfess's and Professor Degertekin's lab groups for their help and advice on this project.

I would like to acknowledge my friends and family for their support and kindness towards me during my time working on this thesis. Without their motivation, producing the work presented in this document would have been much more difficult, if not impossible.

The author would like to take this opportunity to thank the engineers at National Instruments for their contributions to this research. This work was partially funded by the National Science Foundation under Grant Number DMI-0200331. The government has certain rights in this material. Any opinions, findings and conclusions or recommendations are those of the

authors and do not necessarily reflect the views of the National Science Foundation or National Instruments.



## TABLE OF CONTENTS

<b>ACKNOWLEDGEMENTS .....</b>	<b>III</b>
<b>TABLE OF CONTENTS .....</b>	<b>V</b>
<b>LIST OF FIGURES .....</b>	<b>VIII</b>
<b>LIST OF TABLES .....</b>	<b>XII</b>
<b>SUMMARY .....</b>	<b>XIII</b>
<b>CHAPTER I - INTRODUCTION .....</b>	<b>1</b>
Microscale Engineering .....	1
Motivation and Project Objective .....	3
<b>CHAPTER II - BACKGROUND AND LITERATURE REVIEW .....</b>	<b>5</b>
Contact Metrology Techniques .....	5
Non-Contact Metrology Techniques .....	8
Destructive Metrology Methods .....	13
Dynamic MEMS Metrology Techniques .....	14
<b>CHAPTER III - OPERATIONAL THEORY .....</b>	<b>18</b>
Optical Interferometry .....	18
Michelson Interferometer .....	19
Diffraction Grating Interferometer .....	22
<b>CHAPTER IV - CONTROL TECHNIQUE .....</b>	<b>27</b>
Analog Phase Locking Through Second Harmonic Monitoring .....	34

Tuning and Calibration of the Control System .....	38
Analytic Model .....	38
Experimental Validation of the Analytic Model.....	41
Controller Design.....	46
Controller Tuning.....	49
<b>CHAPTER V - EXPERIMENTAL SETUP AND PROCEDURES .....</b>	<b>55</b>
Hardware Setup.....	55
Sample and Micrograting Fixtures.....	56
Optical Setup.....	56
Software Setup .....	58
Motion Control.....	59
Data Acquisition .....	62
Control Software.....	66
Experimental Procedures .....	71
Focus Determination.....	71
Reflectivity Calibration.....	73
Sensor Specifications .....	74
Bandwidth.....	74
Signal to Noise Ratio (S/N) .....	76
Vertical (Out-of-Plane) Resolution.....	77
Horizontal (In-Plane) Resolution.....	79
<b>CHAPTER VI - CASE STUDY AND RESULTS .....</b>	<b>81</b>
Controller Results .....	81

Case Study - cMUT .....	85
Static Metrology of a cMUT .....	87
Optical Distortions in Imaging.....	90
Dynamic Metrology of a cMUT .....	92
Deformable Grating Sensor .....	101
Two Sensor Parallel Implementation.....	103
 <b>CHAPTER VII - CONCLUSIONS AND SUGGESTIONS FOR FUTURE WORK</b>	
<b>.....</b>	<b>106</b>
Summary .....	106
Conclusions.....	108
Recommendations and Future Work .....	110
 <b>APPENDIX A .....</b>	<b>112</b>
 <b>REFERENCES.....</b>	<b>114</b>

## LIST OF FIGURES

Figure 1. Schematic of an Atomic Force Microscope (AFM) .....	7
Figure 2. Schematic of a confocal laser microscope (Nichols, 2004) .....	9
Figure 3. Schematic of a white light interferometer (Shilling, 2003).....	12
Figure 4. Schematic of DVD Probe (Kirkland, 2002) .....	13
Figure 5. Principle of stroboscopic imagery .....	15
Figure 6. Laser doppler vibrometer schematic (Rembre, 2001) .....	17
Figure 7. Schematic of a Michelson interferometer.....	20
Figure 8. Constructive (a) and destructive (b) interference .....	21
Figure 9. Diagram of light refracted from a grating and a reflecting surface (Kim, 2003) .....	23
Figure 10. Location of the diffraction orders as from an example grating (Kim, 2003) ..	24
Figure 11. Interference curves for the first and second diffraction orders (Kim, 2004)...	25
Figure 12. Interference curve showing linear region .....	28
Figure 13. Interference curve showing the position modulation and optical intensity output .....	30
Figure 14. Light Intensity, 1 <sup>st</sup> Harmonic, and 2 <sup>nd</sup> Harmonic as a function of path difference .....	32
Figure 15. Negative (a) and positive (b) feedback within the linear regions of the 2 <sup>nd</sup> harmonic curve.....	33
Figure 16. Block diagram of an interferometer with a control system based on the lock-in technique (Graebner, 2000) .....	34
Figure 17. Schematic of the analog circuitry used for the second harmonic locking .....	35

Figure 18. Control system block diagram.....	36
Figure 19. FFTs of simulated photodetector, generated 2 <sup>nd</sup> harmonic, and multiplied signals showing convolution.....	37
Figure 20. Photograph of the experimental setup with axes labeled .....	39
Figure 21. Diagram of a mass, spring, damper mechanical system.....	40
Figure 22. Time series of a measured step response showing 2% tolerance band .....	42
Figure 23. FFT of a step response showing harmonic peaks.....	42
Figure 24. Bode plot of swept sine wave.....	44
Figure 25. Bode plot of the plant analytic model.....	45
Figure 26. Reduced control block diagram showing lumped sensor .....	46
Figure 27. Bode plot of the designed PI controller.....	47
Figure 28. Bode plot of the open-loop control system.....	48
Figure 29. Control tuning flowchart .....	51
Figure 30. Frequency spectrum of uncontrolled system.....	52
Figure 31. Optical table compliance graph (Melles Griot, 2004).....	56
Figure 32. Ray tracing of the laser beam through the optical system.....	57
Figure 33. Schematic of the grating and microlens setup.....	58
Figure 34. Raster (a) and overshoot (b) method of surface scanning .....	61
Figure 35. Surface scan showing backlash problem.....	61
Figure 36. Flowchart for LabVIEW scanning program.....	64
Figure 37. Screenshot of the block diagram of the LabVIEW scanning program.....	65
Figure 38. Screenshot of the user interface for the LabVIEW scanning program.....	65
Figure 39. Screenshot of the FPGA UI.....	67

Figure 40. Screenshot of the FPGA PID control block diagram .....	68
Figure 41. PID control flowchart.....	70
Figure 42. Screenshot of the PID sub function block diagram .....	70
Figure 43. Amplitude of the photodetector signal showing peak focus intensity.....	73
Figure 44. Interference curve (a) and a zoomed-in view of the linear region (b).....	78
Figure 45. Cross section of a metal trace showing horizontal resolution .....	80
Figure 46. Photodetector (a) and analog 2 <sup>nd</sup> harmonic (b) signals with process variable setpoint indicated .....	82
Figure 47. Analog 2 <sup>nd</sup> harmonic signal (a), computed 2 <sup>nd</sup> harmonic signal (b), and the MEMS displacement amplitude (c) over time with the controller on and with it off	84
Figure 48. SEM of a cMUT .....	85
Figure 49. Schematic of cMUT in cross section.....	86
Figure 50. Three-dimensional image of a cMUT taken with a white light interferometer	88
Figure 51. Two-dimensional cross section profile of a cMUT under 40V static actuation .....	88
Figure 52. Static height map of a cMUT generated with the actively controlled diffraction grating interferometer .....	89
Figure 53. Diagram of sensor and specimen showing multiple reflections.....	91
Figure 54. Vibration map of the surface of a cMUT .....	94
Figure 55. Vibration map of a cMUT actuated at the first fundamental vibration mode .	95
Figure 56. ANSYS finite element model of the cMUT membrane vibration amplitude at the first fundamental vibration mode.....	96

Figure 57. Vibration map of a cMUT actuated at the second fundamental vibration mode .....	96
Figure 58. ANSYS finite element model of the cMUT membrane vibration amplitude at the second fundamental vibration mode .....	97
Figure 59. Cross section of the vibration map of a cMUT activated at the second fundamental mode.....	98
Figure 60. Cross section of the vibration map of a cMUT activated at the first fundamental mode.....	98
Figure 61. Static height map of a cMUT showing the mechanical vibration ripples that appear with the controller inactive.....	100
Figure 62. Static height map of a cMUT with the controller active, showing the lack of mechanical vibration ripples .....	100
Figure 63. Static height map of a trace with the controller active (a) and inactive (b) showing the increase accuracy of the system under active control .....	101
Figure 64. Schematic of the deformable diffraction grating sensor with integrated photodiode (Kim, 2004).....	102
Figure 65. Gain response of the deformable grating sensor and actuator package.....	103
Figure 66. Screenshot of the LabVIEW block diagram of two parallel PID controllers implemented on the FPGA.....	104
Figure 67. Interference curve showing set point and modulation range.....	112

## LIST OF TABLES

Table 1. Summary of static microscale metrology techniques .....	14
Table 2. Performance of various gain parameters .....	53
Table 3. Specification comparison between the metrology system described in this thesis and a commercial stroboscopic white light interferometer .....	80
Table 4. Results of controlled and uncontrolled signals over 500 seconds .....	85



## SUMMARY

Over the last twenty years, the research field of microelectromechanical systems (MEMS) has grown exponentially. However, the adoption of MEMS devices in the marketplace has lagged significantly behind the research interest. One of the major barriers to the commercial usage of MEMS devices is the relatively low-yield, which limits the cost effectiveness of the devices. In order to increase the yield, research progress must be made in the fabrication technologies used to produce these MEMS devices. Currently, there exists a lack of suitable metrology tools for the three-dimensional analysis of microscale components. In particular, there is a dearth of technologies that can measure the mechanical motion of MEMS devices.

This thesis describes the creation of a metrology system based upon an actively controlled diffraction grating interferometer, which measures relative linear distances. The dynamics of this sensor are estimated based on experimental testing, and a suitable controller is designed to maintain the position of the sensor in the most sensitive operating region. This controller is implemented on a field programmable gate array (FPGA) processor, which allows for flexible programming and real-time control.

The sample under test is mounted atop a three axis linear stage system, which allows the diffraction grating interferometer to scan across the surface of the device, creating maps of the static and dynamic measurements. The controller is shown to maintain the sensitivity of the sensor during this operation. This insures all data are taken on the same scale, creating more accurate results. The controller increases the signal to noise ratio as compared to the system without the controller.

The specifications of the entire metrology system are detailed including the sensor and controller bandwidth, the vertical and horizontal resolution, and the signal to noise ratio. A case study utilizing a capacitive micromachined ultrasonic transducer (cMUT) is presented. The sensor generates static and dynamic displacement maps of the surface of this MEMS device. The controller improves these measurements by maintaining a position of high sensitivity during operation.

Finally, the preliminary results of a miniaturized version of this system are presented including the implementation of two fully independent parallel sensors. This allows for array implementation of these sensors, which is crucial for the batch fabrication photolithography techniques used to create many MEMS devices. Recommendations on the future work needed to complete the array implementation are given in conjunction with methods for increasing the resolution and robustness of the macroscale system described in this thesis.

# CHAPTER I

## INTRODUCTION

### **Microscale Engineering**

The feature size of mechanical devices has been steadily decreasing throughout the history. Recently, the field of microscale devices has been of particular research interest. These devices contain features approximately one hundred microns (100 $\mu$ m) to one micron in size. The ongoing miniaturization of technology allows for cheaper products with greater performance and increased functional flexibility. The late physicist Dr. Richard Feynman famously discussed this evolution of technology and the possibilities of microscale devices long before the advent of personal computers with his talk entitled: *There's Plenty of Room at the Bottom* (Feynman, 1996). In this lecture, he describes his vision of the future of technology, specifically discussing the many orders of magnitude between existing devices and the atomic scale. Future technology will continually push the size of features of electromechanical devices toward the atomic level. However, process control and analysis tools must be developed alongside these functional devices in order to increase the reliability, the function, and the economic viability of microscale devices. Specifically, the need for three dimensional metrology data is not being met, and in turn the low fabrication yields of microscale devices prohibit their adoption in the marketplace.

Much of the research in developing microscale technologies deals with the creation of processing and fabrication techniques for microscale devices. Silicon micromachining techniques derived from integrated circuit manufacturing processes,

such as the complimentary metal oxide semiconductor (CMOS) process, form the majority of the existing techniques to fabricate microscale devices. Although there are other novel methods of microscale manufacturing, such as embossing, mechanical cutting, and bulk deformation, photolithographic processes form the majority of manufacturing techniques for microscale devices. Photolithography is the process of creating three dimensional structures on a flat substrate through the deposition of different materials in specific patterns. The patterns are typically created through an etching process, which removes unwanted material. Photolithography is inherently a layered process and allows for massively parallel manufacture. Along with semiconductor devices which are purely electronic in nature, a wide range of electromechanical devices can be manufactured using this technique. Some examples of these devices are atomic force microscopy (AFM) cantilever arms, miniature acceleration sensors, and microscale stepper motors. These devices, dubbed microelectromechanical systems (MEMS), have a wide range of applications and represent a very active area of research.

A defining attribute of a MEMS actuator is mechanical motion via electrical stimulation. This motion can either be parallel to the plane of the substrate, such as the motion that occurs in the micromotor, or out-of-plane of the substrate, such as the motion of the AFM cantilever arm. In either case, in order to properly characterize the performance of a MEMS device, this motion must be quantified. Currently, there is a dearth of metrology techniques that can properly measure microscale devices. Furthermore, the out-of-plane motion of many MEMS devices necessitates that the metrology tools used must be able to generate measurement data in all three dimensions.

## **Motivation and Project Objective**

The capacitive micromachined ultrasonic transducer (cMUT) is the primary MEMS device that is studied by the metrology tool detailed in this thesis. These devices utilize the capacitive force generated between two parallel but oppositely charged electrodes to deflect a thin membrane. A cMUT can be used as either a sensor or an actuator, and their motion is of particular research interest in a variety of fields including medical devices and acoustic sensors. Therefore, a metrology tool that quickly and accurately measures the dynamic performance of cMUTs is necessary in order to refine the fabrication process and increase yield. Also, many MEMS devices are fabricated in array implementations, and an ideal metrology system should also be capable of array implementation in order to minimize inspection time. The use of this system for in-process metrology allows it to be integrated in the fabrication process, thereby giving immediate feedback and process control capability.

This thesis describes the creation of a measurement tool capable of detecting the out-of-plane motion of cMUTs and other MEMS devices with sub-nanometer precision and sensor bandwidth into the MHz range. This new metrology system utilizes a diffraction grating interferometry technique from a single wavelength source along with active feedback control to maintain a high measurement sensitivity level. A macroscale proof-of-concept system that shows the viability of the diffraction grating technique for dynamic measurements is introduced. Also, a microscale sensor capable of array implementation is demonstrated and two parallel sensors are demonstrated.

The significant aspects discussed in this thesis are the optical interferometry technique using a diffraction grating and microlens, the active control of the distance

between the sensor and the target in order to maintain a high sensitivity of measurement, and the case study of an existing MEMS device. Chapter II of this thesis discusses existing MEMS metrology techniques and their limitations. The third chapter describes the optical interferometry in general and the usage of a diffraction grating and microlens. The fourth chapter discusses the control theory used to maintain high measurement sensitivity during operation. Chapter V details the hardware and software as well as data collection and analysis techniques. The sixth chapter in this thesis relates a case study of a MEMS device and the results generated from using the experimental system. Finally, the last chapter discusses the conclusions and suggestions for future work on this system and in this field in general.

## **CHAPTER II**

### **BACKGROUND AND LITERATURE REVIEW**

The majority of MEMS devices are fabricated using photolithographic techniques developed from silicon micromachining fabrication for electronic semiconductor components, and, therefore, much of the existing metrology techniques are tailored to this domain. In particular, photolithography research has long focused on line width resolution and mask alignment techniques, also known as critical dimensions (Larrabee, 1994). These dimensions are the driving parameters for decreasing the feature size of semiconductor components such as transistors or diodes. The miniaturization of these features leads to more powerful processors. Many of these metrology tools are based on optical microscopy. However, an optical microscope only yields two-dimensional information and gives no feedback on the out-of-plane dimension of a MEMS device. Furthermore, many optical microscopes are diffraction limited to a resolution of  $0.25\mu\text{m}$ .

#### **Contact Metrology Techniques**

The ability to generate data in the out-of-plane dimension began with surface roughness profilometry measurements for bulk deformation processes such as milling or grinding. In this technique, a small metallic stylus with a diamond tip is placed in contact with the measured surface. The diamond tip travels linearly along the length of the specimen, following the contours of the surface. These contours are measured through the deflection of the stylus. The creation of styli with very low inertia and tips with very sharp corner radii led to the development of atomic force microscopy (AFM) (Binnig 1986). The AFM measures the atomic repulsion force between the atoms of the stylus tip

and the atoms of the sample surface, as shown in Figure 1. The difference between the AFM and the stylus profilometer is one of scale and resolution, the latter being much finer for AFMs compared to stylus profilometers. Many AFMs use an interferometer to measure the deflection of the AFM stylus cantilever. This allows the AFM to have a resolution greater than the spacing between atoms within solid, which is on the order of a few angstroms ( $10^{-10}$  m) (Myers 1988). AFMs use the same one-dimensional motion of the tip over the surface as stylus profilometry, and many linear scans must be stitched together to produce a three-dimensional image. The radius of curvature of the probe tip limits the lateral resolution of an AFM, which is around 10nm. The most significant limitations of the AFM for MEMS metrology are the inability to generate dynamic data of out-of-plane motion and the amount of time taken to generate a fully three-dimensional measurement.



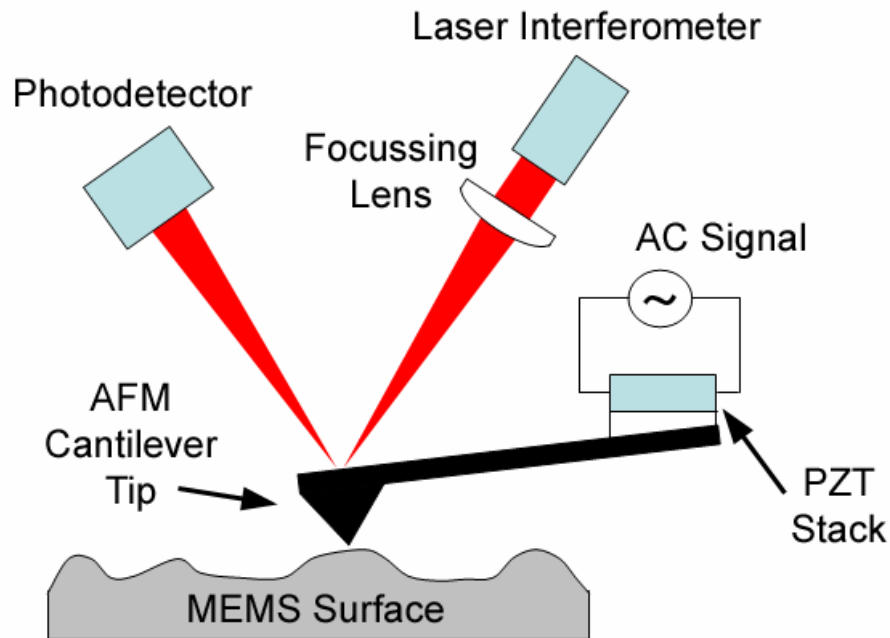


Figure 1. Schematic of an Atomic Force Microscope (AFM)

There are three modes of AFM operation. The first mode is described above. The tip comes in contact with the surface and passively reacts to the forces between the tip and surface as they move relative to one another. Another mode is the tapping mode. In this mode, the cantilever is oscillated in an up and down motion via a piezoelectric transducer (PZT) as it moves over the surface. Generally, the tapping mode produces a higher resolution measurement than passive scanning. The final mode is a non-contact mode where the Van der Waals forces between the probe tip and the surface prevent the probe from contacting the atoms of the surface. This mode produces the lowest resolution scan but prevents surface damage from the probe tip.

Another form of contact MEMS metrology that has its roots in the macroscale is the nano coordinate measuring machine (nano-CMM). A nano-CMM has the same components of a macroscale CMM, containing a small stylus with a tip of specialized

geometry, such as a sphere or a cylinder. The stylus is attached to a motorized head that is able to move and track position in more than three dimensions. As the CMM tip comes in contact with the surface under measurement, the probe tip deflects, and sensors pick up this motion. The location of this point of contact is recorded. This process repeats for many surface contact points, which creates a three-dimensional point cloud. The procedure is performed manually, where a human user moves the probe from point to point, or CAD data is used to generate the initial guess for the location of the next measured point. The nano-CMM has shown resolution comparable to an AFM, and development is currently ongoing for MEMS metrology applications (Pegg 1999).

### **Non-Contact Metrology Techniques**

Aside from these contact methods involving styli, a number of non-contact methods have been developed for MEMS metrology. First and foremost, a standard optical microscope measures lateral dimensions but provides no measurements in the out-of-plane dimension. Using a Nomarsky filter on an optical microscope allows for out of plane motion detection; however, it is impossible to quantify this motion. Confocal laser microscopy, however, can provide some metrology data in this dimension. A confocal laser scanning microscope, diagrammed in Figure 2, works by focusing a laser beam on the surface to be measured and detecting the intensity of the reflected beam. The reflected beam power is a strong function of surface height due to the use of two pinholes, which limit light reflected from points outside of the focal plane. By performing a raster scan of the surface in the horizontal plane and stepping the part in the out-of-plane vertical direction, a three-dimensional point cloud or the surface boundary can be generated. This process utilizes a significant number of image processing

techniques and interpolation to generate an image or a set of data points. Also, lighting conditions and the repeatability of the horizontal and vertical actuators play a huge role in the ability to generate reliable three-dimensional data.

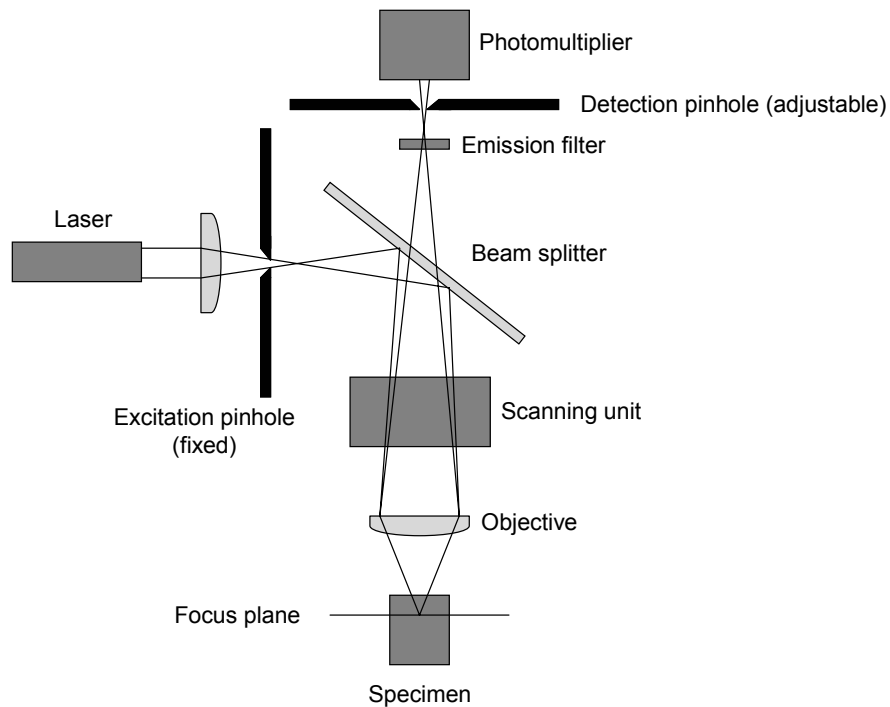


Figure 2. Schematic of a confocal laser microscope (Nichols, 2004)

Another useful tool for the metrology of microscale components is the scanning electron microscope (SEM). An SEM images a sample in the following manner: a highly focused and collimated beam of electrons are incident upon the surface, which in turn knock surface electrons free. Detectors located inside the target chamber, which is typically under a hard vacuum, count these scattered electrons. In addition, since the SEM utilizes electron scattering, the sample must be electrically conducting. For non-conducting samples, a coating must be used to complete the circuit. Recently, there has

been research into SEMs that operate at higher pressures, as well as SEMs that can measure non-conductive surfaces. The advantage of this technique is that the SEM has a very high resolution, on the order of a few angstroms. However, it cannot generate a true three-dimensional image; instead, providing a high contrast two-dimensional image. The resolution of an SEM approaches atomic scale. Scanning electron microscopy is useful for a qualitative analysis of a part, or a quantitative two-dimensional measurement, such as lithography line widths. Generally, SEMs are not suitable for most MEMS metrology applications.

Interferometry has its roots in the famous double slit experiments conducted by Thomas Young in the early 1800s, which proved that electromagnetic radiation could be described as both a particle and a wave, a fundamental idea in quantum mechanics. Albert Michelson and Edward Morely developed the first interferometer and used it to make a very reliable estimate of the speed of light and to disprove the notion that “ether”, an ever-present substance penetrating all space, was the medium in which electromagnetic radiation traveled (Michelson, 1895). This experiment opened up an entirely new paradigm in metrology, where light could be used an absolute standard of measurement. A linear interferometer works by combining two beams of electromagnetic radiation from the same source and noting the phase difference between the two. Linear interferometers are a widely used tool in the area of macro-scale metrology. They are often used for machine tool calibration and error mapping. In the case of micro-scale engineering, this technique has not been widely used.

White light interferometry differs from single wavelength interferometry through the usage of a broadband light source, such as that from a halogen bulb. A diagram of a

white light interferometer is shown in Figure 3. Like a single wavelength interferometer, the white light interferometer utilizes the principle of interference from a single source to determine the out-of-plane height of the sample. An interferogram is produced when light reflected from the surface interferes with a reference beam. An interferogram contains interference fringes that can be used to determine the relative height of the features on the sample surface. However, as the light source is broadband, these interference fringes contain a wide spectrum of light, and filters are used to hone in on a single wavelength at a time. The interference fringes for each particular wavelength are reconstructed using image processing techniques. This gives a white light interferometer the ability to measure out-of-plane displacements of greater than half a wavelength, while achieving sub-nanometer resolution, something that is not possible using a single wavelength interferometer. Edge detection algorithms, image capture hardware, and optics limit the resolution of white light interferometry. Nonetheless, it is possible to achieve micron horizontal precision, while preserving the ability scan a working area of greater than  $1\text{mm}^2$ .

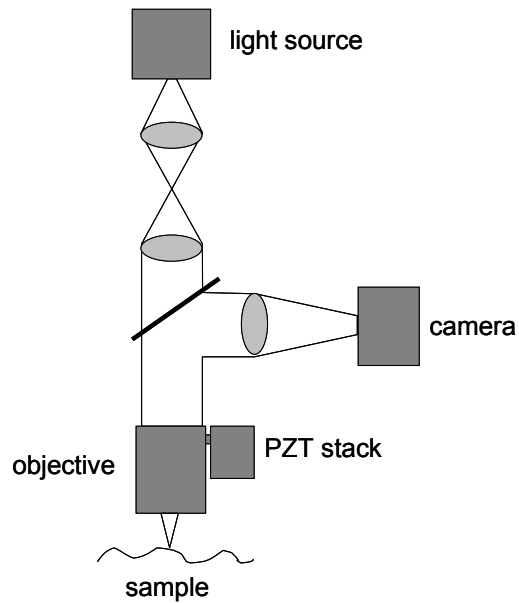


Figure 3. Schematic of a white light interferometer (Shilling, 2003)

An intriguing non-contact metrological tool has recently been developed using the laser, lens, and voice coil of a commercial DVD player. The DVD Probe utilizes the auto-focusing process found in DVD and CD players. A schematic of the hardware used in this system is shown in Figure 4. The light from the diode laser passes through a lens, a beamsplitter, a quarter wave plate, and finally through a reducing objective lens. The resulting shape of the reflected spot from the measured surface is dependent upon the distance from the focus. Four photodetectors in a diamond pattern array detect the shape of this spot. A voice coil attached to the objective lens adjusts the distance from the lens to the surface. A controller monitors the light intensity at the photodetectors and actively controls the voice coil such that focus is maintained at all times. By monitoring the voltage across the voice coil, the DVD probe generates surface height maps. The DVD probe is limited by the reflectivity of the sample; only highly reflective materials such as metals can be measured with the probe. Resolution of the DVD probe is approximately

10nm, and when combined with a high resolution multi-axis stage, the system can be used to analyze microscale parts (Kirkland, 2002).

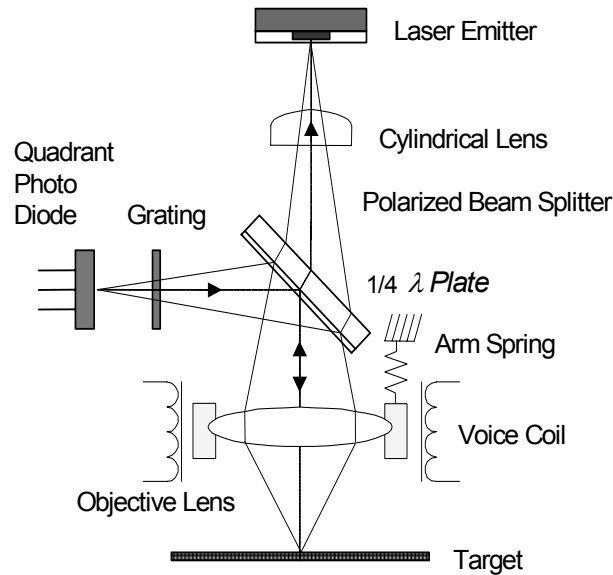


Figure 4. Schematic of DVD Probe (Kirkland, 2002)

### **Destructive Metrology Methods**

Another method that has been used to measure MEMS devices is called Digital Volumetric Imaging (DVI). This process uses a technique called histotechnology, or affixing a specimen in a wax or plastic filler material and viewing the cross sections the part. A microtome removes very thin layers of the specimen one at a time. Hence, the use of this technology is predicated upon destroying the sample under test. A microscope and camera generates two-dimensional images each cross section of the sample embedded in this filler matrix, and edge detection techniques are applied to the images to determine the boundaries of the specimen. Since the spacing between slices is known, a three dimensional point cloud of boundary points is created from the acquired data. The

slice thickness determines the vertical resolution, which can be as small as 0.25 $\mu\text{m}$ . The optics and image capturing equipment limit the resolution in the horizontal plane, which has been shown to be 0.22 $\mu\text{m}$  (Madou, 1997). Table 1 shows a summary of microscale metrology techniques including the resolution and major drawbacks.

Table 1. Summary of static microscale metrology techniques

Metrology Technology	Vertical Resolution (out-of-plane)	Lateral Resolution (in-plane)	Major Drawback
AFM	0.1nm	50nm	slow speed
Micro-CMM	500nm	500nm	under development
Confocal Laser Microscopy	300nm	300nm	dependent upon lighting conditions
SEM	N/A	10 $\text{\AA}$	conductive materials only
White Light Interferometer	0.5nm	500nm	limited angular resolution
DVD Probe	10nm	10nm	dependent upon surface reflectivity

### **Dynamic MEMS Metrology Techniques**

The forces driving the mechanical motion of MEMS devices come from a variety of sources, including capacitive, magnetic, thermal, and combustive. The analysis and quantification of this movement, therefore, becomes a critical component of the quality control and process improvement of these emerging technologies. The length scales for the motion of MEMS devices range from microns to nanometers, with frequencies well into the MHz range. Therefore, a metrology tool that has a large operating range as well as a wide sensor bandwidth would be an extremely useful tool to increase the yield of MEMS devices and drive their market adoption.

One technique, called Stroboscopic Video Microscopy, is used to detect the in-plane motion of MEMS devices. This technology utilizes an optical microscope and a



strobed light source that is synchronized to the actuation signal of the MEMS device (Figure 5). A digital camera records the images, and edge detection techniques are applied to quantify the movement. This is very similar to the stop-action animation employed in some motion picture entertainment. These systems perform with nanometer accuracy (Davis, 1998). Yet, due to the two-dimensional nature of optical microscopy, only in-plane movement is detected. This form of dynamic metrology is unsuitable for MEMS devices that utilize out-of-plane motion.

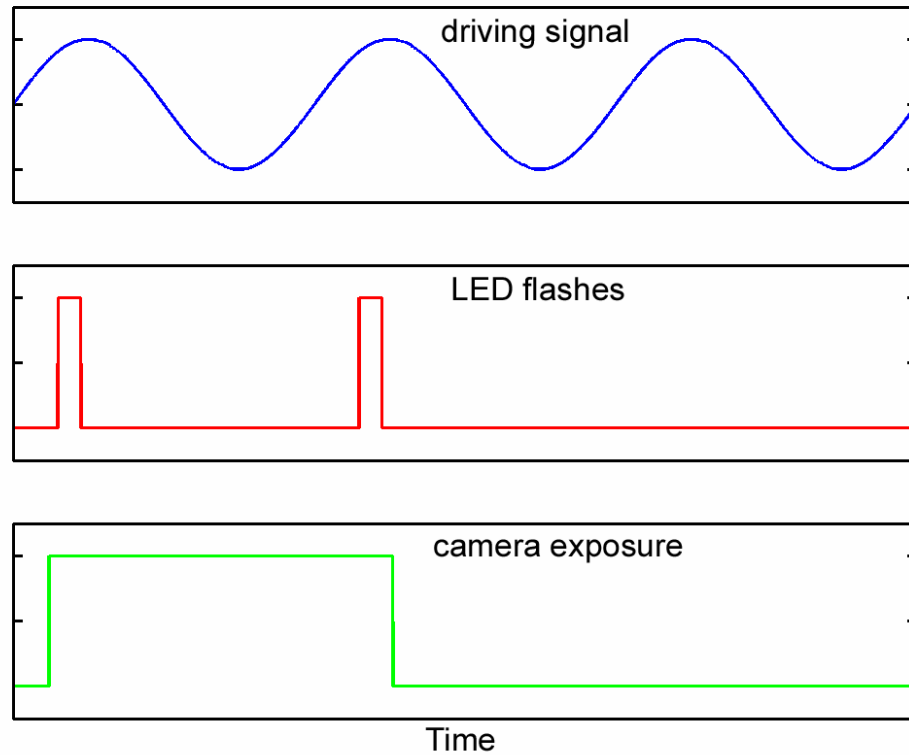


Figure 5. Principle of stroboscopic imagery

However, if an interferometer is used instead of an optical microscope in conjunction with stroboscopic imagery, three-dimensional dynamic data is generated.

Hemmert *et al.* utilized a Michelson interferometer with a strobed LED light source and a charge coupled device (CCD) camera to produce interferograms at various actuation phases. This allows for a full reconstruction of both in-plane and out-of plane motion. The stroboscopic interferometer achieves sub-micron in-plane resolution and sub-nanometer out-of-plane resolution (Hemmert, 1999). Similarly, a laser can be used as a light source for a single point interferometer, as opposed to a wide field light source such as an LED. This sort of system must be combined with mechanical stages to provide true three-dimensional data.

Another technique used to measure the dynamic motion of MEMS devices is called Laser Doppler Vibrometry. Figure 6 shows a schematic of this system. This technique utilizes the Doppler Effect to detect the speed of vibration. When a monochromatic light source is incident upon a vibrating surface, the reflected light undergoes a frequency shift directly proportional to the speed of the vibration. Therefore, the reflected laser light will be frequency modulated through time as the vibrating surface moves towards and away from the laser source. By utilizing a heterodyne interferometry technique, which utilizes two wavelength slightly shifted from one another, the magnitude and direction of the modulated frequency can be detected (Rembre, 2001). Polytec Corporation has developed a micro laser doppler vibrometer, which has an out-of-plane resolution of approximately 0.01nm and an in-plane resolution of 0.5 $\mu$ m (Polytec, 2001).

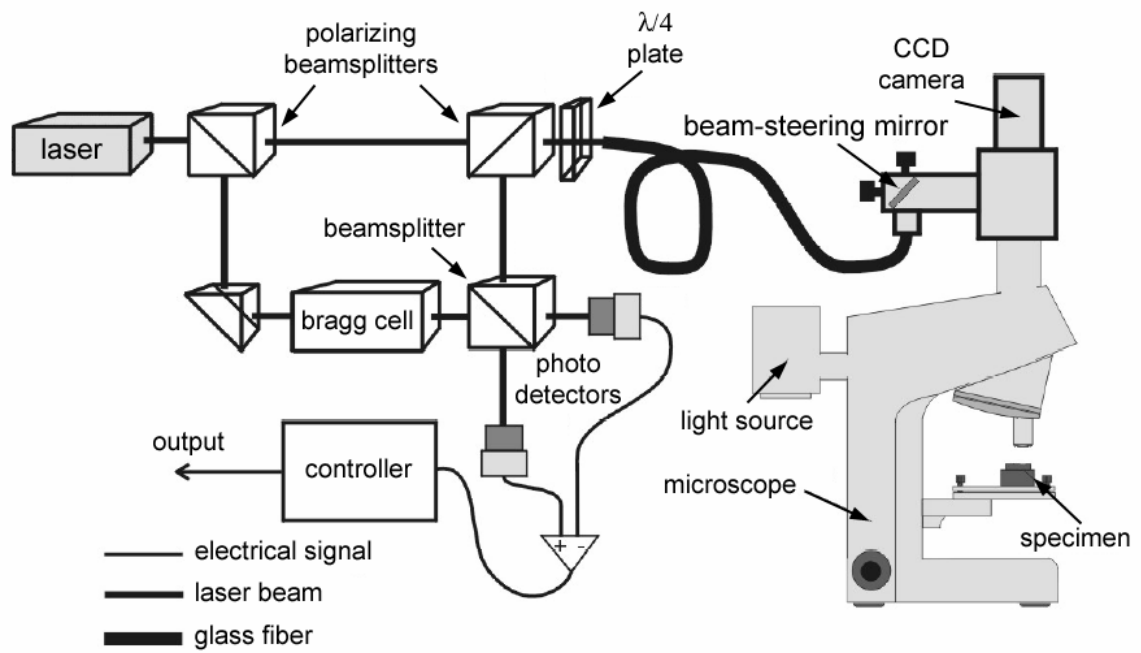


Figure 6. Laser doppler vibrometer schematic (Rembre, 2001)

## **CHAPTER III**

### **OPERATIONAL THEORY**

The goal of the project described in this thesis is the development and testing of a miniaturized interferometer with active mechanical control. The history and working principles of interferometers are discussed in this chapter, including the anticipated resolution and configuration of the particular interferometer used for this project. In addition, the theory of maintaining a high sensitivity measurement is discussed.

#### **Optical Interferometry**

Optical interferometry is a widely used tool in metrology, and has been utilized to measure distances smaller than a nanometer, and longer than a light year. For example, on the macroscale, interferometers measure the errors of the axes of computer numerically controlled (CNC) machine tools, including straightness, angularity, and linear calibration. This allows for the creation of error maps of the entire working volume. Using this technique, high precision manufacturing can be achieved such as the 20 angstrom (rms) surface finish of parts created on Lawrence Livermore National Laboratory's diamond turning lathe. Also, a very large interferometer is under construction at Hawaii's Mt. Keck Observatory. This interferometer uses two identical infrared telescopes. Interferometry is employed to expand the angular measurement capacity of the two 10m telescopes to the equivalent of a single 85m telescope, which would be the largest infrared telescope ever created. The ultimate goal of this interferometer system is the ability to image Jupiter-sized planets orbiting nearby planets.

Interferometry is a powerful tool for the measurement of objects at many different size scales.

### **Michelson Interferometer**

The first interferometer, created by Albert Michelson and Edward Morely in 1887, spawned an entirely new realm of metrology (Michelson, 1895). The ability to resolve absolute distances to a precision of one half of the wavelength of light was a breakthrough that would become the foundation for much of today's microscale metrology. While the original Michelson interferometer was not designed to be used as a system for distance measurement, its potential was quickly realized, and in 1906 Michelson measured the length of the standard meter bar, kept in Paris, to a fraction of the wavelength of the Cadmium absorption line. This eventually led to the abandonment of a physical specimen as the standard for length. Instead, the distance standard is now defined by the speed of light in a vacuum.

A schematic of the Michelson interferometer is shown below in Figure 7. A beamsplitter splits a monochromatic light source into two perpendicular beams. In the original Michelson interferometer, the beamsplitter consists of a half silvered mirror placed at a 45 degree angle. These two perpendicular beams are reflected off of two mirrors,  $M_1$  and  $M_2$ , placed normal to the incident beams. The distance traveled by the first beam is  $2d_1$  and the distance traveled by the second beam is  $2d_2$ . The reflected beams recombine again at the beamsplitter, which allows half of the light pass through and reflects the other portion of the light to a detector. The resulting pattern of the two superimposed beams is known as an interferogram.

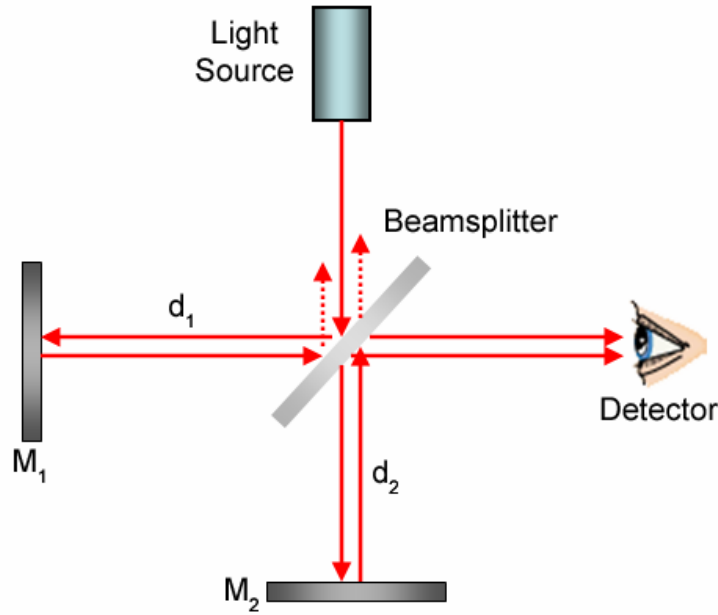


Figure 7. Schematic of a Michelson interferometer

Interference occurs whenever the waves of two coherent sources meet. In the Michelson interferometer, these sources are the two perpendicular beams reflected from the mirrors that are superimposed upon each other at the detector. The interference of the two beams utilizes the theory of superposition to create a distance measurement. If two signals are superimposed upon each other and are perfectly in phase, the interference signal will be purely constructive (Figure 8 (a)). If the two signals are  $180^\circ$  out of phase, the interference is purely destructive, and no intensity will be present at the detector (Figure 8(b)). The phase difference in an interferometer occurs when one beam travels a different distance than the other beam, which is known as the path difference. Every half wavelength of path difference, the combined signal reaches a point of destructive interference, or trough. Similarly, an intensity peak occurs every half wavelength of path

difference. The peaks and troughs are separated by  $\lambda/4$ . The entire sinusoidal curve is called the interference curve and is the basis for all metrology using interferometers.

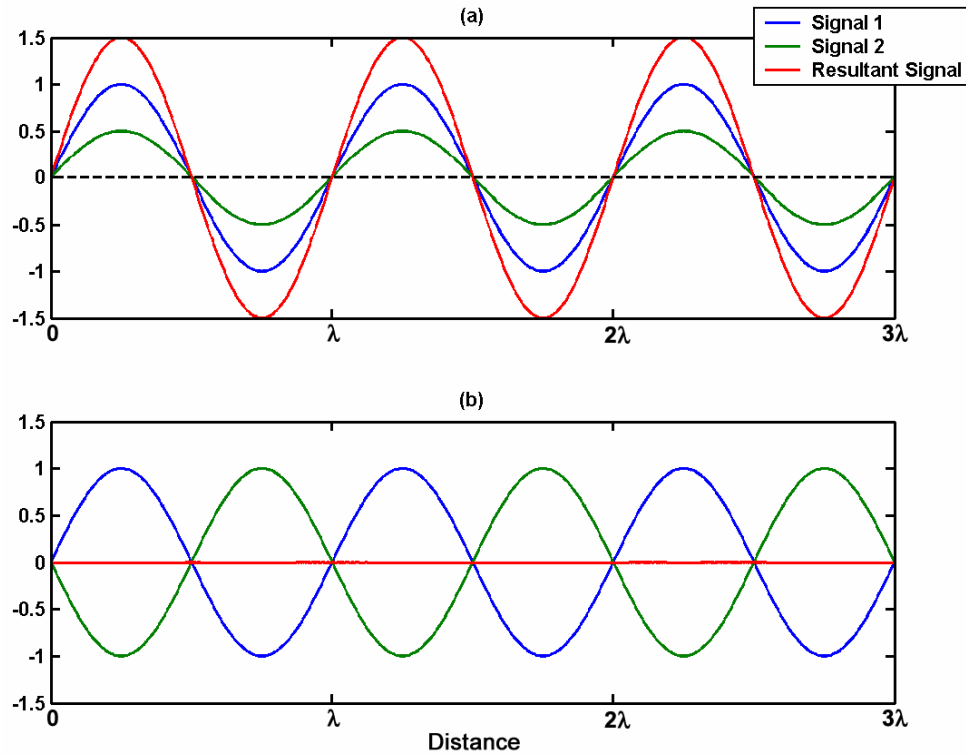


Figure 8. Constructive (a) and destructive (b) interference

There are two methods that the interference phenomenon can be used to generate data about relative distances. In the Michelson interferometer, if  $M_1$  is moved at a constant rate, either forward or backward, the intensity at the detector will move from trough to peak every  $\lambda/4$ . By counting the number of peaks seen by the detector, a measure of the distance traveled can be computed. The resolution of this measure is, therefore, one half of the wavelength of the light source. This type of measurement is used by many commercial interferometer systems. The resolution of these devices is

316nm or half the wavelength of a Helium Neon (HeNe) laser. Other techniques such as heterodyning the frequency of the laser produce higher resolution commercial interferometers. The second method of generating measurements from the interference curve involves dividing up the interference curve between the peak and trough. The intensity curve is a stable sinusoidal function, and as long as the jumps between measurement points do not exceed  $\lambda/4$ , the distance traveled can be computed from the sinusoidal transformation. A sensor using this method has a theoretically infinite resolution. In practice, the precision of the analog to digital converter (ADC) used and signal to noise ratio (S/N ratio) limit the resolution, although sub-nanometer precision has been achieved as detailed in Chapter V of this thesis.

### **Diffraction Grating Interferometer**

In addition to the original Michelson interferometer configuration, there are many other interferometer designs, including the Frizzau interferometer; the Mach-Zehnder interferometer; the Sagnac, or ring, interferometer; and the diffraction grating interferometer, which is used in the system described in this thesis. As with all interferometers, the diffraction grating interferometer, utilizes the superposition of two waves of light coming from the same coherent source. A single beam illuminates an optical grating consisting of thin, reflecting stripes on an optically clear substrate. If absorption is ignored, a portion of the beam passes through the grating while the rest of the light is reflected. This causes the recombined light to diffract at an angle from the grating surface, as shown in Figure 9.



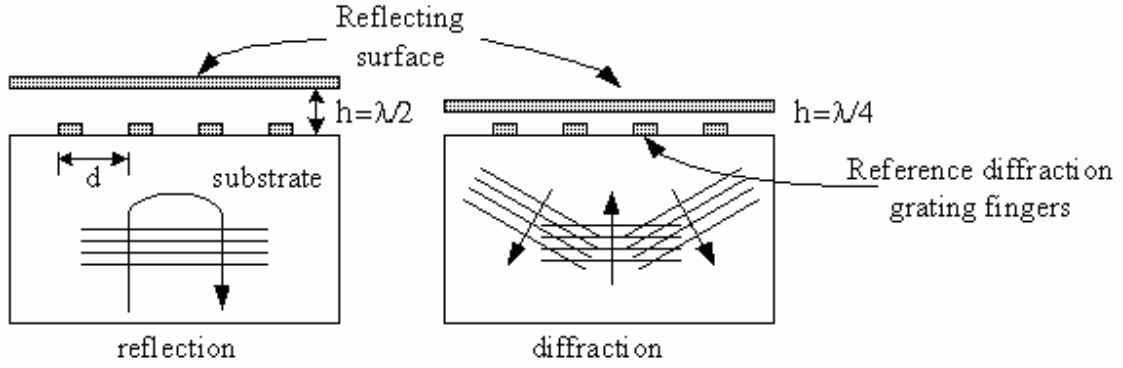


Figure 9. Diagram of light refracted from a grating and a reflecting surface (Kim, 2003)

The angle of these diffraction orders is given by Equation (1) where  $d$  is the stripe spacing,  $m$  is any integer (including 0), and  $\lambda$  is the wavelength of the light source. The integer number indicates the order number of the diffraction spot, e.g.  $m=0$ , is the zeroth order spot,  $m=\pm 1$  are the first order spots, etc.

$$d \sin \theta = m\lambda \quad (1)$$

A surface some distance away from the grating reflects the light that passes through the grating. Similar to a Michelson interferometer, the intensity of the light at each diffraction order is a periodic function of the distance between the grating and the reflective surface, also called the stand-off distance. In Figure 10, three example stand-off distances and their respective intensities are plotted for an observation plane 1mm away from the diffraction grating. The grating period in this example is  $2\mu\text{m}$  and 10 grating fingers are modeled. A HeNe laser with a wavelength of 632.8nm is the simulated light source. When the stand-off distance is an even integer number of quarter wavelengths, the incident light is reflected back to the zeroth order. Similarly, when the

distance is an odd integer multiple of  $\lambda/4$ , it is reflected back to the first orders. Any other distance will give a mixture of these two reflective scenarios, as shown when the stand-off distance is  $\lambda/8$ . These results indicate where to place the photodetector in an experimental system. In most cases it is nearly impossible to place the detector at the location of the zeroth order as it is reflected directly back toward the source. However, the first order is accessible with proper geometrical configuration.

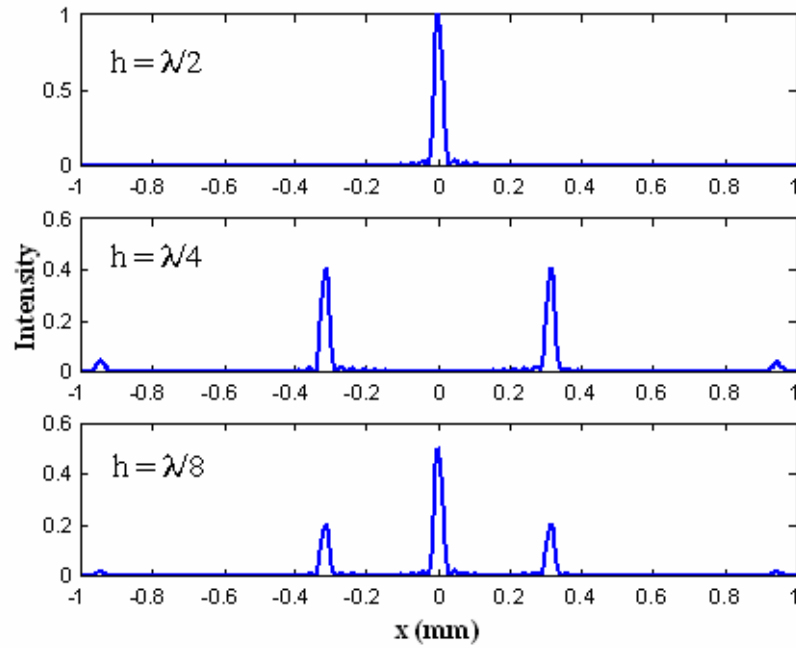


Figure 10. Location of the diffraction orders as from an example grating (Kim, 2003)

Furthermore, by applying Fourier analysis of the diffraction grating geometry, the far-field intensity of the diffraction orders can be modeled by Equations (2) and (3). The intensities are a periodic function of the stand-off distance, and, therefore, are identical to the interference curves presented in Figure 11.

$$I_0 \propto A \cos^2 \left( \frac{2\pi}{\lambda} h \right) \quad (2)$$

$$I_1 \propto B \sin^2 \left( \frac{2\pi}{\lambda} h \right) \quad (3)$$

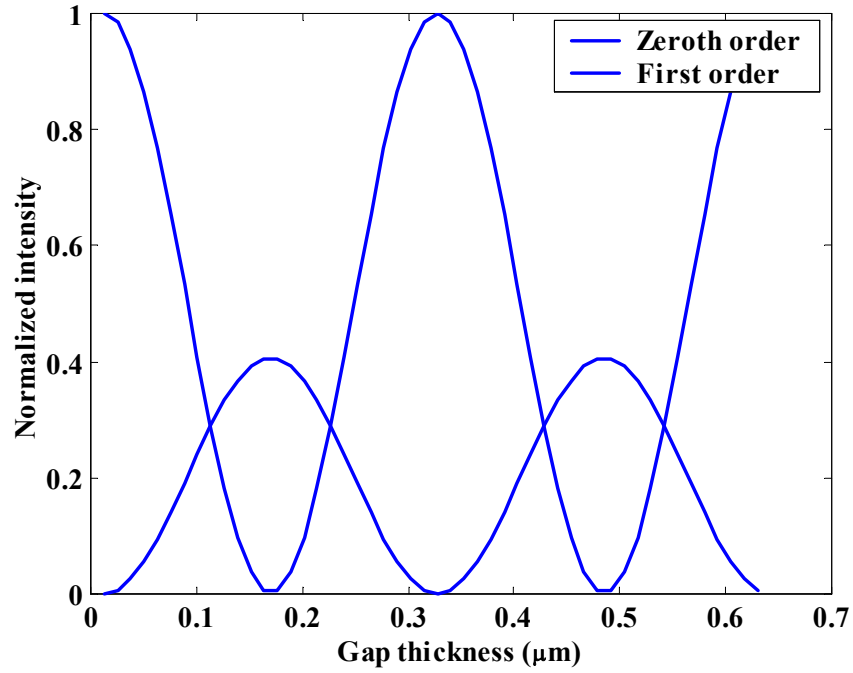


Figure 11. Interference curves for the first and second diffraction orders (Kim, 2004)

It is possible to fabricate gratings with this periodicity using photolithographic techniques (Kim, 2002). The limitation to this technique for interferometric measurements is the lack of absolute displacement measurements, i.e. step changes of greater than  $\lambda/4$  yield ambiguous results. Also, the surface under test must reflect light

normal to the incident beam; otherwise, interference with the reference beam will not occur, and the diffracted light will not be a function of the path difference. This presents a problem for surfaces where the roughness exceeds  $\lambda/4$ , as the reflected light will scatter, hence not causing any interference. The theoretical maximum angle,  $\theta$ , that the surface can be inclined is a function of the final converging lens as shown in Equation (4), where  $r$  is the lens radius of curvature, and  $f$  is the focal length.

$$\theta = 2 \cdot \tan^{-1} \left( \frac{r}{f} \right) \quad (4)$$

## CHAPTER IV

### CONTROL TECHNIQUE

The use of this interferometer system to measure both the static height of a specimen as well as its dynamic motion is a function of the optics used, the bandwidth and resolution of the sensor, and the signal to noise ratio of experimental system. A large contribution to the baseline noise present in the system is the presence of mechanical and acoustic vibrations, which affect the path difference from the sample to the sensor. For example, if mechanical vibrations have an RMS displacement of 20nm, the resolution of the entire system cannot exceed this value. In addition, these random movements along the interference curve may move the path difference to a non-linear location, or “hump,” such as the portion located around  $\lambda/8$  in Figure 12. Accordingly, the measurements taken at this location will be highly non-linear. If the change in path difference between measurement points is significant enough, it may wrap around the top of this hump, producing erroneous results. Therefore, a method of reducing the magnitude of these vibrations and controlling the location along the interference curve where the measurements are taken will improve the resolution and performance of the interferometer system.

The most sensitive region of the interference curve, in terms of optical intensity per unit of displacement, is the portion where the slope (first derivative) is greatest, or where the curvature (second derivative) is the smallest, as indicated in Figure 12, where the path difference is  $\lambda/4$ . This portion is the most linear region of the curve and is repeated every quarter-wavelength of path difference. Therefore, a method of locking onto this region will produce the best performance of the interferometer.

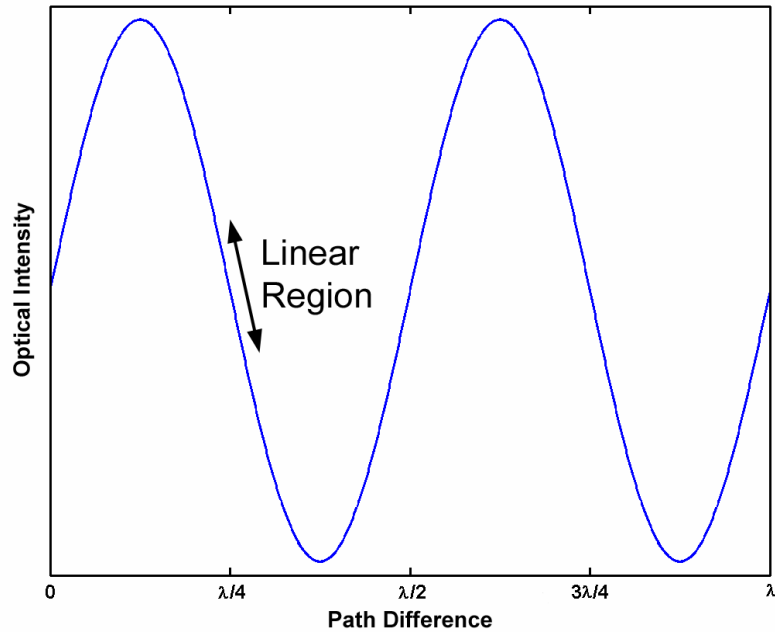


Figure 12. Interference curve showing linear region

The most obvious way to lock onto the linear region of the interference curve is to monitor the intensity of the optical power during operation. By establishing a set-point for this signal in the center of the linear zone shown in Figure 12, a feedback mechanism is created where the position is driven back to the linear region. Ideally, this optical power signal is only a function of the path difference between the grating and the sample, and the lowest optical power is zero. However, this is not the case in real systems, as some dependence upon ambient lighting conditions and the reflectivity and slope of the surface being measured always exists for the interference curve. The reflectivity and the slope of the surface will differ for portions of the specimen surface. Thus, the simple magnitude of the optical power cannot be used if the metrology system is to function as a scanning sensor, or one that performs measurements of many points over the surface of a specimen. Therefore, another method of determining if the interferometer lies within the

linear region must be utilized that is not dependent upon the surface reflectivity or the slope of the surface.

A different approach to isolating linear region utilizes the derivatives of the optical intensity present in the interference curve. From Equation (3), the intensity present at the first interference order is a sinusoidal function of the path difference. Using simple calculus, the center point of the linear region is an inflection point, and therefore, the curvature, or second spatial derivative, is zero at this point. This is true regardless of the surface reflectivity and slope, which changes both the mean and the amplitude of the interference curve. Therefore, the second spatial derivative is used as the basis for controlling the path difference such that the interferometer always operates within the region of highest sensitivity.

Modulating the path difference between the specimen and the sensor generates a time varying intensity signal at the first diffraction order, as shown in Figure 13. Assuming the modulation function is sinusoidal, this modulated intensity signal,  $I_{mod}$ , is represented in Equation (5) where  $A$ ,  $B$ , and  $C$  are constants,  $\lambda$  is the wavelength of the light,  $x$  is the path difference,  $\omega$  is the modulation frequency, and  $t$  is time. The greater the reflectivity of the specimen surface, the greater the difference between the maximum intensity and minimum intensity of the interference curve. Assuming the modulation amplitude,  $B$ , is held constant, the amplitude of the optical intensity,  $A$ , yields a measure of the surface reflectivity. Monitoring this value during a scan of the surface allows the sensor to compensate for changing surface reflectivity.

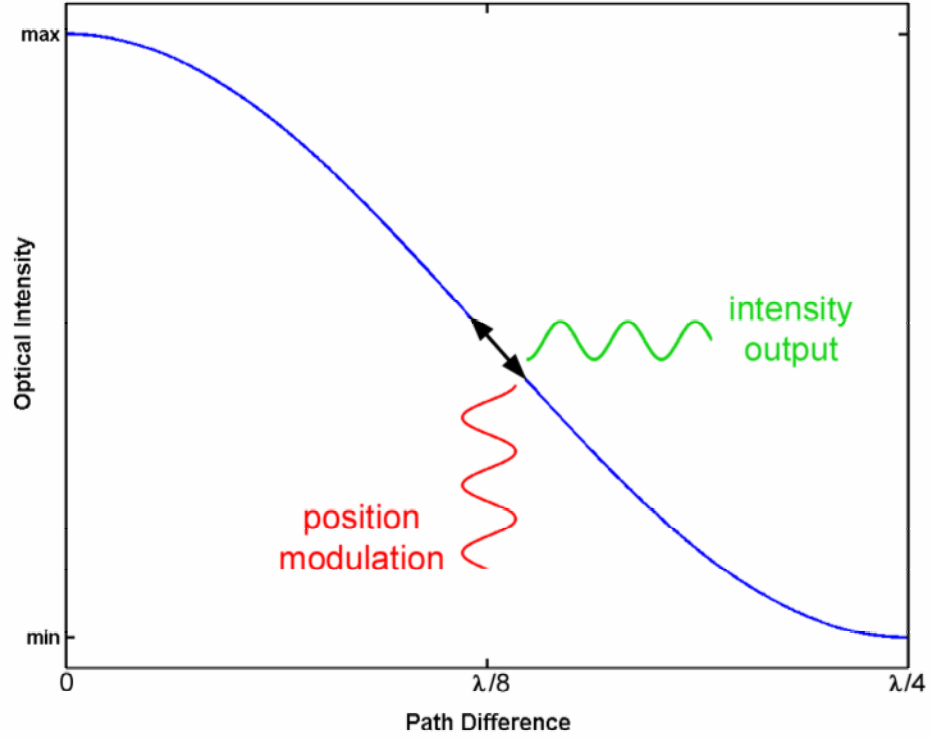


Figure 13. Interference curve showing the position modulation and optical intensity output

A method for locking onto the linear region of the intensity curve also follows from the analysis of the modulated intensity signal. Since  $I_{mod}$  takes the form of a squared sinusoid, it will contain the frequency  $\omega$ , and all harmonics of  $\omega$ . Performing a Fourier transform on Equation (5) yields the following result: the power present in the signal at the frequency  $\omega$ , also known as the fundamental frequency, is proportional to the first spatial derivative of the interference curve. Similarly, the power present in the frequency  $2\omega$ , or second harmonic, is proportional to the second spatial derivative of the interference curve. These relationships are expressed in Equations (6) and (7), and a mathematical proof is given in Appendix A. Therefore, minimizing the magnitude of the second harmonic, in turn minimizing the second spatial derivative, forces the



interferometer to operate in the most sensitive linear region of the interference curve. This relationship is the basis for the control scheme developed later in this chapter.

$$I_{mod}(x, t) = A \cos^2 \left( \frac{2\pi}{\lambda} (x + B \sin \omega t) \right) + C \quad (5)$$

$$I_{mod}(\omega) \propto \left| \frac{\partial I_1}{\partial x} \right| \quad (6)$$

$$I_{mod}(2\omega) \propto \left| \frac{\partial^2 I_1}{\partial x^2} \right| \quad (7)$$

The correlation between the spatial derivatives and the harmonics of the frequency modulated signal means that the first harmonic ( $\omega$ ) and second harmonic ( $2\omega$ ) signals are  $90^\circ$  and  $180^\circ$  respectively out of phase of the light intensity as shown in Figure 14. While the linear region of the second harmonic signal is repeated every  $\lambda/4$ , only the regions where the slope is positive can be used for feedback control. In these regions of positive slope, negative feedback is present in the system. Therefore, if the controller has some residual error, such as an overshoot, it will be eliminated through time, as shown in Figure 15(a). In the linear region where the slope is negative, the feedback is positive, and an overshoot will lead the controller to move away from this

region, indicated by the red cross in Figure 15(b). Hence, the controller will lock onto the linear region of the second harmonic curve with positive slope. However, if a large enough disturbance is present, the controller may jump  $\lambda/2$  to the next linear region with positive slope. In theory, this may continue indefinitely; however, the actuator has physical limits and the sensor has limited focal depth.

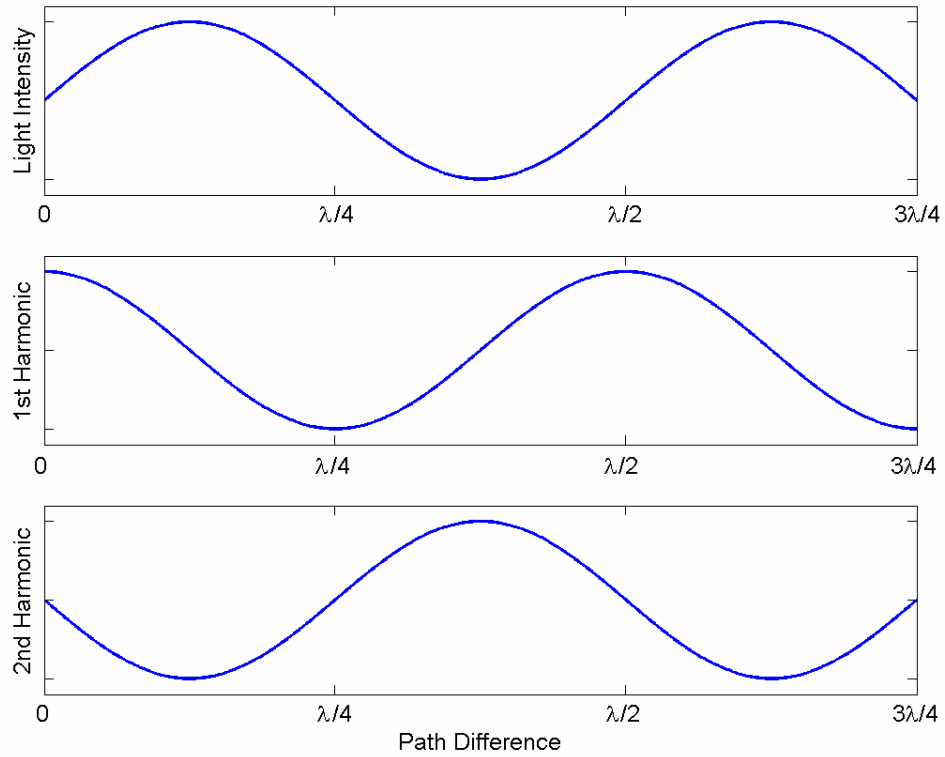


Figure 14. Light Intensity, 1<sup>st</sup> Harmonic, and 2<sup>nd</sup> Harmonic as a function of path difference

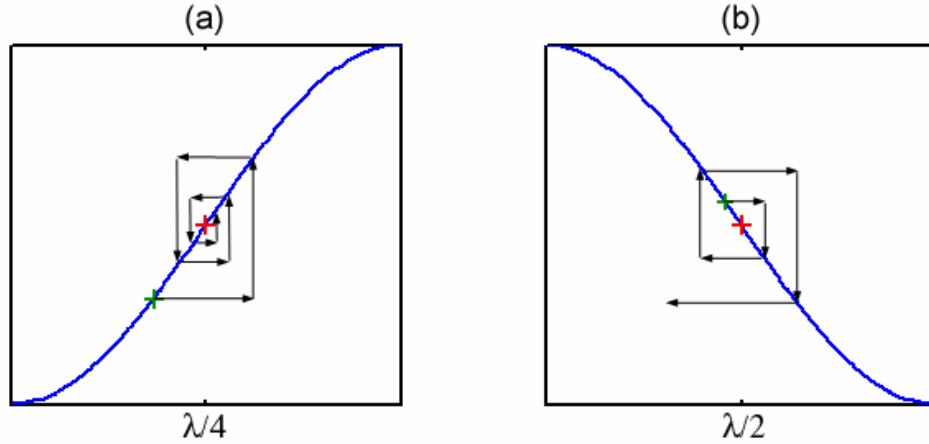


Figure 15. Negative (a) and positive (b) feedback within the linear regions of the 2<sup>nd</sup> harmonic curve

By using the second harmonic information as opposed to the optical power, the issues regarding reflectivity and surface angle are avoided. Also, by insuring that all measurements are taken within the linear region, all measurements will be on the same optical intensity versus displacement scale. Therefore, actively controlling the path difference between the surface and the sensor yields higher resolution, increases the signal to noise ratio, and insures the linearity of all measurements. In addition, the linear region insures that the controller is operating on a single input, single output, linear, time-invariant system.

Graebner *et al.* present a system which utilizes the method described above for isolating the most sensitive region of the interference curve using a piezoelectric transducer (PZT) and a Michelson interferometer in conjunction with a phase sensitive detector (PSD). The PSD locks onto the second harmonic of the photodetector output much like a lock-in amplifier. Data of a thin film resonator has shown that this actively controlled interferometer has a sub-nanometer vertical resolution, with a diffraction

limited horizontal resolution of  $0.5\mu\text{m}$  (Graebner, 2000). The block diagram for this system is presented below (Figure 16).

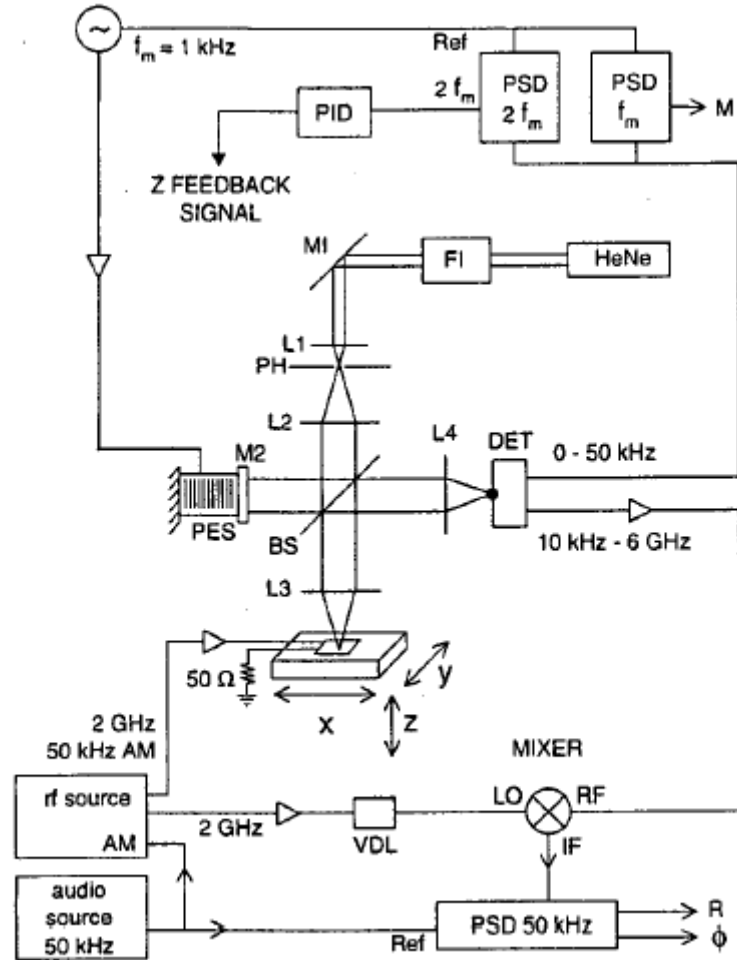


Figure 16. Block diagram of an interferometer with a control system based on the lock-in technique (Graebner, 2000)

### **Analog Phase Locking Through Second Harmonic Monitoring**

To actively control the path difference between the sample and the diffraction grating, the sample is mounted on top of a PZT, as is done in the Graebner experiment.

The PZT modulates the position of the specimen with a 40nm sinusoidal signal at a frequency of 4.3kHz. As stated in Equation (7), the magnitude of the second harmonic of this modulated signal is proportional to the second derivative of the optical intensity. The second harmonic can be measured using a commercial lock-in-amplifier, such as the Stanford Research Systems™ SR830, which was originally proposed for this project. However, this lock-in-amplifier is not suitable for use in a real-time control implementation due to its slow time response, making it unsuitable for active control. Therefore, a discrete analog lock-in solution is proposed and implemented. Figure 17 below diagrams the electronics circuit used for this analog implementation. The full block diagram of the control system is shown in Figure 18.

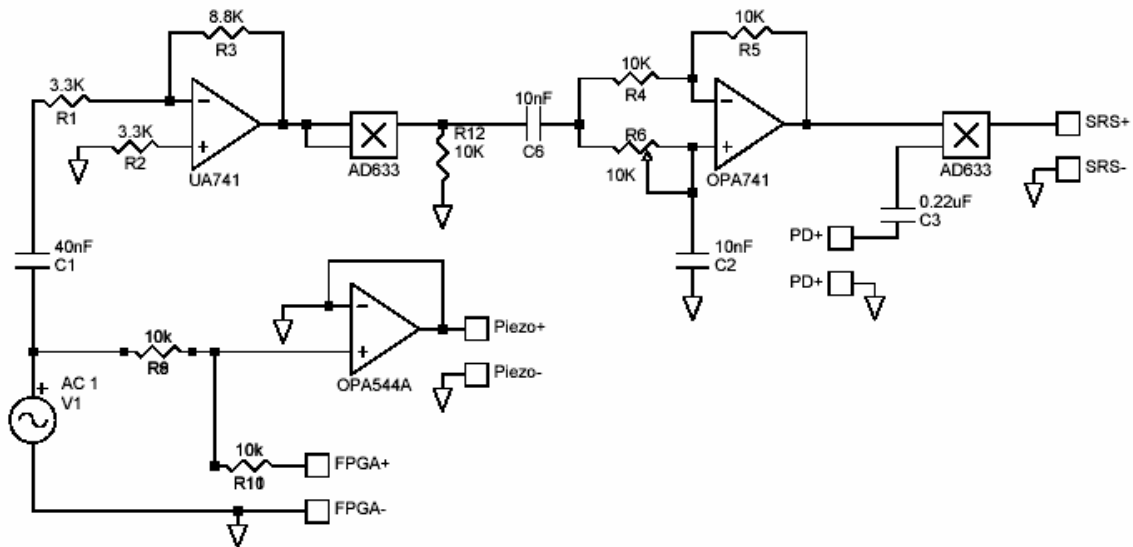


Figure 17. Schematic of the analog circuitry used for the second harmonic locking

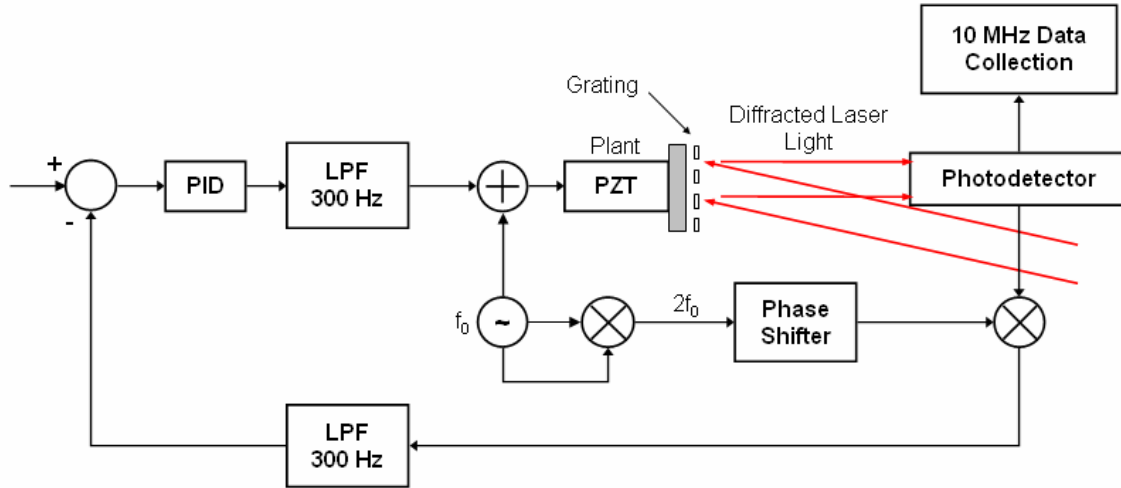


Figure 18. Control system block diagram

A sinusoidal signal is generated at  $\omega$  from an SRS DS345 function generator and passed to a high current summing amplifier and an analog multiplier, which creates a signal at  $2\omega$ . This signal is amplified and passed to an all-pass filter implemented with a standard 741 op-amp, a potentiometer, and an RC circuit network. The all-pass filter adjusts the phase of the  $2\omega$  signal such that the phase difference with the optical intensity signal measured by the photodetector is minimized. These two signals are multiplied together in another discrete analog multiplier, which convolves the  $2\omega$  signal with the optical intensity signal. This convolution moves the power present in the region around the second harmonic frequency to the DC level as seen in the simulated Bode plots of Figure 19. The multiplied signal is then low-pass filtered such that the result contains the magnitude of the second harmonic of the optical intensity signal and the magnitude of any signals that fall under the cut-off frequency of the filter. These low-frequency signals are the result of mechanical and acoustic vibrations that affect the path difference between the measured surface and the diffraction grating.

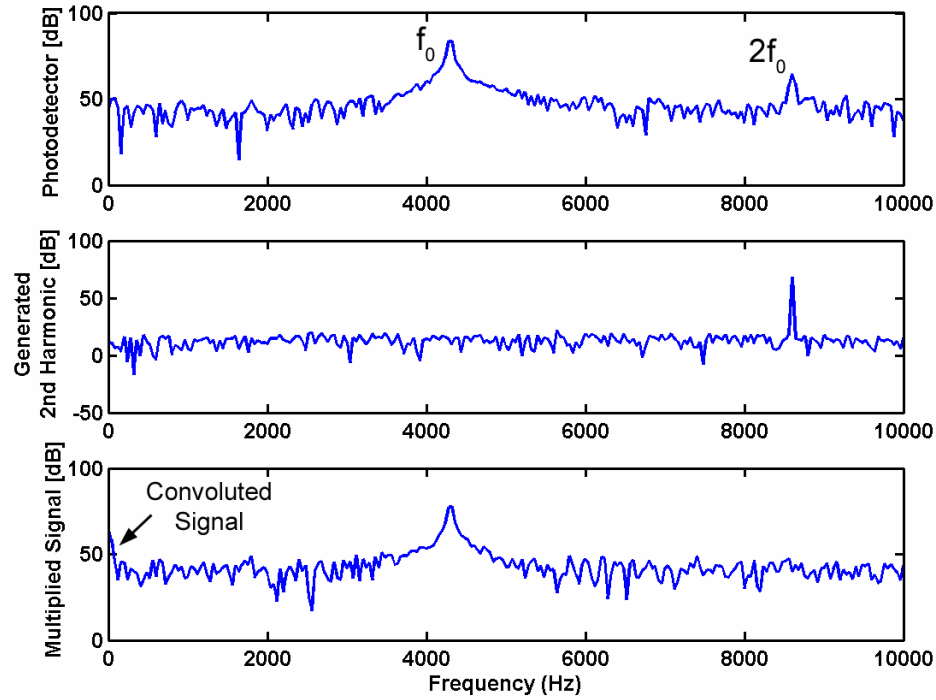


Figure 19. FFTs of simulated photodetector, generated 2<sup>nd</sup> harmonic, and multiplied signals showing convolution

The output from the low-pass filter is used as the process variable for a Proportional Integrative Derivative (PID) controller. To aid in the tuning of this controller, it is implemented digitally on a National Instruments PXI-7115 Field Programmable Gate Array (FPGA) processor. This implementation allows for the flexibility to implement anti-windup techniques, as well as digital filtering of both the input and output. In addition, the speed of the control loop is easily controlled on the FPGA. Much like a Digital Signal Processor (DSP), the FPGA utilizes only fixed point numerical representation, which makes programming the FPGA a bit more difficult than floating point processors. PID control using fixed point representation is shown to be stable, fast, and flexible for the control of linear systems (Murphree, 2002). The FPGA

device is preferable to a DSP in cases where operations can be optimized to run in parallel, such as the implementation of two separate PID control loops running simultaneously. It is theoretically possible to scale an FPGA device such that hundreds of PID control loops are run simultaneously and independently with no loss of speed or bandwidth.

There are other metrology systems that utilize this harmonic locking technique to reduce the impact of noise sources, such as the frequency tuning of an iodine laser (Aloha, 1998). In this case, many harmonics are measured and the frequency tuned to a particular iodine absorption line with the use of a digital PI controller implemented on a fixed point DSP. This allows for a much greater stability of the frequency of the laser and helps to reject thermal drifts or lasing cavity dimensional changes.

### **Tuning and Calibration of the Control System**

The method of control has now been established for the system described in this thesis and the next section describes the tuning and calibration of the control. The control system consists of a single input, single output, linear time-invariant system, which is controlled using a controller programmed on an FPGA device. In order to determine the type of controller to use and the respective gains to be applied, an analytic model of the system is created, and experiments are run to validate this model and discover the discrepancies between the model and the real system. The model and the desired dynamic responses determine the controller design.

### **Analytic Model**

First and foremost for the analysis and tuning of a control system, a basic model of the plant dynamics must be created. In this case, the plant (Figure 18) consists of a



PZT stack and the sample under test affixed to the free end. A picture of this setup is shown in Figure 20. A PZT with this type of loading generally acts like spring-mass-damper system (Figure 21). The spring component is the piezoelectric transducer, the sample under test is the mass, and the damper is the viscosity of the air surrounding the system. This system is a second-order mechanical system; yet, it is somewhat non-linear. The PZT has both non-linear and hysteresis responses; however, under proper actuation conditions, the PZT acts linearly (NEC / Tokin, 2003). Therefore, the nonlinearities are ignored in this analysis. Generally, the transfer function of a second order system is written as shown in Equation (8), where  $\omega_n$  is the undamped natural frequency and  $\zeta$  is the damping ratio.

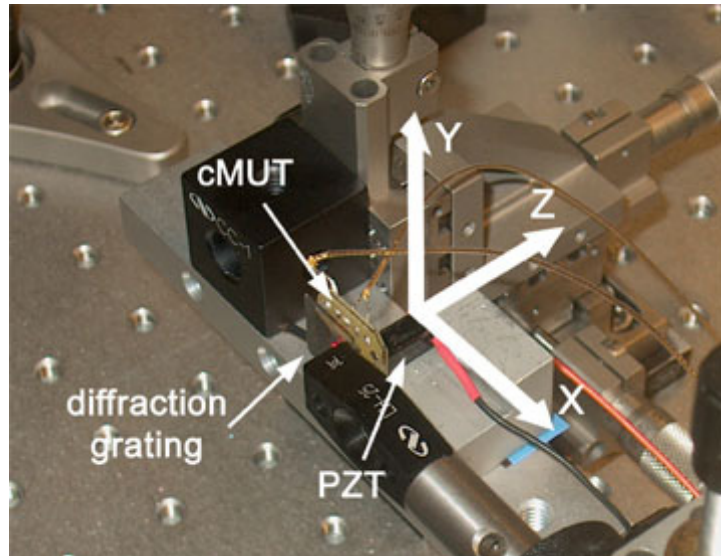


Figure 20. Photograph of the experimental setup with axes labeled

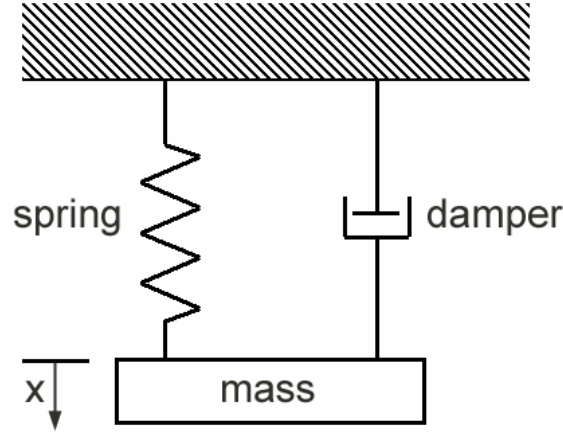


Figure 21. Diagram of a mass, spring, damper mechanical system

$$G(s) = \frac{\omega_n^2}{s^2 + 2\zeta\omega_n s + \omega_n^2} \quad (8)$$

A second order system has a few unique and identifiable characteristics. First, if the system is subjected to a unit step input, and the system is underdamped ( $0 < \zeta < 1$ ), it will exhibit an oscillatory response, which asymptotes to a final value over time. Underdamping is assumed with this system because the mass is very small compared to the spring constant of the PZT. Second, an underdamped system indicates that the closed-loop poles are complex conjugates of each other and lie in the left-hand plane of the  $s$ -plane (Ogata, 1997). The frequency of this oscillation, called the undamped natural frequency,  $\omega_n$ , can be expressed in terms of  $\omega_d$  and  $\zeta$  as shown in Equation (9). Finally, the damped natural frequency,  $\omega_d$ , is the dominant frequency present in a Fourier transform of the output from a step response.

$$\omega_d = \omega_n \sqrt{1 - \zeta^2} \quad (9)$$

### **Experimental Validation of the Analytic Model**

In order to validate the analytic model of the plant system, two different experimental tests are run: a step response analysis and a swept sine-wave analysis. A function generator is used to generate a square-wave at low frequency, creating a recurring step function. A high current op-amp drives the capacitive load of the PZT. The output from the photodetector is recorded at 1MHz. Figure 22 shows the time series of this step response. Clearly, the assumption of an underdamped system holds true, as the end mass oscillates rapidly while slowly being damped out. An FFT of the response (Figure 23) shows that the PZT plant has a number of harmonic frequencies, although the maximum peak occurs near 4500 Hz, which corresponds to the damped natural frequency,  $\omega_d$ .

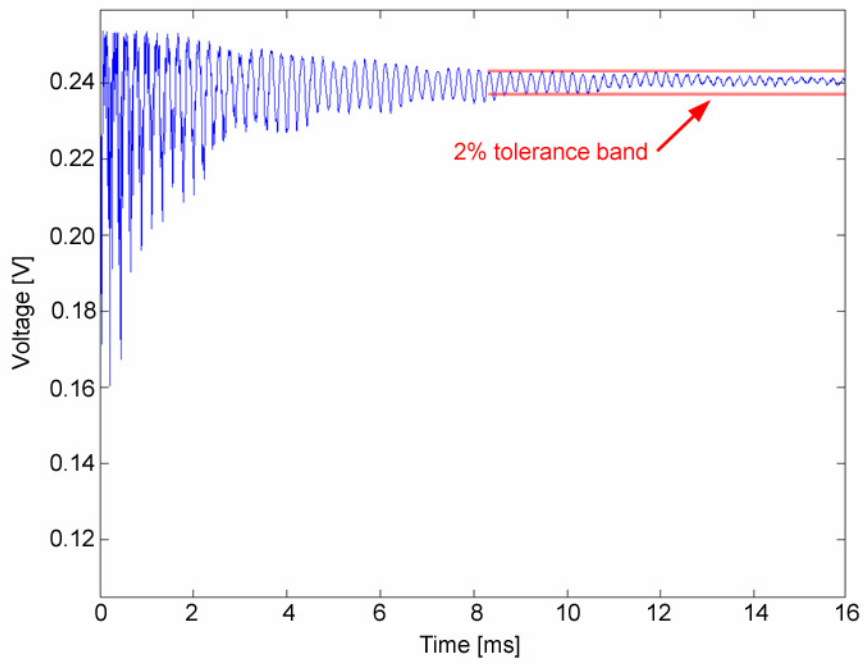


Figure 22. Time series of a measured step response showing 2% tolerance band

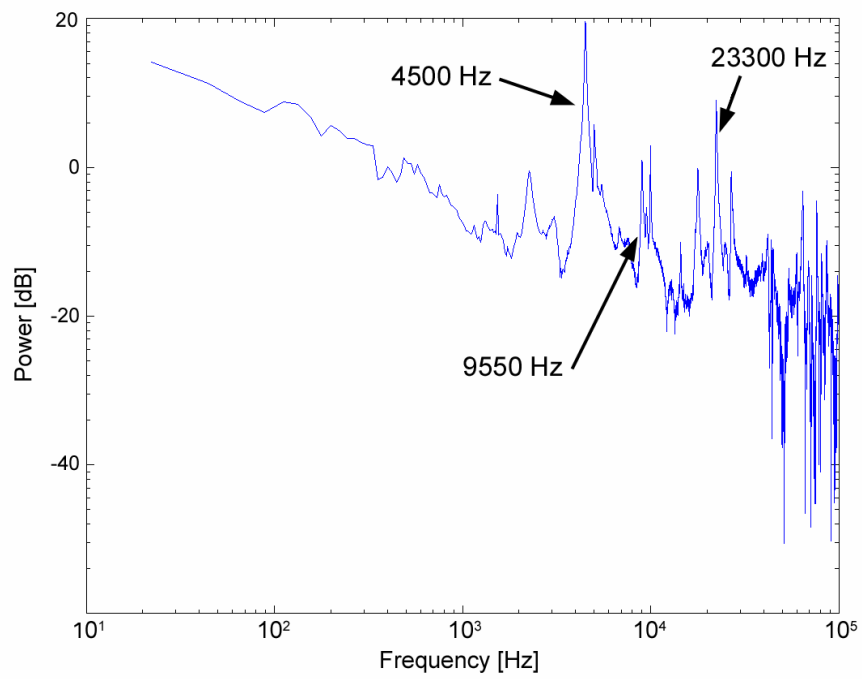


Figure 23. FFT of a step response showing harmonic peaks

The parameters of the second order system, such as the undamped natural frequency, can be derived from data in the step response. The settling time of the step response,  $t_s$ , signifies the time required for the output to settle into a band of  $\pm 2\%$  of the steady state value. The step response shown in Figure 22 has a settling time of approximately 9.3ms. Utilizing Equation (10), the damping ratio,  $\zeta$ , of the plant is estimated to be 0.0155. A damping ratio this small indicates that the system is severely underdamped, which is predicted by the initial physical model for the plant. Using Equation (9), this also means that the undamped natural frequency is essentially equal to the damped natural frequency that appears in the step-response.

$$t_s = \frac{4}{\zeta \omega_d} \quad (2\% \text{ criterion}) \quad (10)$$

In a similar vein to the analysis done on the step-response experiment, a function generator is used to create a swept sine-wave input for the plant. Both the input and output are recorded for the swept wave, and the open-loop gain is calculated for all frequencies. The results, shown in the Bode plot in Figure 24, are very similar to the step-response. The plant shows nearly identical dynamics, with the largest peak coming at 4500Hz, and secondary peaks occurring at 9550Hz and 23330Hz. Note that the gain at frequencies under 2kHz has a nominal gain of around -10dB. This indicates that within this frequency band the input magnitude is approximately three times the output magnitude. This correlates well with the observed nominal amplitudes of the waveforms viewed on an oscilloscope. Typically for a 500 mV signal driving the PZT, the sensor

output will be in the 100mV range. At the harmonic peaks, the sensor gain approaches 0dB, or unity gain.

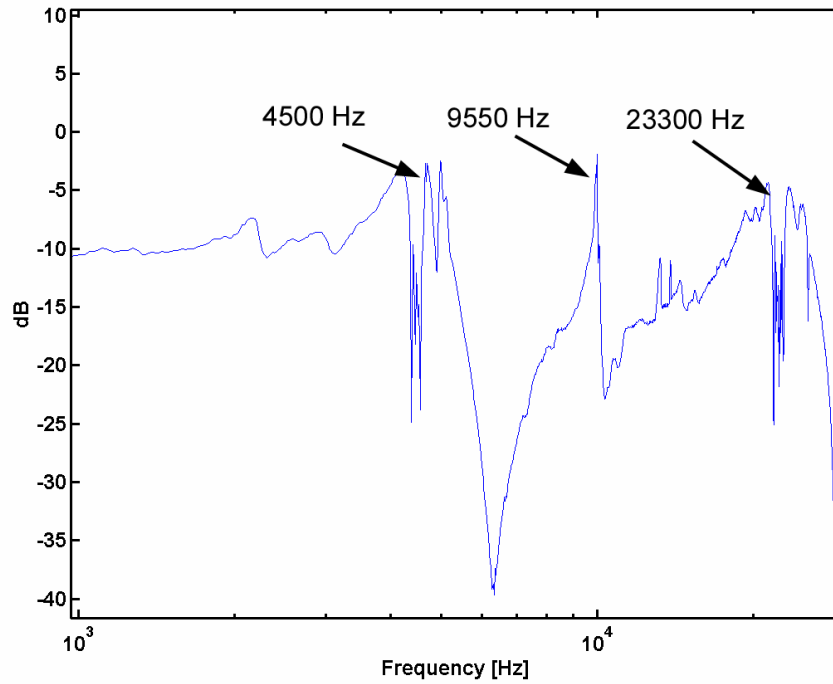


Figure 24. Bode plot of swept sine wave

Therefore, following the theoretical transfer function of a second order system (Equation (8)), the plant system is modeled as a single second order system having a natural frequency of 4500 Hz, as this is the highest magnitude peak as well as the lowest frequency harmonic peak. The unity gain transfer function for this analytic model of the plant is given in Equation (11), and a Bode plot of the open-loop gain is shown in Figure 25.

$$G_p = \frac{7.99e8}{s^2 + 1666s + 7.99e8} \quad (11)$$

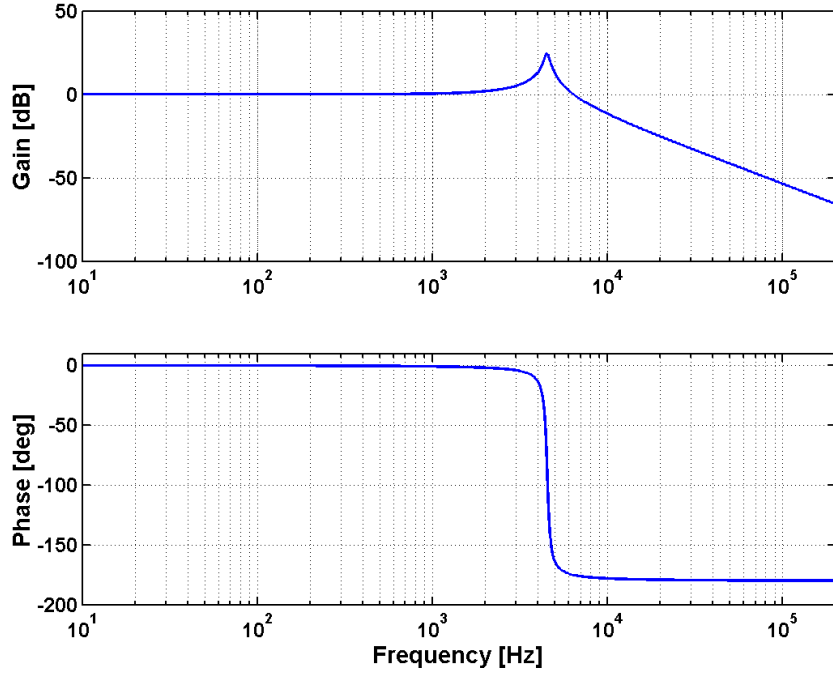


Figure 25. Bode plot of the plant analytic model

In the block diagram for the entire system, there are other elements than the PZT stack and photodiode, which are characterized above. The system dynamics of these elements, such as the analog multipliers, the all-pass filter (or phase shifter), and the low-pass filter, must be accounted for if a closed loop transfer function is to be derived. Swept sine-wave analyses are performed for each of these devices, and the gains are found to be flat across the operational range of frequencies. In addition, no phase lag exists for these components. Therefore, a constant gain represents the transfer functions of each of these elements. Finally, the plant and sensor are lumped into a single transfer

function having the same second order dynamics as the PZT and photodiode, albeit with a scaled gain. The closed-loop block diagram now consists solely of a PID controller, a second order lumped plant and sensor, and a feedback loop connecting the two (Figure 26).

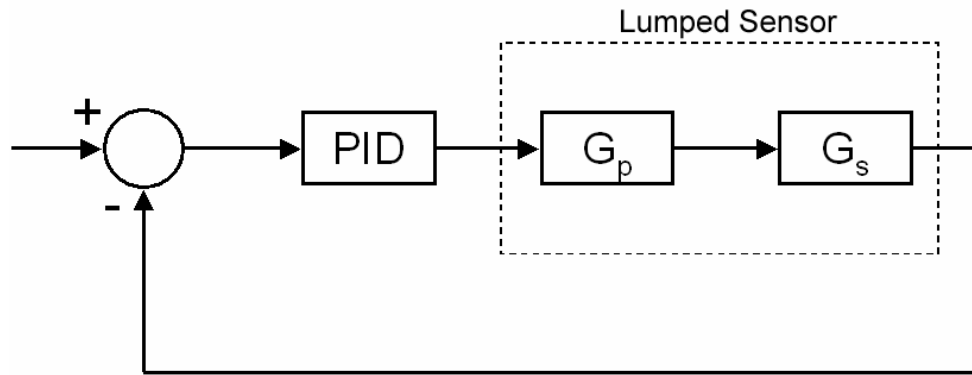


Figure 26. Reduced control block diagram showing lumped sensor

### **Controller Design**

The plant dynamics for this system are known, and a controller is now designed to achieve the system dynamics that are sought. The dynamics that the controlled system should possess are a fast response time, with minimum steady state error. A lag-compensator would be an ideal controller for this type of system, as it eliminates the steady-state error of a second order system, as well as decreasing the rise time, hence improving the responsiveness of the system. The defining parameters of a lag-compensator are the two corner frequencies and the roll-off rate. A Bode plot of this controller is shown in Figure 27. The first corner frequency occurs at  $f_{c1} = 400\text{Hz}$ , which is after the low-pass filter for the real plant, which is set at  $300\text{Hz}$ . The second corner



frequency is located at  $f_{c2} = 4000\text{Hz}$ , which is before the natural frequency of the second-order plant. Finally, the roll-off between these corner frequencies is  $20\text{dB/decade}$ , which yields  $20\text{dB}$  decrease in power between the corner frequencies.

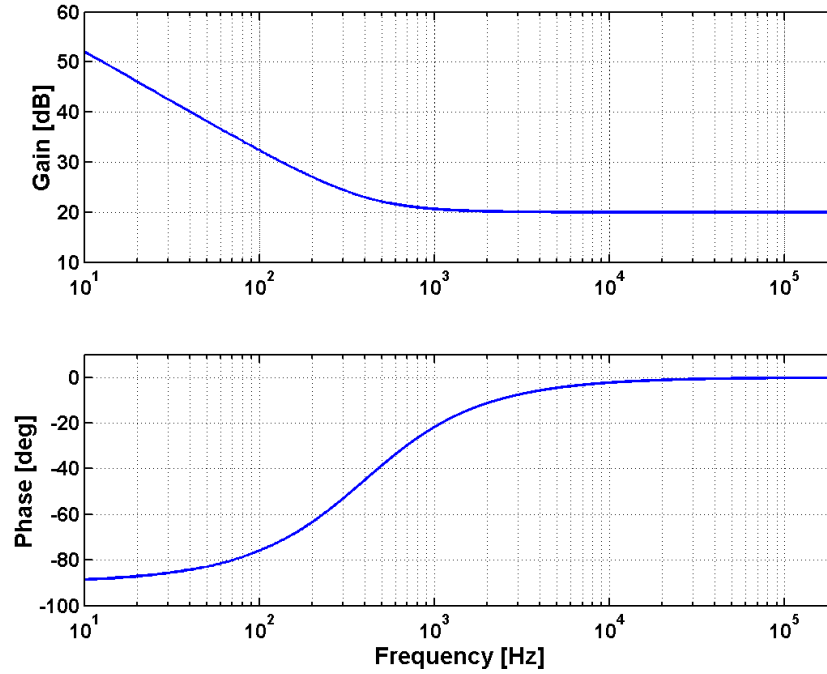


Figure 27. Bode plot of the designed PI controller

The transfer function of this lag-compensator controller is given in Equation (12), where  $T$  is given in Equation (13) and  $\alpha$  is a scaling factor that determines the DC level gain present in the controller. The open-loop transfer function of the system can be calculated by multiplying the open-loop gain of the controller by the open-loop gain of the lumped plant and sensor. This is given in Equation (14), where  $\alpha$  is set to 10. A Bode plot of the entire system is shown in Figure 28.

$$G(s) = \alpha \frac{Ts + 1}{\alpha Ts + 1} \quad (12)$$

$$T = \frac{1}{2\pi f_{c2}} \quad (13)$$

$$G = G_c G_p = \frac{7.99\text{e}9s + 2.009\text{e}13}{s^3 + 1666s^2 + 1.99\text{e}8s} \quad (14)$$

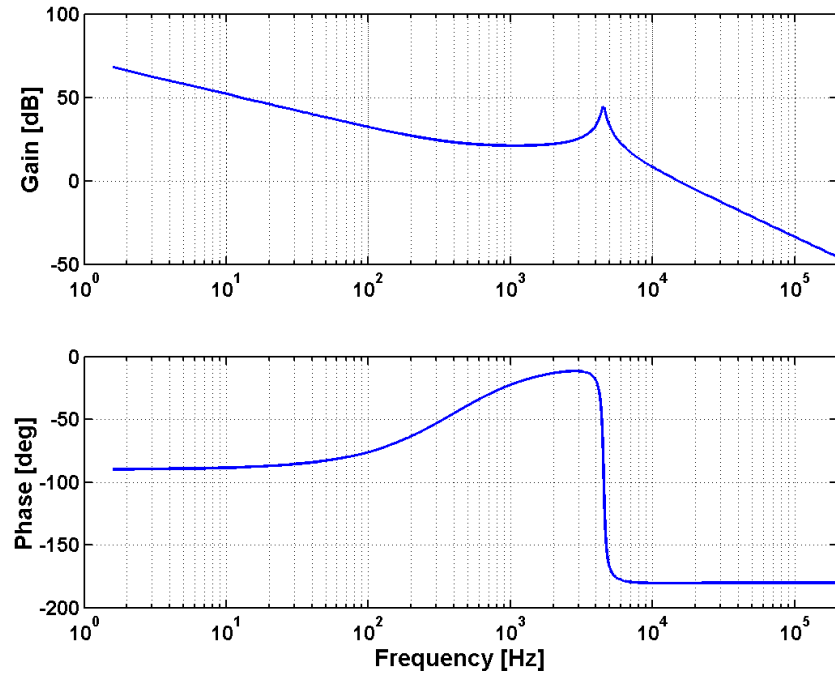


Figure 28. Bode plot of the open-loop control system

The closed-loop transfer function of the entire control system is now modeled, and the gains are implemented on a real controller. The lag-compensator is an ideal controller for this system. However, it is not easy to implement, as it requires a significant gain at the DC level, which often is difficult to implement in a physical system. Therefore, a controller that closely approximates the lag-compensator is desirable. A simple Proportional – Integrative (PI) controller performs this task extremely well. A PI controller contains a pole at the origin while the lag-compensator controller contains a small magnitude asymptotically stable pole (Ogata, 1997). Applying Equations (15) and (16), it is simple to convert the transfer function of the lag-compensator to gains for a P and I controller. Therefore, for the transfer function in Equation (14),  $K_p = 10$ , and  $T_I = 4\text{e-}5\text{sec}$ .

$$K_p = \alpha \quad (15)$$

$$T_I = \frac{1}{f_{c2}} \quad (16)$$

### **Controller Tuning**

A control scheme for the interferometer system is designed and must be tuned to achieve stability and the dynamic performance desired. The gains for the PI controller derive from the transfer function of a lag-compensator controller as described in the previous section. Since there are some significant differences between the analytic model and the real system, including the gains of the all-pass filter and multiplier, these initial

controller gains must be altered to achieve the best performance. The first step prior to tuning is to locate a representative location on the sample surface to tune with. Typically, the center of the vibrating portion of the MEMS device under test is used.

There are a number of well-documented tuning methods for PI and PID control, such as the Ziegler-Nichols method. However, the interference curve and its second harmonic are sinusoidal and, therefore, severe non-linearities exist outside of a small region of the curve. Hence, this Ziegler-Nichols method cannot be applied, as it requires an oscillating instability, which is often not possible in a non-linear system. Instead, the tuning performed for this system uses a less refined approach. A flowchart of this method is shown in Figure 29. First, the controller uses the initial gains from the theoretical and the response is viewed on an oscilloscope. If a steady-state error is present, the  $T_I$  is reduced to increase the amount of integration present, and the response is again viewed. This process repeats until the steady-state error is eliminated. Similarly, the  $K_P$  gain is adjusted by analyzing the stability of the response. If the response is unstable, this indicates that the controller is overshooting the setpoint and wrapping around the top of the sinusoidal curve. In this case, the proportional gain is reduced, as a smaller  $K_P$  allows the controller to stay within the bounds of the linear range of the second harmonic curve. The proportional gain is reduced until the system is stable and rejects external vibration. The downside to this method is that a wide range of proportional and integral gains satisfies these requirements.

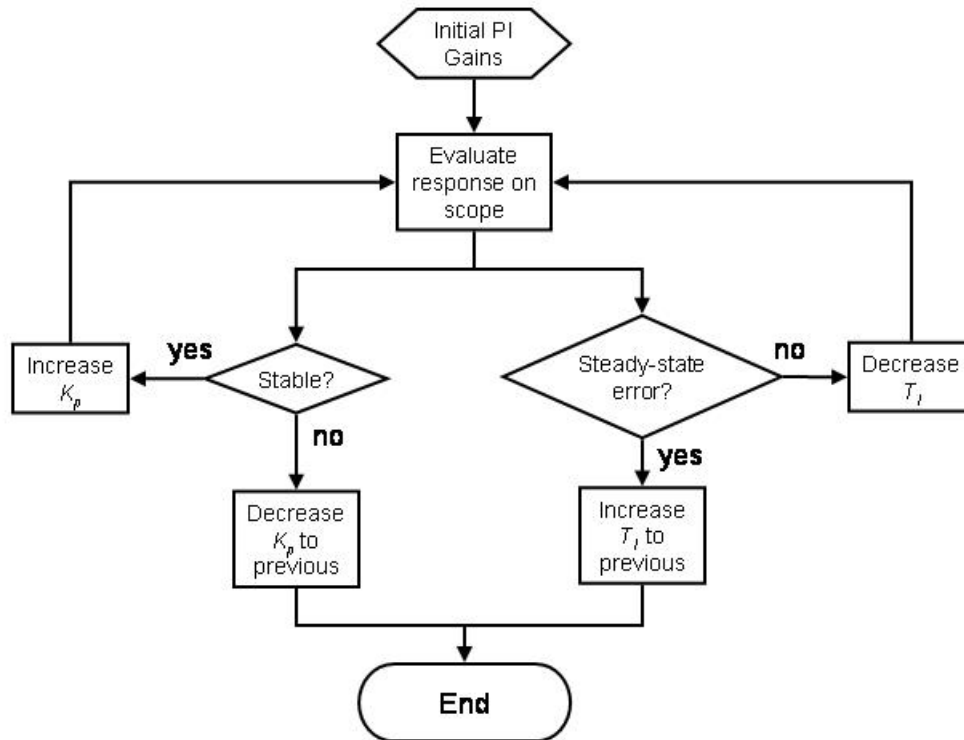


Figure 29. Control tuning flowchart

Further refinement of the controller gains is performed via two methods. The first method is via the evaluation of the responsiveness of the system to an external vibration. This external vibration comes from a rap of a fist to the top of the optical bench upon which the apparatus is placed. The gains are “tweaked” such that the responsiveness of the system is as fast as possible, i.e. the external vibrations last for the shortest amount of time on the oscilloscope screen. Using this technique, the gain parameters generated are:  $K_p = 0.5$ , and  $T_i = 5\text{e-}6$  sec. The major difference between these parameters and the theoretical gains is the decrease in proportional gain from 10 to 0.5. This change accounts for the constant gains of the other components in the lumped plant and sensor system.

The second method for refining the controller gains is more scientific. A Stanford Research Systems SR785 dynamic signal analyzer is connected to the photodetector output. An FFT of this signal is recorded with controller turned off as a baseline for measurement. The three measurements of interest are the magnitude of the first harmonic, the magnitude of the second harmonic, and the magnitude of the noise floor, as shown in Figure 30. Next, the controller is turned on and frequency spectra are measured for various levels of each of the two gain parameters. The results from a few of these measurements are tabulated in Table 2.

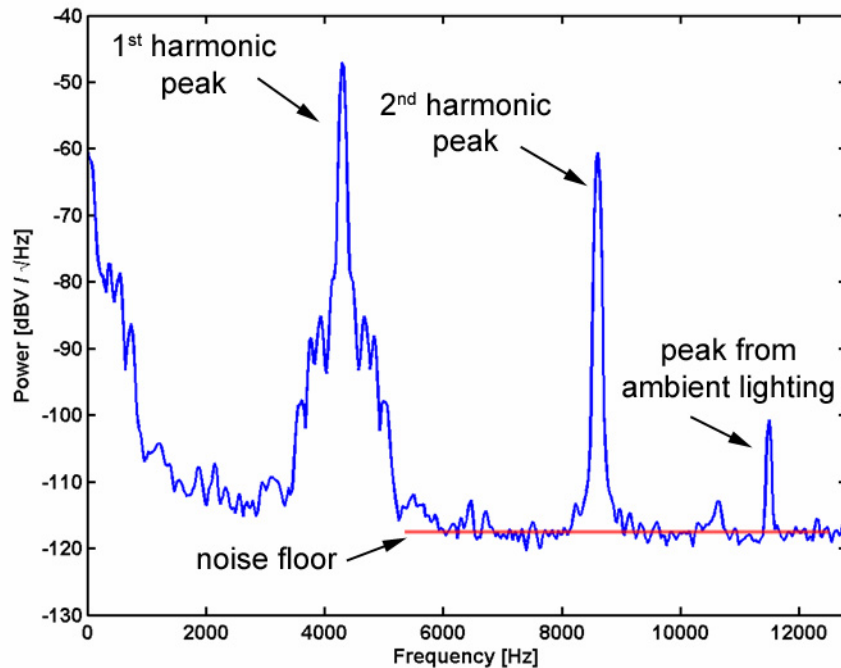


Figure 30. Frequency spectrum of uncontrolled system

Table 2. Performance of various gain parameters

Signal	S/N (peak $\rightarrow$ noise floor)	Ratio (1st harm $\rightarrow$ 2nd harm)
Uncontrolled	67.13 dBV/ $\sqrt{\text{Hz}}$	10.66 dBV/ $\sqrt{\text{Hz}}$
$K_P=0.5, T_I=5\text{e-}6$	60.24 dBV/ $\sqrt{\text{Hz}}$	43.35 dBV/ $\sqrt{\text{Hz}}$
$K_P=1.0, T_I=1\text{e-}5$	53.86 dBV/ $\sqrt{\text{Hz}}$	43.10 dBV/ $\sqrt{\text{Hz}}$
<b><math>K_P=0.2, T_I=2\text{e-}6</math></b>	<b>67.53 dBV/<math>\sqrt{\text{Hz}}</math></b>	<b>46.07 dBV/<math>\sqrt{\text{Hz}}</math></b>
$K_P=0.5, T_I=1\text{e-}5$	60.55 dBV/ $\sqrt{\text{Hz}}$	32.63 dBV/ $\sqrt{\text{Hz}}$
$K_P=0.5, T_I=1\text{e-}6$	59.72 dBV/ $\sqrt{\text{Hz}}$	34.82 dBV/ $\sqrt{\text{Hz}}$
$K_P=0.5, T_I=1\text{e-}4$	58.35 dBV/ $\sqrt{\text{Hz}}$	14.95 dBV/ $\sqrt{\text{Hz}}$

The initial hand-tuned gains are remarkably close to the best gains found using this technique, which are:  $K_P = 0.2, T_I = 2\text{e-}6$ . The goal of the control theory is to reduce the magnitude of the second harmonic ( $2\omega$ ), as this minimizes the second spatial derivative of the interference curve. This inflection point is the center point of the linear region of the interference curve and the optimal point for measurements. To quantify the performance of the controller, the ratio of the magnitude of first harmonic to the magnitude of the second harmonic is calculated. The greater the ratio, the better the controller performs. Using best performing controller gains, this ratio increases by over 36dBV/ $\sqrt{\text{Hz}}$ , which indicates that it forces the sensor to operate with a very small second harmonic, and hence in the linear region.

However, there are some deleterious consequences that come from using the controller. First, although the signal to noise (S/N) ratio increases slightly when the controller is in use, the noise floor is also somewhat increased (15dBV/ $\sqrt{\text{Hz}}$ ). Part of this stems from controller locking onto the most sensitive region of the interference curve, hence increasing the power present throughout the entire spectrum, including the noise. However, it is possible that the controller is also introducing some broadband noise into the system, which is a logical consequence of using a digital signal processor. Also, in

all measurements with the controller turned on, a discontinuity exists in the power spectrum at around 10.5kHz. The source of this discontinuity is unknown and may inhibit the sensor from detecting motion in this frequency range. Finally, there are inherent limitations to these techniques. First and foremost, a truly optimal set of gains cannot be obtained through the subjective measurements that are presented in these methods. Secondly, the signal to noise of the uncontrolled system must be high enough to provide a good correlation between the input and output signals.



## **CHAPTER V**

### **EXPERIMENTAL SETUP AND PROCEDURES**

The control system and its implementation, including some of the physical hardware and setup, is described in the previous chapters. This chapter discusses the remainder of the mechanical setup, the capture and routing of the electronic signals, and the processing performed on those signals. Finally, calibration techniques for the hardware components including the optical focus and the measurement sensitivity are presented in this section.

#### **Hardware Setup**

The mechanical system is built atop a five foot by eight foot Melles Griot StableTop 250 passively damped optical table. Figure 31 shows the compliance curve for this optical table. This type of table is well suited for limiting the impact of mechanical vibrations in the frequency range under 100Hz. The majority of the electronic components are mechanically isolated from the table by placing them upon a freestanding shelf unit located above the optical table. It should be noted that the system described in this thesis shares this large optical table with a few other research projects, although the impact from these systems is negligible upon the performance of this system.

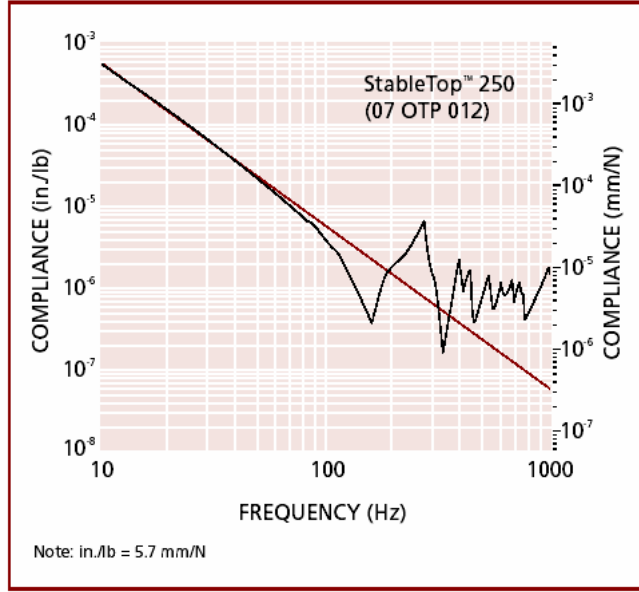


Figure 31. Optical table compliance graph (Melles Griot, 2004)

### **Sample and Micrograting Fixtures**

As discussed in Chapter IV, the sample under test is mounted on a PZT stack (Figure 20), which is rigidly fixed to a three-axis Newport 460A Series linear stage. A Newport CMA-222CL miniature stepper motor drives each axis, and allows for programmatic control. In addition to these three axes of motion, this linear stage system mounts atop a Newport 37 Series two-axis tilt stage, giving a total of 5 degrees of freedom for the sample fixture. The focal distance of the micrograting interferometer sensor is estimated to be 800 $\mu$ m; therefore, the sample is initially placed this distance away from the sensor. The micrograting is rigidly fixed to another three-axis linear stage atop two tilt stages, for five degrees of freedom for the sensor.

### **Optical Setup**

A 4mW JDS Uniphase 1122P helium-neon (HeNe) laser provides the light source for the experiments described in this thesis. The beam diameter of this laser,  $y_1$ , is

630 $\mu\text{m}$ , and the optical wavelength is 632.8nm. The light emitted from the laser passes through a converging lens with a focal length of  $f_1 = 88.8\text{mm}$ , as shown in the ray tracing diagram in Figure 32. The micrograting is placed on the divergent side of the focused beam, which creates a spot size of around 200 $\mu\text{m}$  in diameter. A portion of the beam is then diffracted back to the photodetector, while the remainder passes through the grating. On the backside of the grating, an aperture insures that the beam is no larger than 200 $\mu\text{m}$ . Finally, the microfabricated lens, which has a focal distance of around  $f_2 = 800\mu\text{m}$ , focuses the beam into a spot size of around 500nm, which is one of the limiting factors in the resolution of this system. A schematic of this setup is shown in Figure 33.

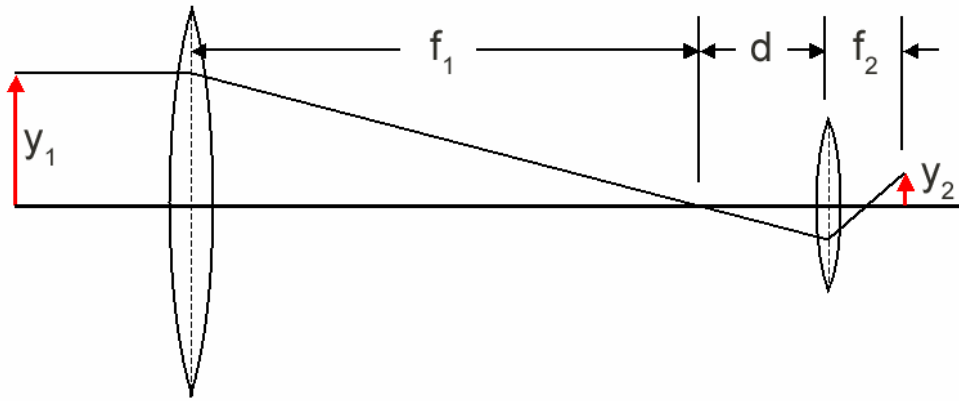


Figure 32. Ray tracing of the laser beam through the optical system

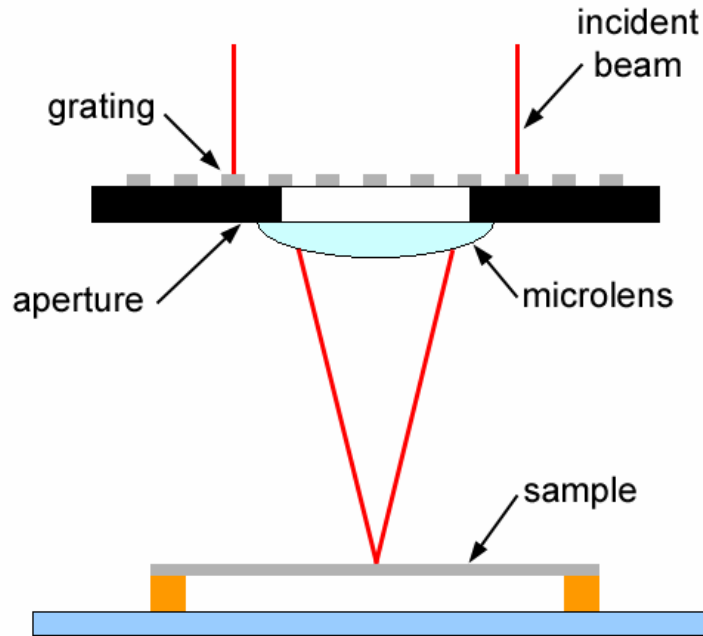


Figure 33. Schematic of the grating and microlens setup

The first diffraction order passes around the outside of the primary converging lens and is picked up by a photodetector located approximately 50cm away from the stages. The photodetector converts the light into voltage, which is viewed on an oscilloscope. An analog to digital converter (ADC) records this voltage signal. The signal contains the modulated intensity information of any motion detected by the sensor. The motion comes from the 40nm control signal, the motion of the MEMS device under test, and any mechanical vibrations present in the system.

### **Software Setup**

Two primary software packages are used for the development and testing of this system, LabVIEW and MATLAB. LabVIEW is a graphical development package created by National Instruments that allows for fast and intuitive creation of software for

data collection and analysis. MATLAB is produced by MathWorks and utilizes a scripted programming language to perform data analysis and to display the results. Often, National Instruments hardware in conjunction with LabVIEW records the data and performs some basic analysis. These data are written to a file then passed to MATLAB for further analysis and display.

### **Motion Control**

In the previous chapters, the discussion of controlling the path difference between the sample and the sensor was discussed along with the method for locking on to the most sensitive region of the interference curve. A measurement taken with a properly tuned controller yields the out-of-plane displacement of microscale device. However, this measurement is for a single surface point, which is essentially a one-dimensional measurement. In order to generate true three-dimensional metrology data sets, a two-dimensional scan over the surface of the device is implemented while recording the out-of-plane measurements. The motorized linear stages are programmed in conjunction with the data acquisition hardware to automate the process of collecting this information. Thankfully, these motors and stages integrate well together, and the motor driver provides a software interface that allows it to be accessed via LabVIEW.

There are many ways to collect data sets over a surface area. The method of continuous movement and data collection allows for the largest data throughput; however, the actuation of the motors creates undesirable vibration and out-of-plane motion of the sample and, hence, is rejected as a useful technique. The simplest point by point method is a raster scan, as shown in Figure 34 (a). In this method, data are taken at the initial start point, shown with a green circle, after which the sample is moved a

distance  $\Delta X$ , whereupon another data point is taken. This process repeats until the sample moves the total scan distance,  $X_s$ . The sample then moves a distance  $\Delta Y$ , and another row of data are taken. This process continues until the entire vertical scan distance,  $Y_s$ , has been covered, and the sample returns to the initial start point. This is done so that when multiple scans over the same portion of the surface are made, the sample position does not have to be manually reset. While this type of scan is fairly trivial to implement, a backlash problem is noted in the shifted rows of composite image, such as the one shown in Figure 35.

To combat this problem, a technique is taken from the machining industry. The basic premise of this method is to always proceed in the same direction while taking data. To implement this technique, once a row has been scanned, the scan location overshoots the target point by a distance,  $d$ , as indicated by the orange circle in Figure 34 (b). This means that the motors and stages are always reversed twice when completing the end of the row, which eliminates any backlash that may be present. The obvious consequence of this technique is that it takes longer to complete a scan, as the stages travel a greater distance; however, for scan of any significant size, this increase in scan time is negligible.

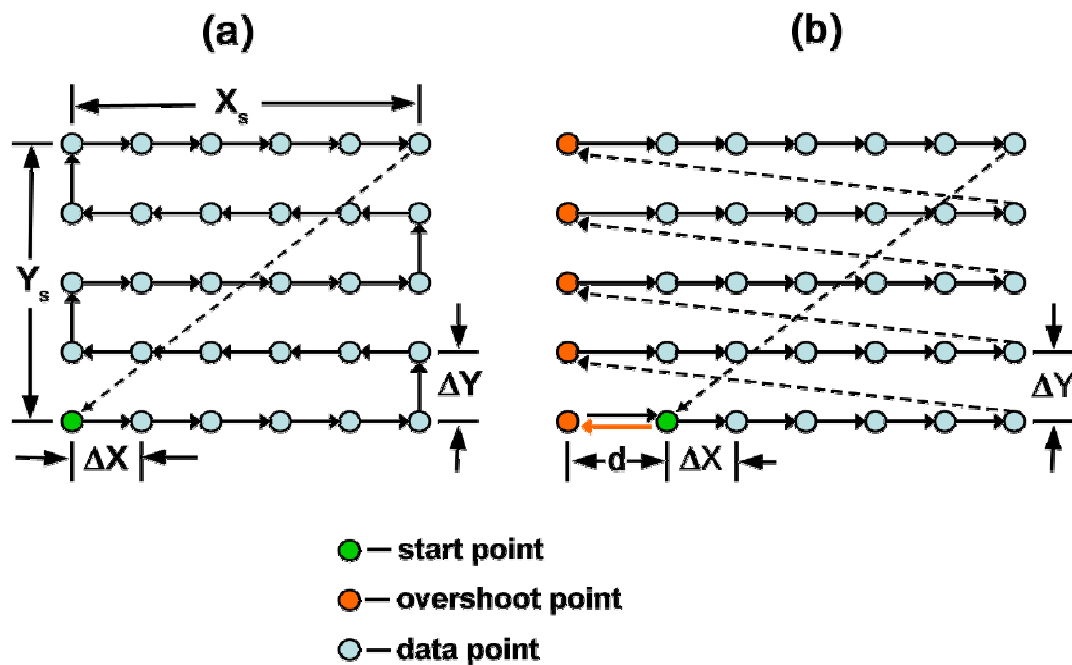


Figure 34. Raster (a) and overshoot (b) method of surface scanning

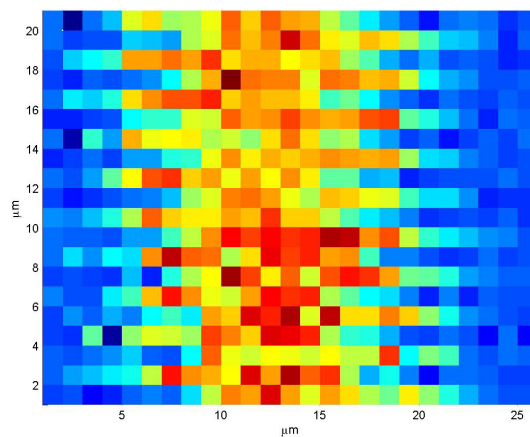


Figure 35. Surface scan showing backlash problem

## **Data Acquisition**

At each data point in Figure 35, three channels of data are acquired using a 12-bit National Instruments 7115 DAQ card. The maximum acquisition rate is 10 million samples per second; however, as with most A/D converters this throughput is multiplexed over all acquired channels. Therefore, for three channels to be acquired simultaneously, the maximum sample rate is 3.33 million samples per second. The card has an analog input range of  $\pm 10\text{V}$  and a full range resolution of 4.9mV. Yet, if the full range is not used, the resolution of the card is reduced to 0.24mV. Typically, only small amounts of data are recorded for each surface point, but this is dependent upon the MEMS actuation frequency.

The flowchart of the entire scanning procedure is shown below in Figure 36, and a screenshot of the LabVIEW block diagram that executes this routine is shown in Figure 37. Once the data acquisition parameters are set, the program initializes the motors for the scanning stages. The data acquisition card then allocates the memory buffer required for the operation and waits for a trigger signal to begin recording data. Often times a number of buffers are recorded for a single data point on the surface. These buffers are averaged to minimize the impact of erroneous data and reduce the noise present in the data. The three channels of voltage data recorded are the input to the PZT, the photodetector signal, and the value of the analog second harmonic signal that comes from the low-pass filter (Figure 18). For the latter two signals, only the DC (or mean) value of the voltage over the entire data set is useful, as there is no frequency dependent portion of this data set. The DC value of the input to the PZT contains the information about the static height of the surface, regardless of its dynamic motion. The photodetector signal



contains a great deal of useful information. It passes through a fast Fourier transform (FFT), which is used to measure the magnitude of the signal at various frequencies. Two frequencies are of particular interest: the control signal actuation frequency, typically 4.3kHz, and the MEMS device actuation frequency. The user selects two narrow bands that are used to estimate the peak magnitude within these frequency ranges. As discussed in the previous chapter, the magnitude of the modulation frequency is useful for compensating for changing surface reflectivity. The magnitude of the MEMS device actuation frequency yields the peak to peak amplitude of the out-of-plane motion of the MEMS device. Additionally, the phase of the MEMS device is calculated from the FFT. Therefore, a total of six data sets are generated from these three channels. They are written to a file, and all are viewable in real-time on the user interface of the LabVIEW program, as shown in Figure 38.

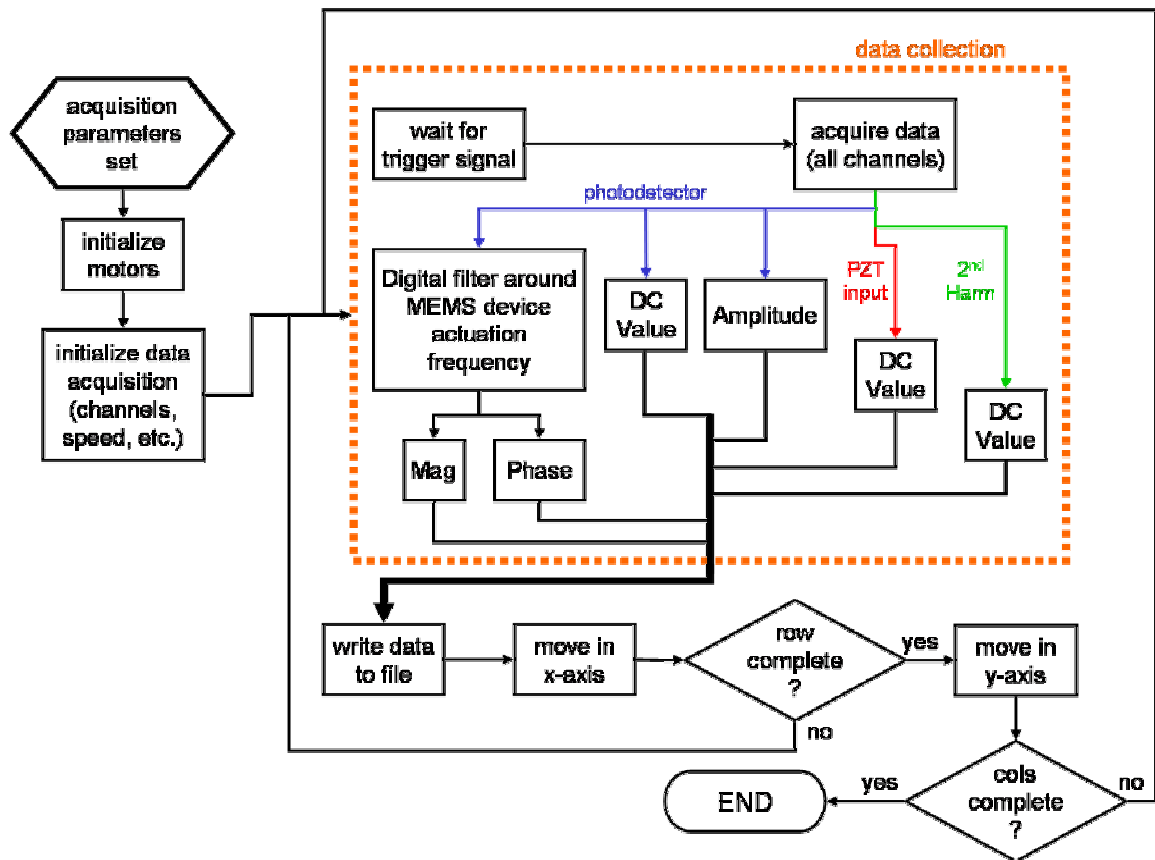


Figure 36. Flowchart for LabVIEW scanning program



## **Control Software**

The control technique used in this system uses a field programmable gate array (FPGA) processor created by National Instruments. The interface with this processor is fairly unique. The FPGA operates much like a DSP. Compiled code must be downloaded to the FGPA through a mini-PCI interface each time the code is modified. The FPGA runs autonomously from the host PC on a fixed clock, providing a stable platform for real-time operations. However, the processor can also be programmed to transmit some data to the host PC. The benefit of this system is that the FPGA performs many fixed point calculations simultaneously while offloading some data operations where floating point arithmetic is preferable. Typically, these offloaded tasks are not used for real-time control and instead are more useful for display and analysis, such as Fourier transforms. Also, the PC can be used to display and interact with a graphical user interface, such as the one shown in Figure 39.

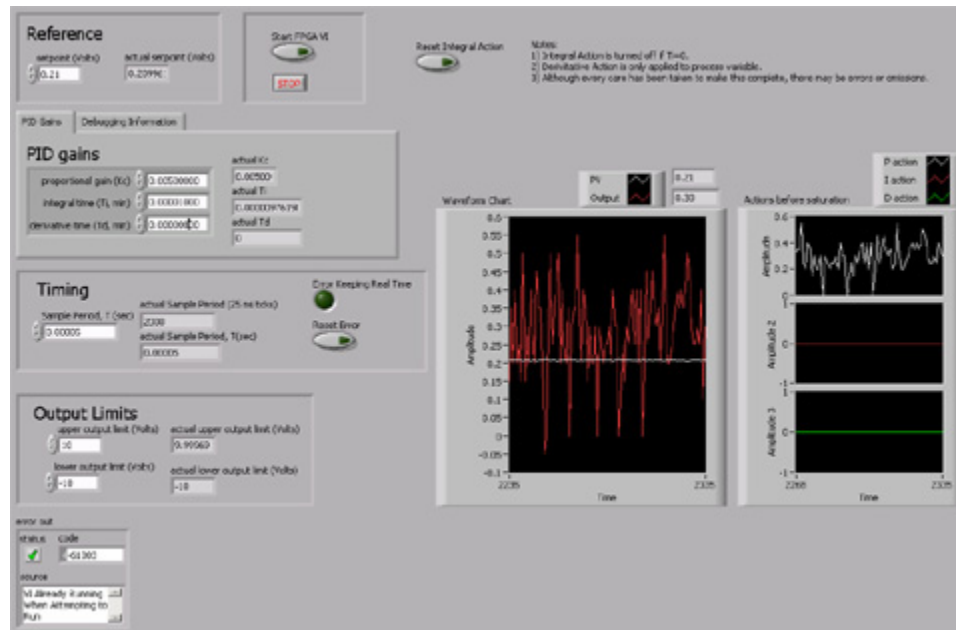
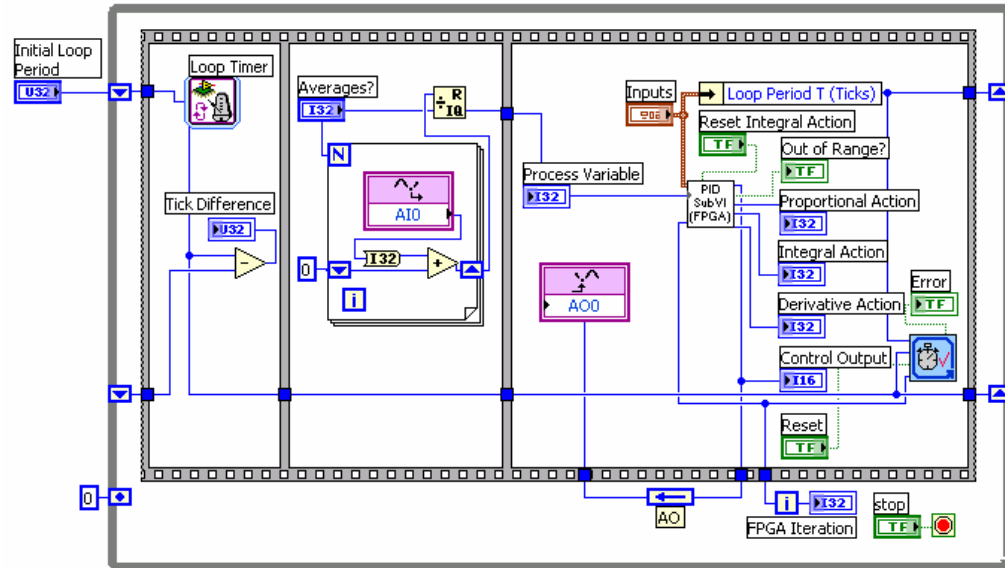


Figure 39. Screenshot of the FPGA UI

The PI controller design described in the previous chapter is subset of a full PID algorithm programmed on the FPGA device. National Instruments provides an easy to use toolkit for the FPGA that is integrated into LabVIEW, as well as many sample programs. Using this toolkit, developing programs for the FPGA is simple and straightforward. The types of operations performed by FPGA are fairly limited, and the programmer is forced to recognize the fixed point limitations of the FPGA, although the toolkit provides a number of methods to combat the rollover problems inherent in fixed point arithmetic. A screen shot of the LabVIEW PID controller block diagram which runs on the FPGA is shown in Figure 40.



The algorithm itself is a modified version of a sample program provided by National Instruments (Humberstone, 2003). A flowchart of the algorithm is shown in Figure 41 and the LabVIEW block diagram of this algorithm is shown in Figure 42. Within the user interface, which runs on the host PC, the loop period,  $T$ , and the gains,  $K_P$ ,  $T_I$ , and  $T_D$ , are selected. A setpoint,  $SP$ , is established for the controller to compare against, and the analog input and output channels are initialized, which begins the controlling action. The proportional action,  $A_P$ , utilizes the error between the process variable and the setpoint as shown in Equation (17). The integral action is a bit more complicated. Trapezoidal integration is applied to the current process variable and the process variable from the previous iteration, as shown in Equation (18). The derivative action is similar to the integral action; however, the action only uses the process variable itself, and not the error, as shown in Equation (19). Finally, the three actions sum

together and the total passes to the digital to analog converter, which converts the unsigned 32-bit number to a voltage within the specified range.

$$A_p = (PV_{curr} - SP) K_p \quad (17)$$

$$A_I = \left( \frac{(PV_{prev} - SP) + (PV_{curr} - SP)}{2} \right) \frac{K_p * T}{T_I} \quad (18)$$

$$A_D = (PV_{prev} - PV_{curr}) \frac{Kc}{T} T_D \quad (19)$$

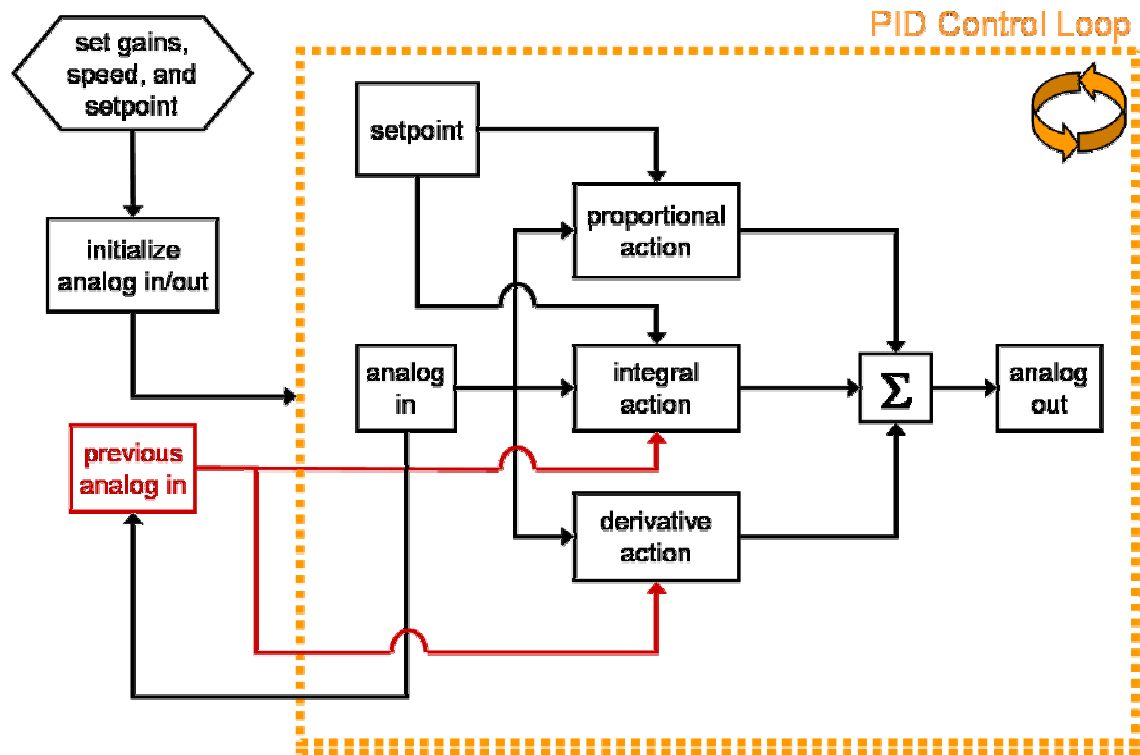


Figure 41. PID control flowchart

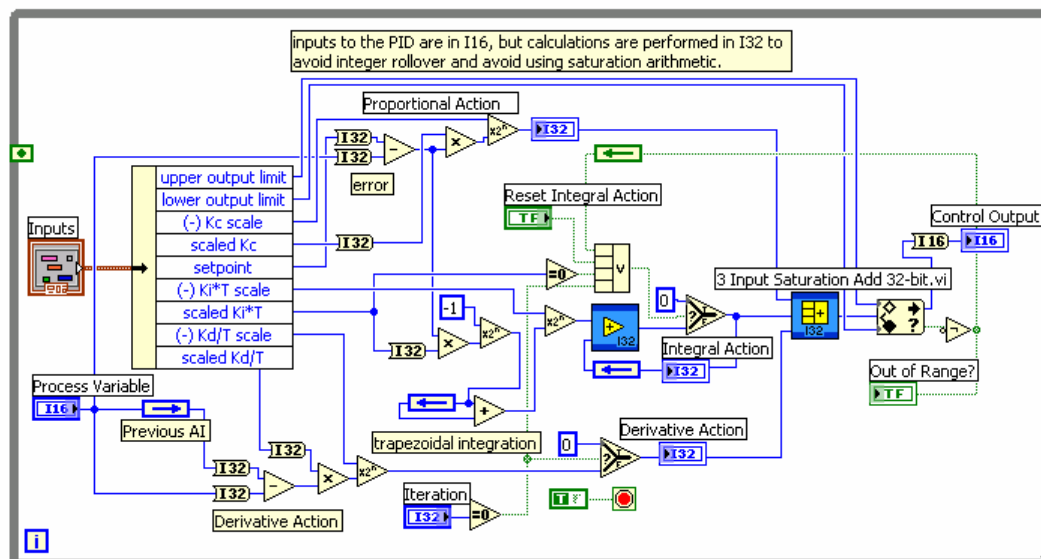


Figure 42. Screenshot of the PID sub function block diagram



## **Experimental Procedures**

A crucial aspect for generating meaningful and accurate data is the creation of consistent testing and setup procedures. In addition, calibration routines must be run each time the system is altered in any way in order to insure that the scaling from photodetector voltage to displacement is accurate. As stated in previous sections, the number of degrees of freedom for this experimental system is considerable, and fine tuning each one in order to maximize the response of the system is a tedious and time consuming process. Once the setup is performing consistently, care is taken not to alter or disturb the alignment.

### **Focus Determination**

In this experimental system, the final spot size of the laser beam on the surface is critical to achieving a high resolution. Subsequently, the ability to adjust the focus of the laser beam is of utmost importance. The two parameters of interest in this adjustment are the distance between the first converging lens and the diffraction grating and the distance from the converging microlens to the sample surface.

The first converging lens is an off-the-shelf commercial component and its focal distance is a known quantity. Therefore, the focus is fairly easy to calibrate. The goal of this lens is to reduce the spot size such that nearly all of the light intensity is incident upon the diffraction grating. To measure this quantity, the far-field image of the grating is projected upon a piece of paper. The lens is moved towards the grating until the fewest number of grating fringes are imaged. This represents the point where the grating is at the exact focal point of this lens. In order to insure that the beam is divergent as it enters the grating, the distance is increased slightly, and the position of the lens is then locked.

Similarly, the x and y positions of the diffraction grating and microlens are optimized in the same manner.

The focus position of the microlens is more difficult to locate. The lens is manufactured using a recently developed technique and the exact focal length of each particular lens is unknown (Kim, 2003). An estimated focal length of 800 $\mu\text{m}$  is derived from the size of the lens and its curvature, and these data are used as the initial starting position. With a focal distance this short, the range of focus where the spot size is suitable for imaging is fairly small. To isolate the region where the depth of focus is suitable, the system scans a position on the quartz wafer with microscale traces. These traces are aluminum and are patterned via a lift-off process, which leaves a fairly sharp edge. The substrate is optically clear; therefore, the surface of the trace is much more reflective than the substrate. As the sample moves closer to the sensor in the z direction, the system records the surface reflectivity, using the procedure discussed in the previous chapter. A single row of data points is taken for each successive step toward the sensor. The position of highest reflectivity indicates where the spot size is the smallest and, hence, the position where the microlens reaches its focal point. An image of this experiment is shown in Figure 43.

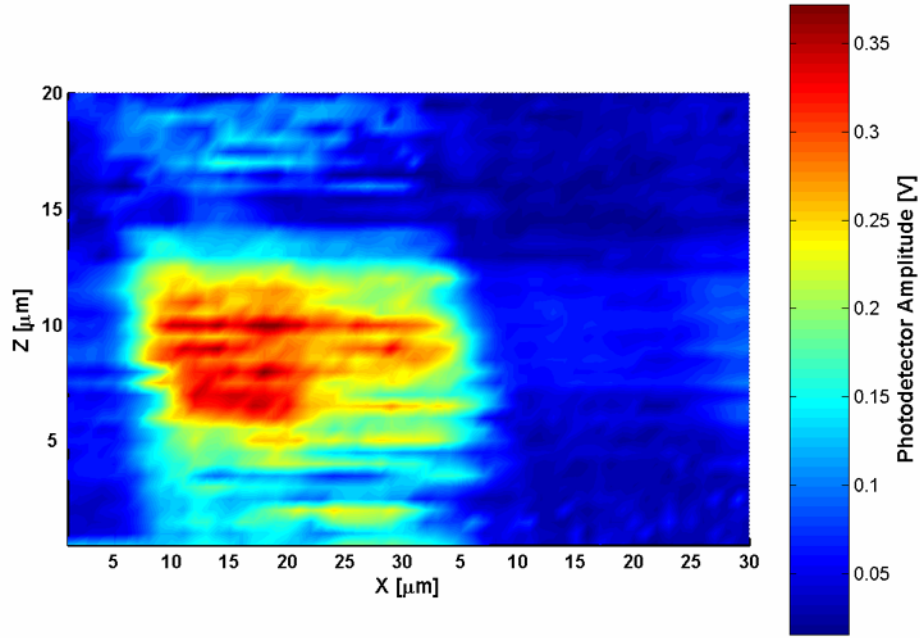


Figure 43. Amplitude of the photodetector signal showing peak focus intensity

### **Reflectivity Calibration**

The procedure used to calibrate the focal distance for the microlens is also used to correct for the changing reflectivity of the sample surface. The PZT is actuated with constant amplitude of 40nm. Assuming that the controller keeps the interferometer in the linear range of the interference curve, the amplitude of the interference signal detected by the sensor should also be constant. However, this is not always true, as different points on the surface of the sample have different reflectivity, which would cause the intensity of the light at the first diffraction order to fluctuate. This fluctuation affects the levels of the other signals derived from the photodetector, namely, the magnitude of the MEMS device actuation displacement. Therefore, the maximum amplitude of the control frequency detected across the surface of the sample is used as point of maximum reflectivity. It is assumed that the reflectivity is linearly proportional to the amplitude,

and therefore the rescaling factor shown in Equation (20) is used to generate more accurate displacement measurements. This creates more accurate deflection measurements.

$$M_{new} = M_{old} \left( \frac{A_{max}}{A_{pt}} \right) \quad (20)$$

### **Sensor Specifications**

The operational limits and capabilities of any metrology tool define its usefulness and applicability. The most useful sensors have a large dynamic range, a high bandwidth, a low signal to noise ratio, and a high sensitivity. Metrologists who develop new sensors strive to achieve these goals, as they are the driving factors for adoption in the marketplace. In this thesis, the diffraction grating interferometer system has been described in terms of the operating principles, the control technique, design and implementation, the hardware and software interfaces, and the experimental procedures. As a cohesive whole, the scanning interferometer system is a tool capable of creating measurements of the out-of-plane movement of a MEMS device across a defined scanning region. The limits of this sensor system are described in the following section.

#### **Bandwidth**

Any commercial sensor that measures dynamic data will list the bandwidth of the sensor. Typically, this is defined as the frequency where the gain of the sensor drops 3dB below its nominal capacity. The bandwidth is a function of the actual sensing element, as well as the electronics and signal processing equipment used in conjunction with the

sensor. The sensing element in the micrograting interferometer is a microfabricated photodetector. This device is a PN junction diode that operates in the reverse bias region. The current produced at this junction is proportional to the light intensity incident upon the junction (Bechwith, 1995). This current is amplified by a current amplifier chip and converted into a voltage, which is recorded by the analog to digital hardware.

The bandwidth of the photodetector used in this system is quite high and can record signals up to 2MHz (Lee, 2003). Along with the 10 million samples per second capability of the ADC used, the highest frequency signal that can be recorded by this system is 2MHz, although a sample frequency of 4 to 5 times the highest frequency to be detected is preferable.

The control system on the other hand has much less bandwidth than the system as a whole. The second harmonic lock-in technique utilizes frequency modulation and demodulation to determine the magnitude of the second harmonic present in the photodetector signal. Via convolution, this magnitude is shifted to the DC level and a low-pass filter allows only the frequencies around the second harmonic to affect this magnitude. Therefore, the bandwidth of this control scheme is limited to the bandwidth of this low-pass filter. Typically, this filter has a cut-off frequency of 300Hz, such that only vibrations under this cut-off frequency are actively controlled.

The speed of the control loop would necessarily have to be greater than this cut-off frequency. The maximum loop frequency of the PI control algorithm implemented on the FPGA controller is 150kHz, a limitation imposed by the amount of logic that the controller uses onboard the FPGA. The FPGA itself has a clock speed of 40MHz, but obviously the PI control technique requires quite a few calculations, as indicated by the

flowchart in Figure 41. Therefore, the bandwidth of the controller can be much greater than the 300Hz cut-off frequency of the low-pass filter; however, for this experimental setup, this is the effective bandwidth limitation of the controller.

### **Signal to Noise Ratio (S/N)**

The signal to noise ratio of any sensor is vitally important for many dynamic measurements. This specification gives the ratio between the magnitude of the signal of interest and the background noise level. A sensor with a large S/N ratio is able to pick up faint signals and be used in applications where the noise sources cannot be controlled or reduced. These noise sources vary considerably and can include mechanical, thermal, electrical, electromagnetic, and shot noise. The primary sources of noise in the system described in this thesis are from mechanical and electromagnetic sources. The shot noise for the photodiode is negligible for the frequencies used in this experiment, and the relative intensity noise (RIN) from the HeNe laser is also negligible compared to other sources (Lee, 2003).

From Table 2, the S/N ratio for the uncontrolled system is 67.13dBV/ $\sqrt{\text{Hz}}$ . Using the best gains for the PI controller, the signal to noise ratio increases only 0.40dBV/ $\sqrt{\text{Hz}}$  above an uncontrolled system. Therefore, the S/N is only a very weak function of the controller, and, generally, the S/N ratio for this sensor is around 67dBV/ $\sqrt{\text{Hz}}$  regardless of controller activity. This level of noise is reasonable for a metrology tool; however, there are methods that can be used to increase the fidelity of the sensor such as electromagnetic shielding and acoustic enclosures.

### **Vertical (Out-of-Plane) Resolution**

The resolution of any sensor is dependent upon a few factors including the hardware limits of the mechanical system as well as limits imposed by the sensor electronics. With the advent of digital computation and floating point arithmetic, the number of bits of the analog to digital converters (ADC) has become one of the limits of the resolution of metrology systems. Increasing the number of bits used in an ADC significantly increases the complexity of the circuitry, and greatly increases the cost of the devices. For the 12-bit ADC used in this system, the full-range resolution of the sensor is 5mV, although this range can be reduced such that the resolution is brought down to 0.24mV.

An estimate of the vertical resolution of the sensor is generated from the sensitivity within linear region of the interference curve, as shown in Figure 12. The slope of this region yields the scale for the measurements taken with this system. Figure 44(a) shows an experimentally generated interference curve, and Figure 44(b) shows a zoomed in view of the linear region of this curve. The specifications of the PZT state that the actuator moves 100nm per Volt (NEC / Tokin, 2003). This can be verified in Figure 44(a), as the interference peak repeats every  $\lambda/2$ , or 316.4nm, which correlates to approximately 3.2V applied to the PZT. Therefore, the PZT is assumed to be linear in this actuation range, and the slope of the interference curve within the linear region is 235nm/V. Using the best resolution on the ADC, this yields a theoretical resolution of less than 0.058nm at the lowest bit of the ADC.

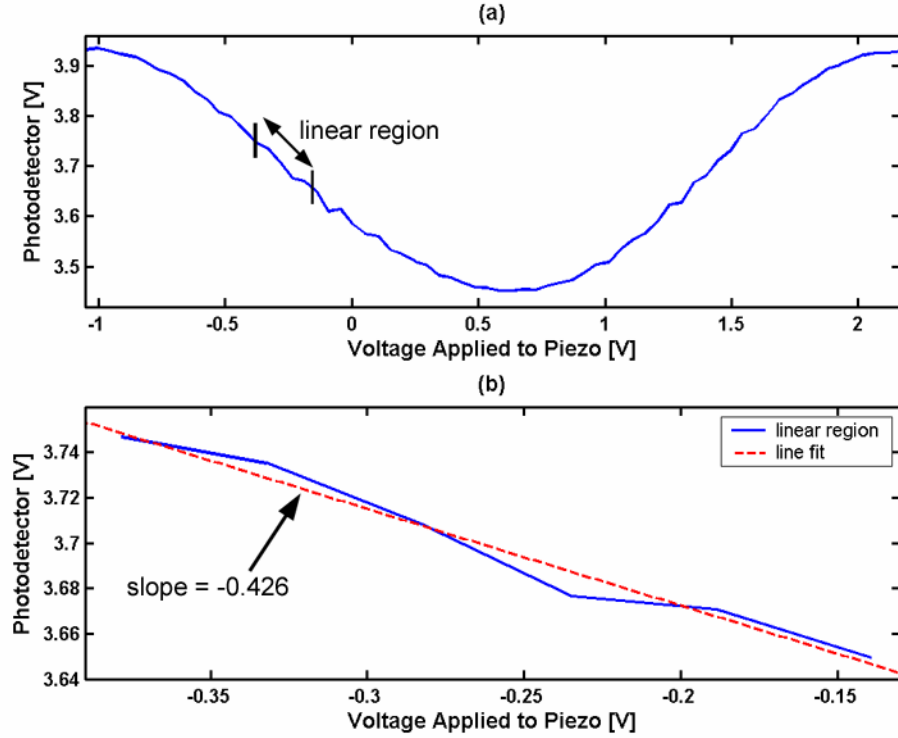


Figure 44. Interference curve (a) and a zoomed-in view of the linear region (b)

However, it is still possible that the theoretical maximum resolution may not be achievable due to noise. The S/N for this system is estimated to be  $67\text{dBV}/\sqrt{\text{Hz}}$ . This indicates that a signal of interest is approximately 2240 times greater in magnitude than the baseline noise. From Figure 44(a), the signal of interest is the peak to peak voltage of the interference curve, or approximately 0.51V. The noise present for a signal of this magnitude is therefore 0.23mV, which is nearly identical to the resolution of the ADC (0.24mV). Therefore, the noise within the system renders the last bit of the ADC useless, making it effectively an 11-bit ADC. Thus, the real achievable out-of-plane resolution for this system is approximately double the theoretical value, or approximately 0.12nm, which is above the level of wavelength drift in the HeNe laser (JDS Uniphase, 2003).



### **Horizontal (In-Plane) Resolution**

The horizontal resolution of this metrology system cannot be analyzed using the same technique as the vertical resolution. The in-plane measurements are a function of the motors and stages used in the sample fixture as well as the spot size of the laser light. As discussed in a previous section, the stages and motors exhibit a significant amount of backlash, necessitating a refinement of the scanning technique. The Newport motors used are micro-stepper motors with optical encoder feedback. A Newport ESP6000 controller manages the motion and provides an easy to use interface. According to the manufacturer specifications, the resolution of this system is  $0.0488\mu\text{m}$ , however, the smallest incremental motion for these stages is  $0.2\mu\text{m}$  (Newport, 2004). Therefore, the best resolution that can be obtained during a scan must be at least  $0.2\mu\text{m}$ .

The size of the optical spot on the surface has a large impact on the horizontal resolution of the system. When the beam enters the microlens, it has a diameter of  $200\mu\text{m}$  due to the aperture. The microlens focuses this spot down to approximately  $2\mu\text{m}$  (Kim, 2004), and, therefore, this should be the limiting factor in the horizontal resolution. The same test that refined the focus of the microlens (Figure 43) is used to determine the horizontal resolution of the sensor. The step size in the x direction is set to  $0.25\mu\text{m}$ ; thus, the edge of the trace should be a sharp step due to the inability for the sensor to pick up surfaces at an angle to the laser beam. If a rounding of the edge is detected, this indicates that the spot lies partially on both the trace and the substrate and is used as the estimate for the lateral resolution. A cross-section of the trace is shown in Figure 45. In photolithographic processes, the line-width resolution is defined as the distance required for a vertical step to move from 5% of the height to 95% of the height. This determines

the minimum spacing required to distinguish between two lines. Utilizing this criterion, the horizontal resolution of the micrograting interferometer system is approximately  $3.6\mu\text{m}$ . Table 3 displays a comparison between the interferometer system described in this thesis and a commercial stroboscopic white light interferometer.

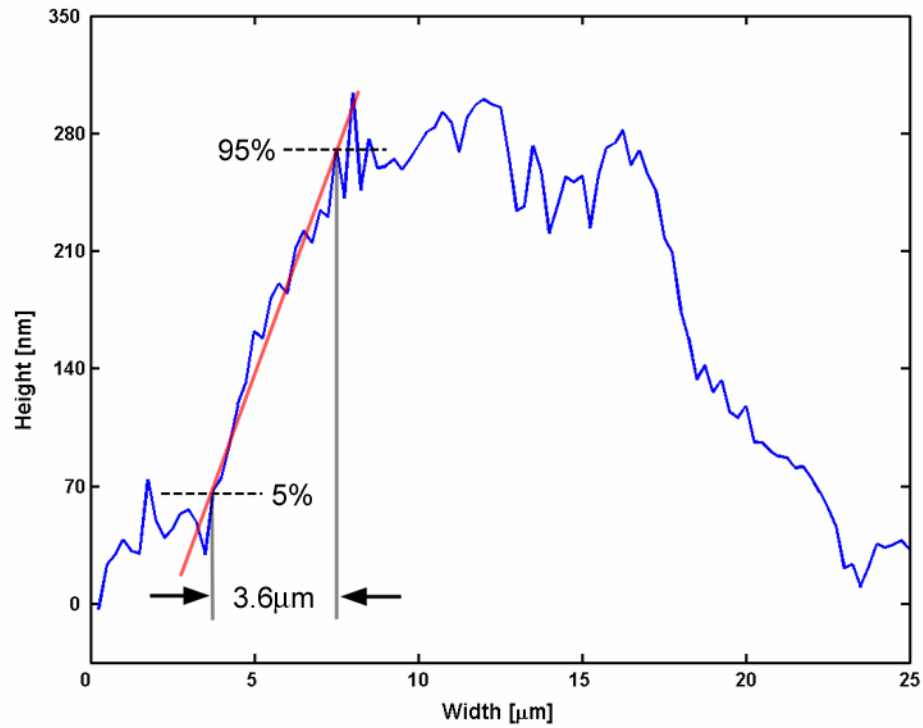


Figure 45. Cross section of a metal trace showing horizontal resolution

Table 3. Specification comparison between the metrology system described in this thesis and a commercial stroboscopic white light interferometer

Metrology System	Bandwidth	Vertical Resolution	Horizontal Resolution
Actively Controlled Diffraction Grating Interferometer	2MHz	0.12nm	$3.6\mu\text{m}$
Veeco Stroboscopic White Light Interferometer	1MHz	0.2nm	500nm

## **CHAPTER VI**

### **CASE STUDY AND RESULTS**

This thesis describes the theory and performance of a diffraction grating interferometer with active control. In previous chapters, the capabilities of the sensor system have been described, including the bandwidth and the resolution. This chapter discusses the results generated from this metrology tool, including proof that the controller improves the performance of the sensor system as a whole through the reduction of the mechanical vibrations and the ability to lock onto the linear region of the interference curve.

#### **Controller Results**

The reduction in the second harmonic magnitude is used as the final step for tuning the controller gains. This reduction takes place by first determining the proper setpoint of the second harmonic ( $2\omega$ ) signal. A slow ramp of the voltage is applied to the PZT, which yields an interference curve as shown in Figure 46(a), as well as a second harmonic curve as shown in Figure 46(b). In this case, the setpoint for the controller is set at 0.30V. Typically, this type of experiment is performed whenever the alignment is changed to insure that the analog lock-in circuitry is performing properly and the interference curve is not distorted.

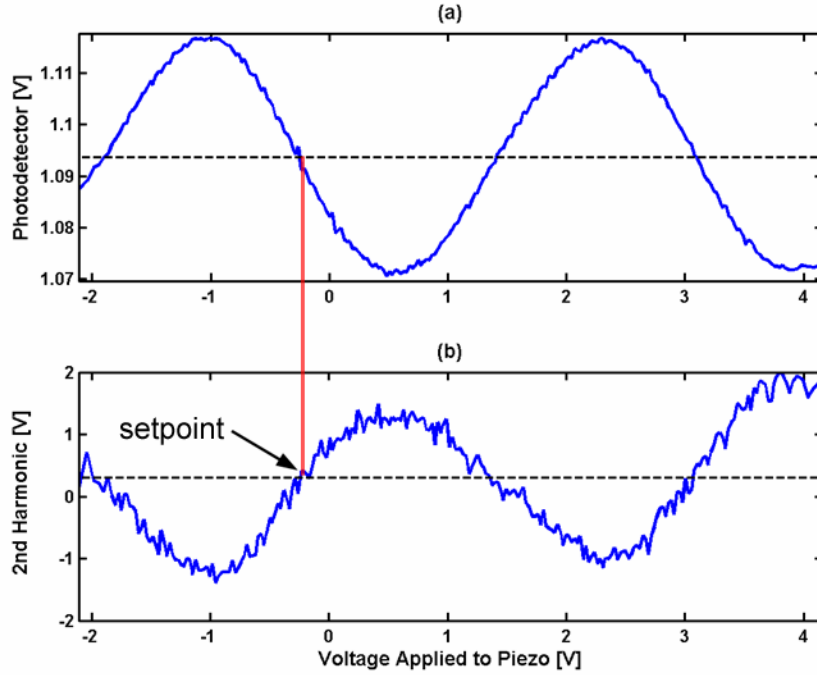


Figure 46. Photodetector (a) and analog 2<sup>nd</sup> harmonic (b) signals with process variable setpoint indicated

To show that the controller is working properly and increasing the sensitivity of the sensor system, an experiment is conducted where the three signals of interest are recorded over an extended period of time. A MEMS device is placed under the sensor and activated at a frequency of 700kHz. The photodetector output contains this modulation along with the lower frequency control signal and any mechanical vibrations that affect the system. Every tenth of a second, for 500 seconds, the photodetector signal and the analog second harmonic signal are recorded. The magnitude of the MEMS device actuation is determined by taking an FFT of the interference signal and recording the 700kHz magnitude. Similarly, the magnitude of the second harmonic of the PZT modulation signal can be determined in the same manner. Figure 46 shows the results of this experiment with the controller turned off (green), and with the controller functioning

(blue). Figure 46(a), shows the fluctuation of the analog second harmonic signal, which is used as the process variable for the controller. Obviously, with the controller active, this parameter remains constant through time, indicating that the controller adjusts the distance between the MEMS device and the sensor such that this parameter is kept at the setpoint. Figure 46(b) shows the magnitude of the second harmonic signal calculated from the FFT. Again, with the controller actively controlling the path difference, this parameter is held constant. The minimum of this parameter while uncontrolled is zero indicating that no second harmonic is present in the photodetector output. However, the controlled signal is not at zero, indicating that improvement can be made to the process variable setpoint to further reduce this magnitude. The shape of the green curve in Figure 46(a) and Figure 46(b) are quite similar, with the exception that the FFT takes the absolute value of the second harmonic. If the negative portions of this curve are flipped to the opposite side of abscissa, the curve would be identical.

The plot in Figure 46(c) shows the magnitude of the MEMS device motion. Clearly, when the system is uncontrolled, this measurement fluctuates wildly, which produces erroneous results, reducing the accuracy of the sensor system. It should also be noted that the detected magnitude of the vibration reaches a maximum when the second harmonic is minimized. This result verifies the theory presented in Chapter IV, Control Technique. With the controller active, the fluctuation in the MEMS actuation amplitude signal decreases and the remains constant through time. The noise present in this measurement is higher with the controller on, but this is most likely the result of the increased sensitivity of the sensor while locked onto the linear region of the second harmonic curve. The mean and standard deviations of each of these measurements are

shown in Table 4. The percentage change in the standard deviation of the MEMS device motion is -48.5%, while the mean increases by 42.3%. Therefore, the controller performs the goal of the system, which is increasing the sensitivity of the system while rejecting external noise sources.

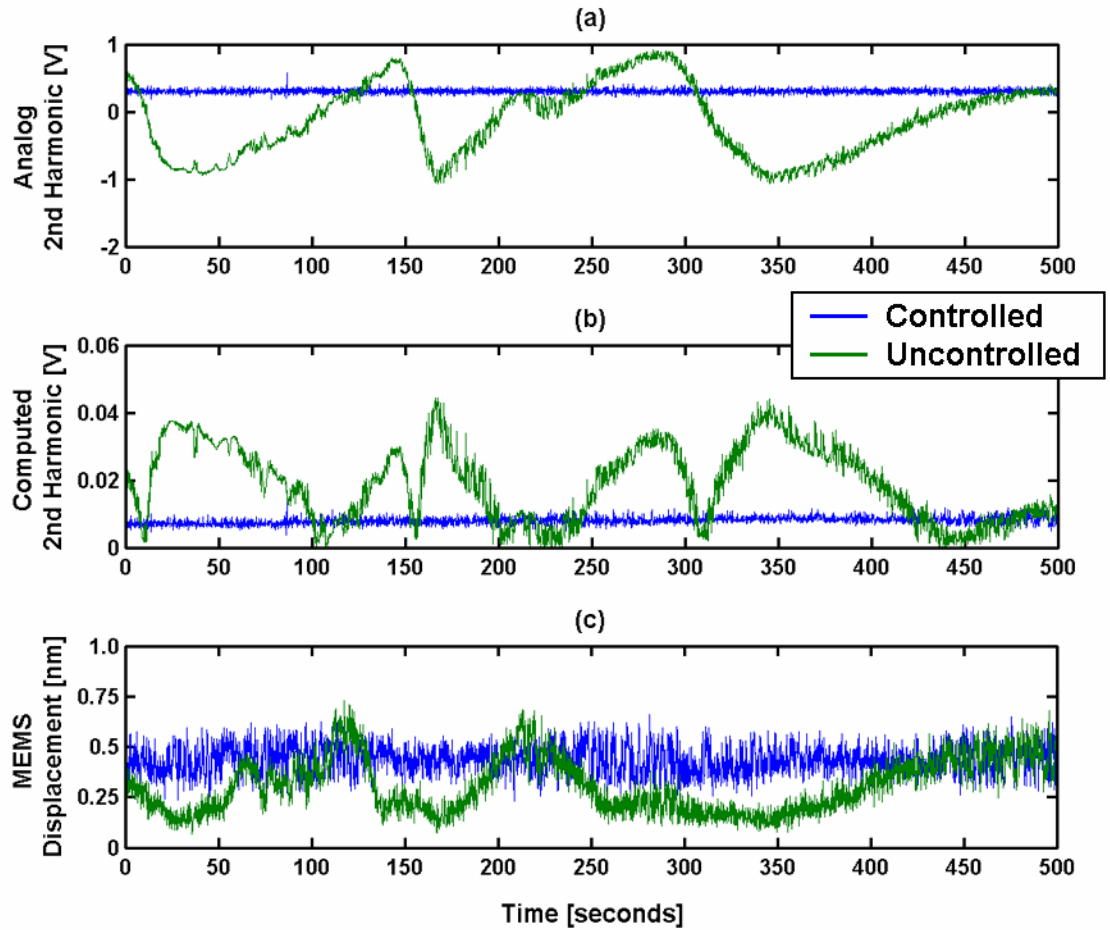


Figure 47. Analog 2<sup>nd</sup> harmonic signal (a), computed 2<sup>nd</sup> harmonic signal (b), and the MEMS displacement amplitude (c) over time with the controller on and with it off

Table 4. Results of controlled and uncontrolled signals over 500 seconds

Signal		700kHz MEMS actuation	FFT 2 <sup>nd</sup> Harmonic	Analog 2 <sup>nd</sup> Harmonic
Controlled	mean	<b>0.438nm</b>	0.0080 V	0.3037 V
	std	0.069nm	0.0010 V	0.0299 V
Uncontrolled	mean	<b>0.307nm</b>	0.0191 V	-0.1261 V
	std	0.134nm	0.0112 V	0.5300 V

### Case Study - cMUT

The controller used in this metrology system has been proven to actively control the position of the sample relative to the diffraction grating interferometer. This control allows for more accurate and better resolution scans. The system is used to measure the static and dynamic displacements of a sample microscale device, a capacitive micromachined ultrasonic transducer (cMUT). These devices are fabricated using well-known photolithography techniques. The devices can range in size from 50 $\mu$ m to over 1mm in diameter. These cMUTs are used as ultrasonic sensors as well as acoustic measurement devices. In addition, they can be forced to vibrate by applying a voltage to the capacitive conductors, allowing them to function as actuators. An SEM of a cMUT is shown in Figure 48.

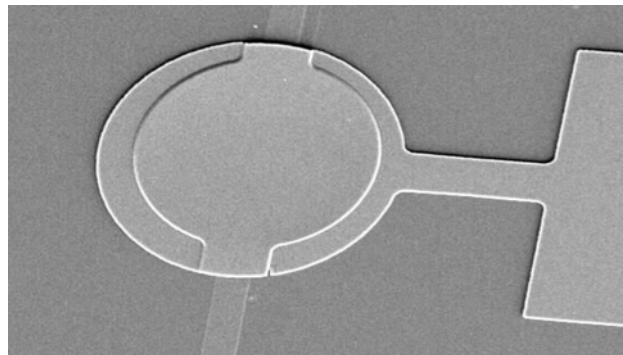


Figure 48. SEM of a cMUT

The devices utilize the electrostatic force generated between two parallel but oppositely charged conductors. The charge comes from a voltage potential difference between the two electrodes. One of these electrodes is a solid aluminum membrane over an open cavity, which is compliant and moves in response to this capacitive force. The other electrode consists of a patterned aluminum layer at the bottom of the cavity. This bottom electrode is known as the capacitive fingers of the cMUT. A schematic cross section of a cMUT is shown in Figure 49. In this design, the edge of the membrane is pinned, forming a circular drumhead configuration. The vibration profile of a thin circular membrane pinned at the edge is well known. In the first vibrational mode, the center of the membrane, point A in Figure 49, has the greatest displacement, and other points, such as B, has less displacement. The estimated deflection is highly dependent upon the sensitivity of the cMUT, which translates the pressure generated from the capacitive force into a deflection. This sensitivity may vary from membrane to membrane.

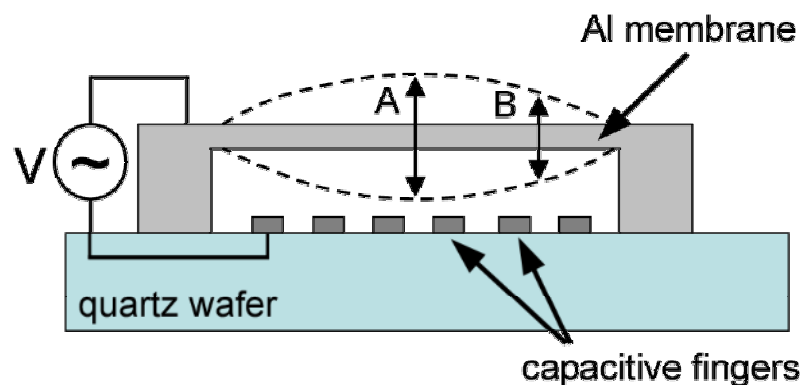


Figure 49. Schematic of cMUT in cross section



Characterization of this movement has been performed by a number of different techniques including white light interferometry and diffraction grating interferometry. The substrate of the cMUT is optically clear, and the capacitive fingers act like a diffraction grating, allowing a diffraction grating interferometer to be created from the backside of the membrane. However, the measurements derived using this technique only represent the average displacement of the membrane, and are not suitable for the creation of vibration maps over the surface of the cMUT. The approximate resonance frequency of the cMUT tested in this case study is 700kHz, which is well within the bandwidth of the sensor system.

### **Static Metrology of a cMUT**

The static height map of microscale device is extremely useful for fabrication process improvement. The layer thickness deposited during photolithography is critical for many MEMS applications, as are the etch depths and angles. Chapter II of this thesis presents a few technologies that exist for the three dimensional metrology of microscale devices. Currently, white light interferometry is one of the most common techniques used. Figure 50 shows a three dimensional image of the sample cMUT device generated from a Veeco white light interferometer. A cross section of this device is shown in Figure 51. In these images, the cMUT electrodes are under a static voltage difference of 40V, which pulls the membrane down toward the bottom electrode. The white light interferometer measures the amount of deflection that a cMUT undergoes as a function voltage applied. With 30V of actuation, the cMUT is deflected approximately 25nm and shows 55nm of deflection with 40V applied.

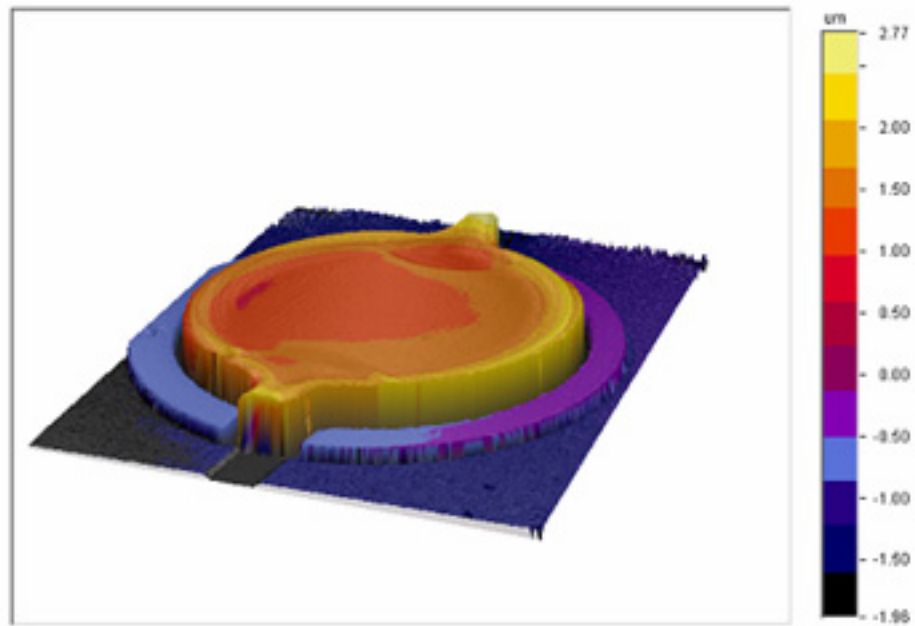


Figure 50. Three-dimensional image of a cMUT taken with a white light interferometer

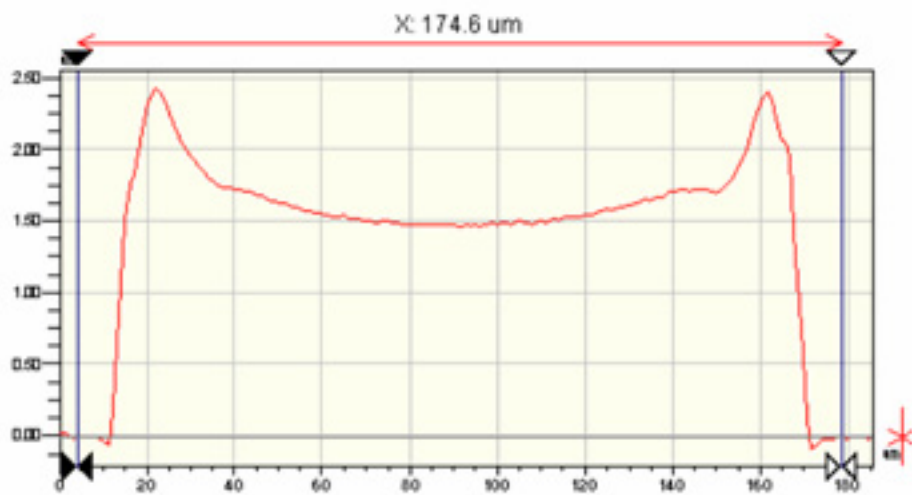


Figure 51. Two-dimensional cross section profile of a cMUT under 40V static actuation

Figure 52 shows the static height image of the same cMUT device generated from the diffraction grating interferometer system described in this thesis. It should be noted that when a step change of more than  $\lambda/4$  (157nm) occurs, the sensor produces erroneous results as the controller cannot adjust for step changes of this magnitude. Evidence of this phenomenon can be seen where the step change occurs between the outer electrode and the substrate. In Figure 52, it appears that this step change is approximately 75nm, whereas in Figure 50, it appears that this step measures around 750nm. Therefore, this type of measurement is only of use for quantifying the shape of relatively flat regions of the MEMS device with no significant step changes.

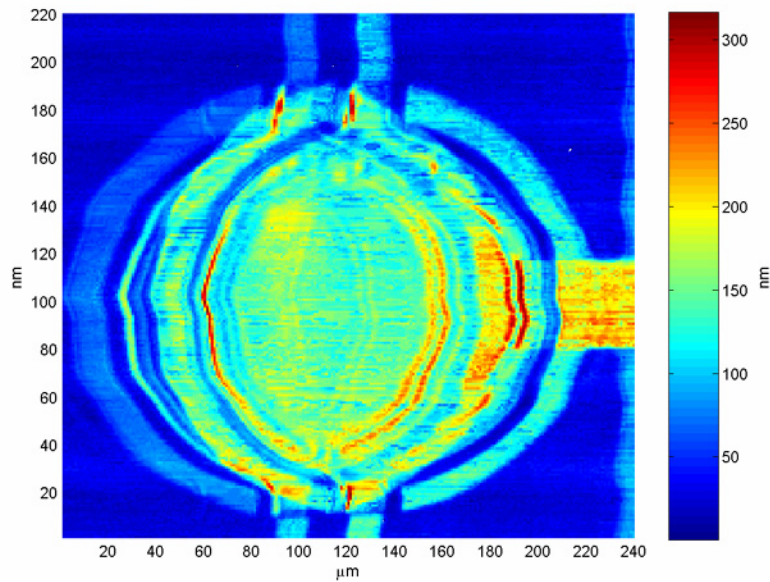


Figure 52. Static height map of a cMUT generated with the actively controlled diffraction grating interferometer

## **Optical Distortions in Imaging**

In Figure 52, a number of optical distortions appear in the image. Some of these aberrations stem from the nature of the optics shown in ray tracing diagram of Figure 32. The HeNe laser produces a spatially coherent collimated beam, which is reduced by the first convex lens. The beam is divergent when it intersects the diffraction grating and the microlens. This divergent beam which passes through a small focal length lens is distorted such that the flat wavefronts present in laser light become bowed and deformed. In addition to the distortion caused by the non-planar wavefronts, the microlens itself may contain aberrations, which further distort the beam and cause some coherence loss. When these distorted wavefronts interfere with each other, the resulting pattern is no longer ideal, and the interference intensity minimum will not be zero. This distorts the measurements taken by the system. Also, some beam steering issues may be present where the light emitted from the microlens is not normal to the surface of the lens.

Along with the aberrations present in the image, a distinct ghosting effect is present in the static metrology image. The image of the cMUT is repeated with an image of lesser intensity shifted by approximately  $30\mu\text{m}$  from the dominant image. The ghosting causes an overlap of the two interference intensities, and in some areas this may cancel out the signal entirely. In other areas, the intensities appear to be additive and a very large interference signal is detected. The ghosting effect is the result of multiple reflections between the sensor and the target surface, as shown in Figure 53. The angle of tilt between the sensor and the specimen,  $\theta$ , can be determined by the amount of shifting present, as the focal length of the sensor is known to be approximately  $800\mu\text{m}$ . This yields a tilt angle of around  $2^\circ$ . Attempts are made to reduce the ghosting effect by

adjusting the tilt angle; however, accurate adjustment of the tilt angle is difficult to accomplish and the overall interference intensity suffers as a result of the tilt adjustment. This causes a loss of resolution and fidelity of the dynamic measurements. The ghosting may also be the result of the aperture surrounding the microlens. This material may reflect the laser light from the surface and again cause multiple reflections. Therefore, the ghosting effect is due to the optical setup and design of the grating and microlens configuration.

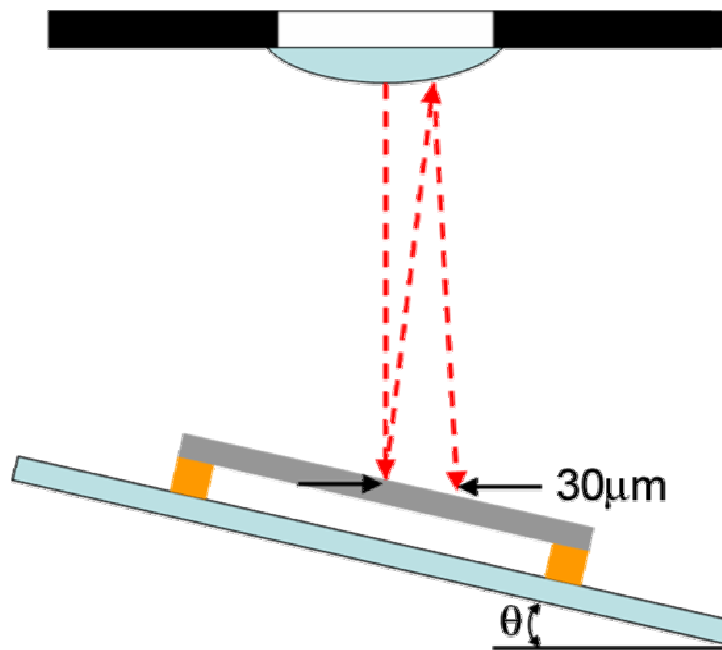


Figure 53. Diagram of sensor and specimen showing multiple reflections.

### **Dynamic Metrology of a cMUT**

In addition to the static metrology capabilities of the actively controlled diffraction grating interferometer, the sensor system also quantifies the amount of out-of-plane motion of MEMS devices. A few existing sensors that have this capability are discussed in Chapter II, but many are very costly and complex. The system analyzes the magnitude of the interference signal at the MEMS device actuation frequency, which correlates to the dynamic motion of the sample. The scaling of this correlation is calculated through the process described in Chapter V. Therefore, the voltage present in the narrow band around the actuation frequency is converted into a peak to peak motion measurement.

The motion of the cMUT is dependent upon the capacitive force generated between the electrodes, which are charged by a sinusoidal signal with a DC offset. Typically, the DC component of the signal is +40V, and the AC component is  $\pm 10V$ . An analytic model of the pressure generated from the voltage applied is presented in Equation (21), where  $\epsilon_0$  is the permittivity constant, and  $g$  is the gap between the electrodes of the cMUT (Hall, 2002). A sensitivity parameter translates the pressure into displacement, which for the particular membrane in this case study is 0.0375nm/Pa, assuming that the membrane is operating at the first vibrational mode frequency. Therefore, by applying Equation (21), the expected peak to peak motion of the cMUT due to the AC signal is 27nm.

$$P = \frac{\epsilon_0 V_{DC}^2}{2g^2} + \frac{\epsilon_0 V_{AC} V_{DC}}{g^2} \quad (21)$$

Figure 54 shows the vibration map of the cMUT vibrating near its natural frequency of 700kHz. The vibration amplitude has been scaled using Equation (20), which accounts for the varying reflectivity of the sample surface. The areas with very poor reflectivity have been trimmed out of this image by setting the amplitude to zero. The sensitivity of the linear range of sensor during this scan is 50nm per volt of photodiode signal as determined through the sensitivity procedure outlined in the previous chapter. Therefore, the maximum measured displacement is around 18nm, which is 33% lower than the analytically predicted value. This 9nm discrepancy can be attributed to the actuation of the cMUT at a frequency other than its peak response. Also, the gap height used in Equation (21) is critical to the estimated peak to peak motion of the membrane. A gap height of 2.2 $\mu$ m was assumed based on the design and fabrication of the cMUT, but a slight variance could account for a change in the deflection.

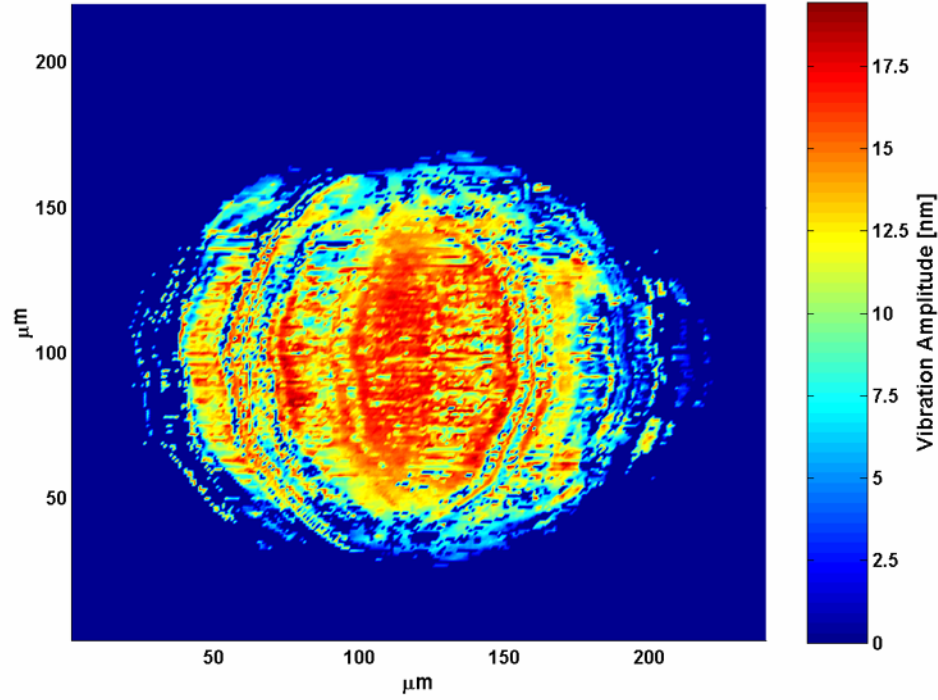


Figure 54. Vibration map of the surface of a cMUT

The circular cMUT is mechanically identical to a drum head, which consists of a thin skin stretched over a circular opening. Along with a primary vibration mode, higher order vibrational modes are also exhibited. In these other modes of vibration, the dynamic surface profiles differ from the fundamental mode. The shape and actuation frequency of these higher order modes are well known and can be analytically solved for using Bessel functions. Figure 55 shows another image of the cMUT vibrating at the first fundamental actuation frequency, and a finite element model of this mode shape is shown in Figure 56. Theoretically, the second actuation frequency is approximately 2.3 times the first fundamental vibration frequency. Therefore, for the cMUT in this case study, the second fundamental vibrational mode occurs at 1.77MHz. According to Lee *et al.* the photodetector used in this system has a bandwidth above 2MHz (Lee, 2003). An image



of the measured vibrational profile of a cMUT actuated at this frequency is shown in Figure 57 and a finite element model of the membrane vibrating at this frequency is shown in Figure 58.

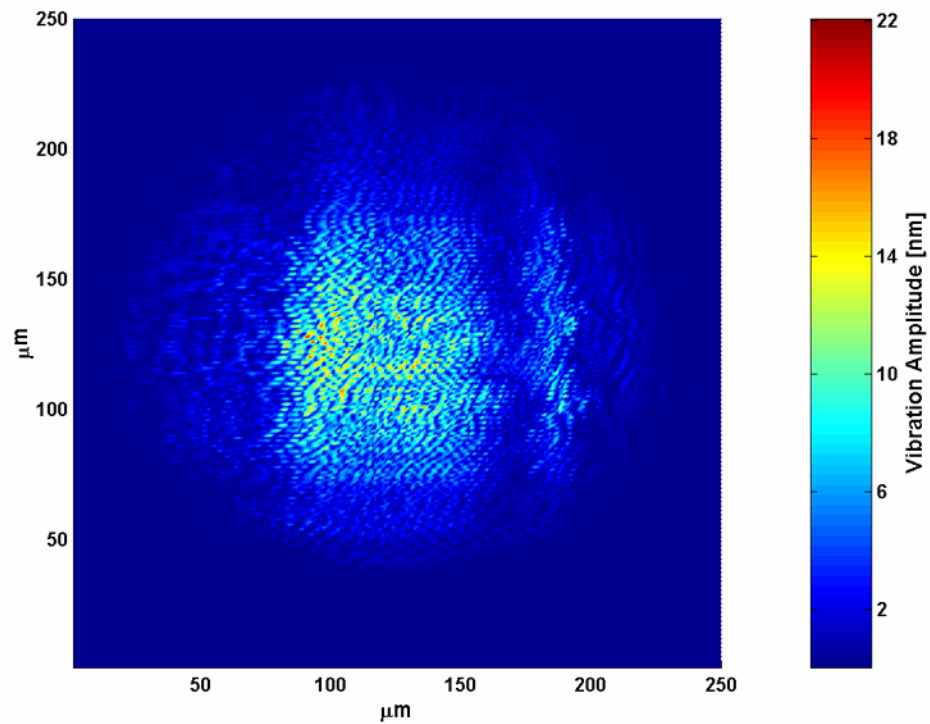


Figure 55. Vibration map of a cMUT actuated at the first fundamental vibration mode

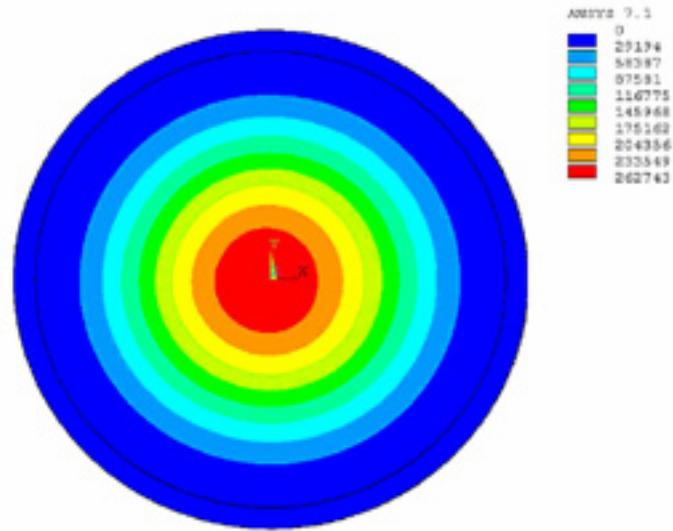


Figure 56. ANSYS finite element model of the cMUT membrane vibration amplitude at the first fundamental vibration mode

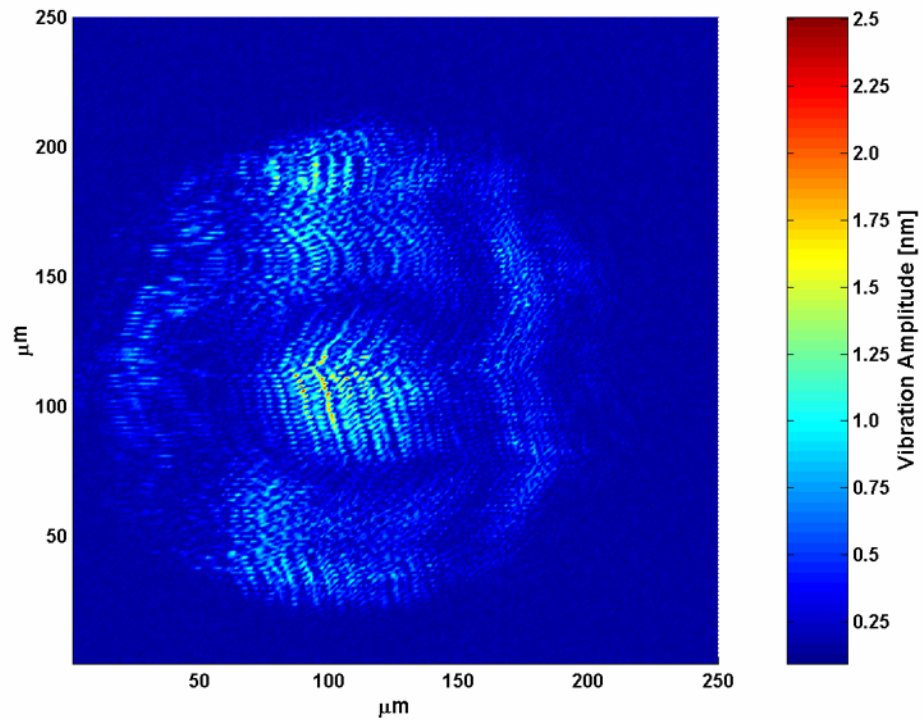


Figure 57. Vibration map of a cMUT actuated at the second fundamental vibration mode

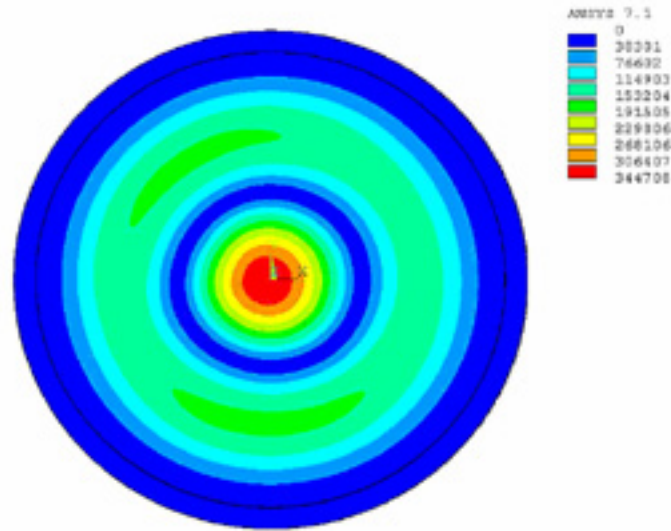


Figure 58. ANSYS finite element model of the cMUT membrane vibration amplitude at the second fundamental vibration mode

The circular node where no vibration is present is located at 0.436 times the radius of the circular membrane. Note that the two vibrating sections vibrate at  $180^\circ$  out of phase, meaning that when one is reaching its maximum positive displacement, the other portion is reaching its maximum negative displacement. However, this metrology system measures the vibration peak to peak amplitude, and, therefore, it would appear that the two sections are in phase, when they are not. A sample cross section of the second fundamental vibration mode map is shown in Figure 59. Compared to Figure 60, which shows a cross section of the first fundamental mode, the higher frequency actuation clearly has two points of zero vibration while having much less amplitude at its peak.

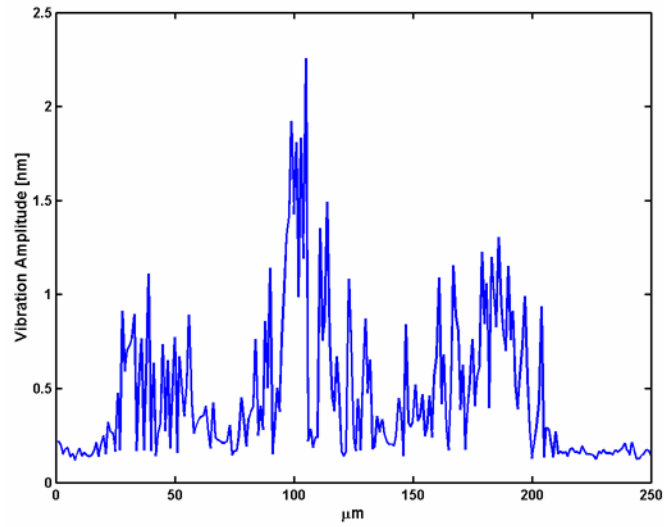


Figure 59. Cross section of the vibration map of a cMUT activated at the second fundamental mode

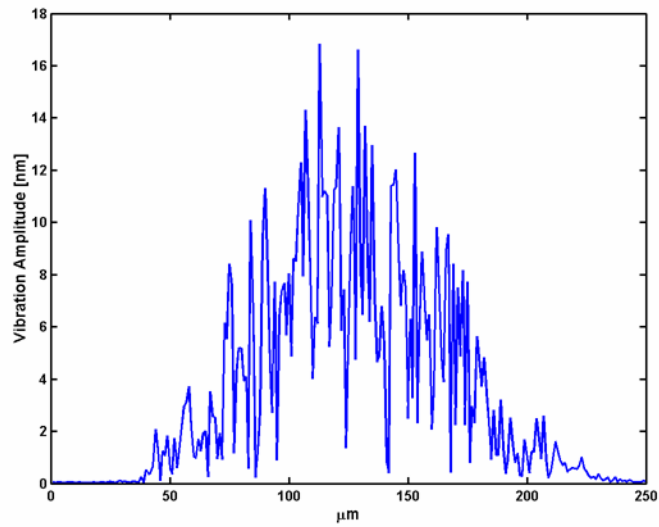


Figure 60. Cross section of the vibration map of a cMUT activated at the first fundamental mode

The active control of the diffraction grating interferometer has been shown to reduce the power present in the second harmonic of the modulation signal as well as increasing the signal to noise ratio of the MEMS device actuation signal. This translates to clearer and smoother surface maps. A major problem that affects the performance of the system is the presence of mechanical vibrations. These vibrations appear in the vibration surface maps as ripples or waves in the image, as shown in Figure 61, an uncontrolled static height map. With the controller activated, these mechanical vibrations are eliminated and the image becomes much more uniform (Figure 62). Figure 63 shows a side-by-side comparison of the static height measurement of a trace taken with the controller on (a) and with it off (b). The controller greatly increases the uniformity of the measurement across the length of the trace.

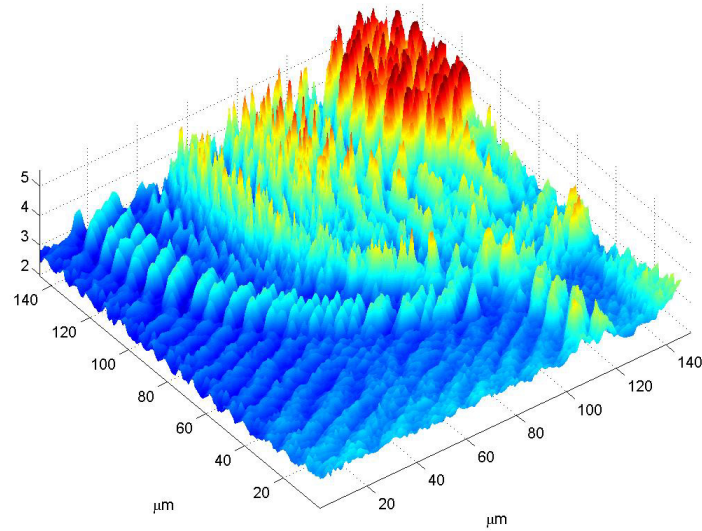


Figure 61. Static height map of a cMUT showing the mechanical vibration ripples that appear with the controller inactive

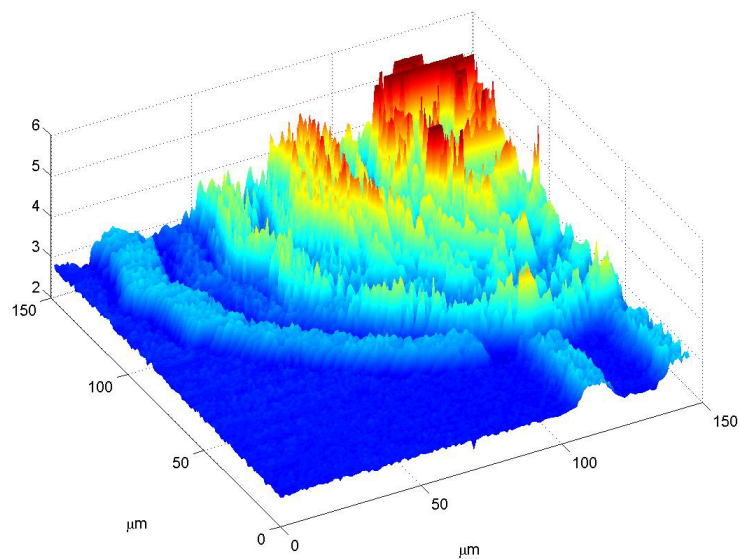


Figure 62. Static height map of a cMUT with the controller active, showing the lack of mechanical vibration ripples

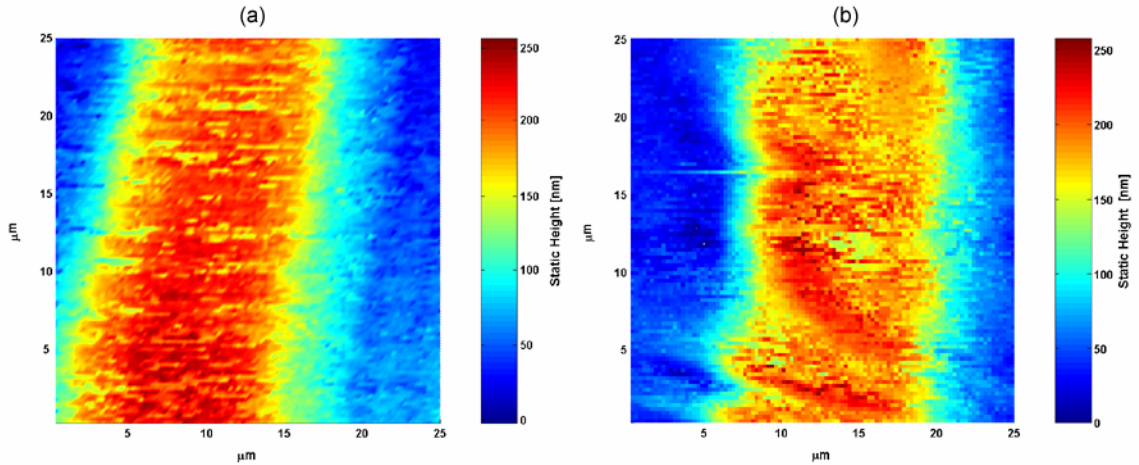


Figure 63. Static height map of a trace with the controller active (a) and inactive (b) showing the increase accuracy of the system under active control

### **Deformable Grating Sensor**

One of the primary goals of this project is to create an inexpensive, parallel non-contact measurement system capable of being integrated into the fabrication process for MEMS devices. A deformable diffraction grating sensor that eliminates the need for a piezoelectric transducer to adjust the path difference between the sensor and the sample has been fabricated. This diffraction grating sensor has an integrated photodetector placed at the location of the first interference order. Kim et al., have shown that this sensor is capable of deflection greater than a quarter wavelength of a HeNe laser (316nm) (Kim, 2004). A schematic of this setup is shown in Figure 64.

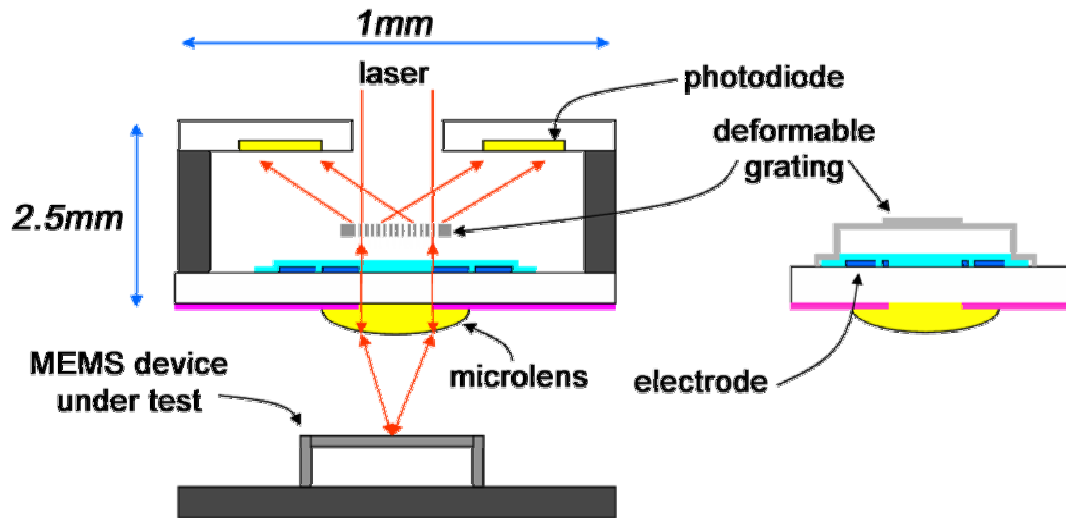


Figure 64. Schematic of the deformable diffraction grating sensor with integrated photodiode (Kim, 2004)

The small package size of this sensor allows it to be implemented in an array configuration. Sensors are arrayed such that they have the same spacing as the MEMS devices on the fabrication wafer, enabling the system to measure many MEMS devices simultaneously, greatly reducing the time and cost required to test the functionality of microscale devices.

The deformable grating has adequate gain characteristics to perform the control scheme described in this thesis. The roll-off of the gain of the sensor begins at around 1kHz and occurs at approximately 10dB per decade, as shown in Figure 65. The nominal gain value is around -35dB, and the -3dB bandwidth characteristic point occurs at around 35kHz. Therefore, a control loop implemented with the deformable grating is able to operate at and above 10kHz. The dynamics of this actuator and sensor device is significantly different from the PZT stack and diffraction grating shown in Figure 23. The deformable grating does not show the characteristic resonance peaks that the PZT



stack has and shows a frequency response that is very similar to a first order system. When the frequency increases above 250kHz, the first order response appears to give way to a higher order system, with a distinct resonance near 1MHz. Care is taken such that the control system and actuation of the deformable rating sensor avoids this range of frequencies. Applying the second harmonic analog locking PID control system to this sensor is currently an ongoing research topic.

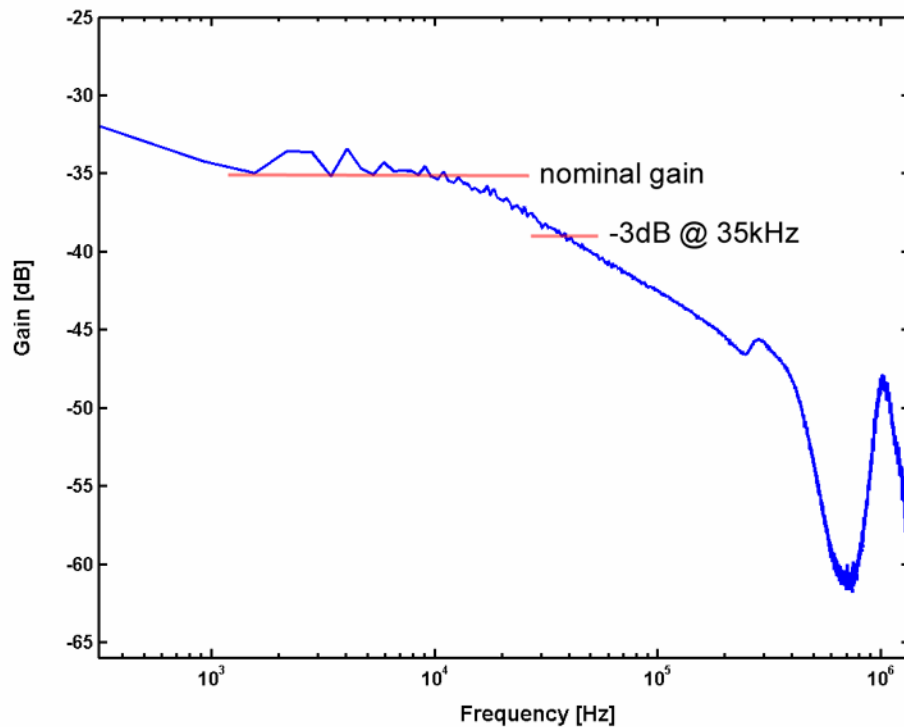


Figure 65. Gain response of the deformable grating sensor and actuator package

### **Two Sensor Parallel Implementation**

The nature of the FPGA processor is such that instructions may be carried out in a parallel fashion, which allows for many simultaneous operations to be performed in conjunction with one another. The FPGA is extremely flexible for reprogramming and

altering the control scheme. The LabVIEW FPGA toolkit is well suited to implement two control loops running in parallel on the FPGA. A copy of the original PID control loop is placed such that the two while loops are parallel to each other as shown in the screenshot in Figure 66. The loops are fully independent, and each one is set with its own distinct loop period. The limiting factor for placing multiple control loops is the amount of logic gates available on the FPGA processor.

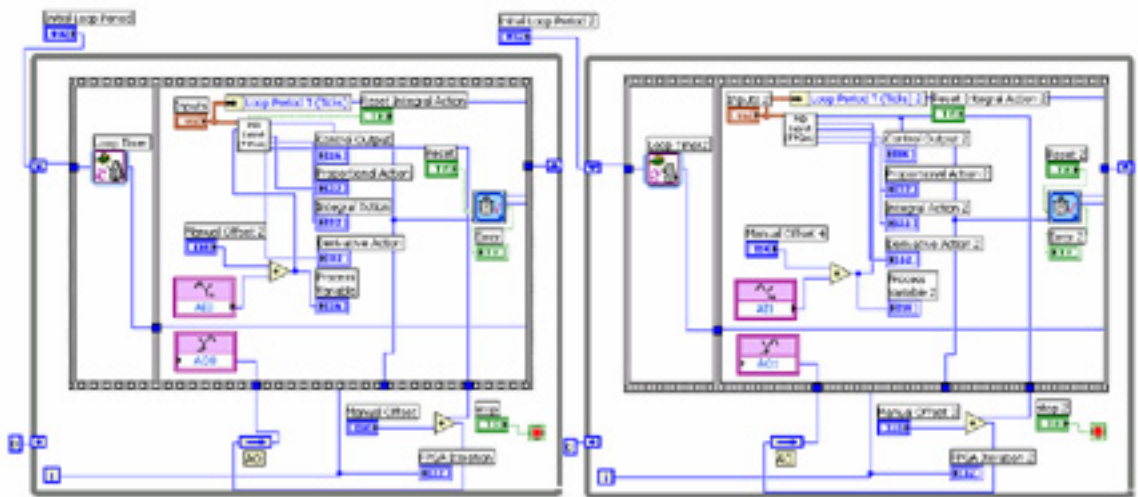


Figure 66. Screenshot of the LabVIEW block diagram of two parallel PID controllers implemented on the FPGA

Using the National Instruments PXI-7115 system, two fully customizable PID control loops are implemented. If the gains for each controller are known and hard-coded into the software, the number of loops that can be run simultaneously increases. The speed of each controller is not a function of the number of other controllers present. Rather, it is a function of the number of operations required to complete all the calculations within the loop. The FPGA processor is flexible such that different

controller types can be implemented simultaneously. For example, two PI controllers and a simple P controller can function in parallel and with different loop frequencies.

## CHAPTER VII

### CONCLUSIONS AND SUGGESTIONS FOR FUTURE WORK

#### Summary

Three-dimensional metrology of microscale parts is necessary to increase the yield of these devices and accelerate their market adoption. Currently, the yield for MEMS devices lags far behind other photolithography based products such as integrated circuits. A metrology tool capable of collecting both static and dynamic data over a wide frequency range is ideal for rapidly evaluating the performance of microscale fabrication techniques. Ideally, this sensor system should also be cheap and parallel in order to incorporate it into the fabrication process itself. This in-line metrology technique can serve as both a quality control technique as well as a fabrication process refinement technique.

This thesis describes the background literature, the theory, the construction, and the testing of an actively controlled diffraction grating interferometer, which serves as a macroscale proof-of-concept for a smaller highly integrated system. The proof-of-concept system measures the static and dynamic displacements of microscale parts. A case study of a sample microscale device is described. Also, preliminary work on the integrated deformable diffraction grating interferometer is presented.

The macroscale system utilizes a diffraction grating interferometer technique to produce the interference pattern. A piezoelectric transducer (PZT) is used to modulate the position of the sample, changing the path difference between the sensor and the sample. A control scheme which uses the constant modulation of the sample as a

feedback mechanism to insure that the metrology system remains in the most sensitive operating region is detailed. This scheme utilizes the second harmonic of the modulation signal as the process variable for a control loop. The second harmonic is proportional to the second derivative of the interference curve, and, therefore, when this signal is minimized, the sensor acts within its linear range.

Step response and frequency sweep response data verifies the analytic model of this electromechanical system. The transfer function of this lumped plant and sensor system is derived from this experimental data. A lag-compensator controller is proposed as a suitable controller for the desired system dynamics. A derivation of the closed-loop transfer function follows from the analytic models of the plant, sensor and controller.

A proportional-integrative controller that closely mimics the performance of the lag-compensator controller is implemented on a fixed-point field programmable gate array (FPGA) processor. The functional gains for this controller derive from the lag-compensator controller transfer function. Refinement of these gains is done through numerous techniques, and a methodology for tuning the PI controller is discussed. The control of this parameter increases the ratio between the power present in first and second harmonics, while slightly increasing the signal to noise ratio of the system. This indicates that the controller maintains the position of the sensor such that it remains in the highly sensitive linear region of the interference curve.

The hardware and software setup of the metrology system is presented. The physical setup consists of a laser, a diffraction grating and microlens, a photodetector and the sample, which is mounted to a three axis motorized linear stage system. The metrology system uses two separate software systems. The data recording and analysis

system controls the in-plane position of the sample, allowing surface maps of the specimen to be created. The algorithm for collecting and analyzing the data recorded by the analog to digital converter is presented. The programming system and user interface to the FPGA processor is addressed, including the ability to adjust all of the gain and timing parameters while the controller is running. This greatly improves the cycle time between controller adjustments.

Calibration of every experimental system is key to insuring that measurements are accurate. Methodologies for determining the focus of the lenses and calibrating based on surface reflectivity are presented. The metrology system specifications are explored including the bandwidth of the sensor and controller, as well as the in-plane and out-of-plane resolution of the system.

A case study utilizing a capacitive micromachined ultrasonic transducer (cMUT) is presented which shows the improvement that the active controller has on the fidelity of the metrology data generated. Surface maps of both the static and dynamic measurements show the capability of metrology system. Vibration profiles of the cMUT are shown for both the first and second fundamental vibration mode, which correlate well with analytic theory. Finally, images are presented of the cMUT which prove the increased performance of the sensor with active control.

## **Conclusions**

The original goal of creating a macroscale proof-of-concept diffraction grating interferometer with active mechanical control is achieved. The physical plant and sensor exhibit second order system dynamics, which allows a simple controller to be designed for the closed-loop system. This designed controller eliminates the steady-state error and

increases the system response time. Reduction of the power present in the second harmonic indicates that the control system keeps the sensor operating in the highly sensitive, linear range of the interference curve.

The metrology system described in this thesis achieves 0.25nm vertical resolution and 3.6 $\mu$ m horizontal resolution. The bandwidth of the sensor exceeds 2MHz, and vibration maps of the second fundamental vibration mode of a cMUT are created. The signal to noise ratio of the system has been measured to be 67dB, which is quite suitable for a wide range of applications. The adjustment of the path difference between the sensor and the sample improves the ability to generate uniform images through the rejection of mechanical vibrations. Thus, the control scheme achieves its goal of increasing the resolution and accuracy of the sensor system as a whole.

The optical setup and design of the system has shown to be flawed and aberrations in the images generated, such as the ghosting and distortions seen in every surface map presented in this thesis. Refinement of this design flaw is not within the scope of this thesis. The initial steps have been taken toward the creation of a microscale metrology system capable of array implementation. A deformable grating sensor which eliminates the need for a piezoelectric transducer is shown to have mostly first order system dynamics and an adequate gain margin for the implementation of a control loop. In addition work has begun on implementing two fully independent sensors in parallel on the FPGA processor.

### **Recommendations and Future Work**

The nature of the optical design is the most obvious problem that the work described in this thesis faces. Under the setup used, the wavefronts incident upon the diffraction grating are bowed, and, subsequently, optical distortion of the interference pattern occurs. In future iterations, care should be taken to insure that a small diameter, collimated beam strikes the grating surface. This will aid in the amplitude of the signal present in the diffraction order detected by the photodiode. Currently, the limitation for the microscale deformable grating sensor is the signal to noise ratio in the optical interference signal. Improvement must be made in this area in order to adequately utilize a controller with this system. In addition to the optical distortion problem, the reduction of the final spot size will allow for greater in-plane resolution of microscale devices.

Further improvements of the diffraction grating interferometer must come from the hardware used in the system. It is quite possible to extend the interferometer's static measurement capabilities beyond a half wavelength; however, in such a situation, a combination of actuators must be used. One such setup is the use of a PZT along with a deformable grating sensor. The PZT could perform the gross movement needed to adequately measure high aspect ratio MEMS devices, while the deformable grating could be used to eliminate the mechanical vibrations that plague and sub-nanometer resolution metrology system.

Also, the speed of the scanning can be dramatically increased. The largest contributor to the time required to create a surface map is the actuation of the motors. The current implementation utilizes a point to point measuring system. The motors and stages must come to a full stop before data is taken. This requires the motors to



accelerate, move, and then decelerate. Ideally, the lateral movement of the MEMS specimen should be constant and data taken as the device passes under the sensor. Higher precision linear stages with less vibration and backlash must be used in order to implement this feature properly.

The system described in this thesis shows the ability to generate surface maps of the static and dynamic motion of microscale devices. The resolution of the system is suitable for use as a process improvement tool. However, more progress must be made in the area of fast, non-contact metrology tools for microscale system. Metrology tools that have a large dynamic range and the ability to be implemented in an array fashion are crucial to improving the production yield of MEMS devices. This in turn reduces the cost of the MEMS components, increasing their market viability.

## APPENDIX A

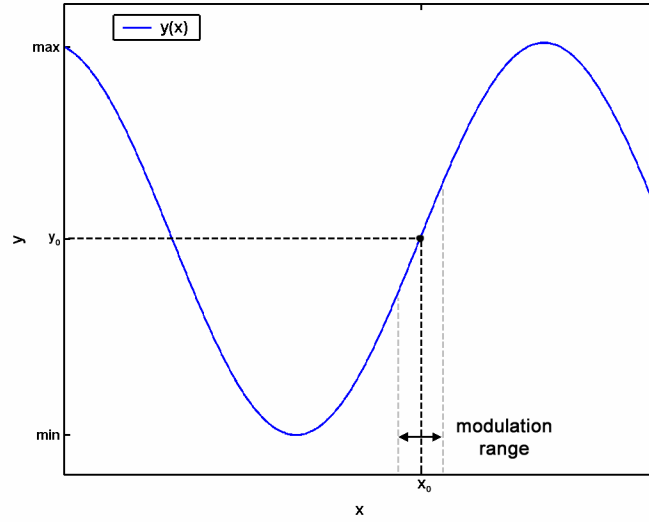


Figure 67. Interference curve showing set point and modulation range

From Equation (5),

$$I(x,t) = A \cos^2 \left( \frac{2\pi}{\lambda} (x + B \sin \omega t) \right)$$

More generally expressed as:

$$y(t) = f(x_0 + \sin(\omega t)) \quad \text{where } f \text{ is any continuous function}$$

Letting,

$$g(t) = x(t) - x_0$$

Expansion of the Fourier Series Analysis Equation:

$$F_k = \frac{1}{T} \int_T y(t) e^{-ik\omega_0 t} dt$$

The first two terms of Taylor Series Expansion of  $y(t)$ :

$$y(t) = \frac{dy}{dx} \Big|_{x_0} d(t) + \frac{1}{2!} \frac{d^2 y}{dx^2} \Big|_{x_0} d^2(t) + y_0$$

Gives the Fourier coefficients, which can be broken up into three terms:

$$F_k = \frac{1}{T} \int_T \left[ \underbrace{\frac{dy}{dx} \Big|_{x_0} g(t)}_{(1)} + \underbrace{\frac{1}{2!} \frac{d^2 y}{dx^2} \Big|_{x_0} g^2(t)}_{(2)} + \underbrace{y_0}_{(3)} \right] e^{-ik\omega_0 t} dt$$

Term (3) for all k:

$$F_{3k} = \frac{1}{T} \int_T y_0 e^{-ik\omega_0 t} dt = 0$$

Term (1) for all k:

$$F_{1k} = \frac{1}{T} \int_T \frac{dy}{dx} \Big|_{x_0} g(t) e^{-ik\omega_0 t} dt$$

Evaluated for k=1:

$$F_{11} = \frac{1}{T} \frac{dy}{dx} \Big|_{x_0} \int_T \frac{1}{2} \left[ e^{-i\omega_0 t} + e^{i\omega_0 t} \right] e^{-i\omega_0 t} dt = \frac{1}{2} \frac{dy}{dx} \Big|_{x_0}$$

Which proves that Term (1) is proportional to the first spatial derivative of y, when k=1 (the first harmonic). For all other k, Term (1) = 0 due to orthogonality.

Similarly, Term (2) is non-zero for k=2

$$F_{22} = \frac{1}{2!} \frac{d^2 y}{dx^2} \Big|_{x_0} \frac{1}{T} \int_T \frac{1}{4} \left[ e^{i2\omega_0 t} + e^{-i2\omega_0 t} \right] e^{-i2\omega_0 t} dt = \frac{1}{4} \frac{1}{2!} \frac{d^2 y}{dx^2} \Big|_{x_0}$$

Proving that Term (2) is proportional to the first spatial derivative of y, when k=2 (the second harmonic). By expanding the Taylor and Fourier Series to include more terms, this proof can be extended to all harmonics, and all derivatives.

## REFERENCES

- Ahola T., Hu, J., and Ikonen, E., "A digital control system for the iodine stabilized He-Ne laser," *Review of Scientific Instruments*, vol. 69, no. 5, pp.1934-1937, 1998.
- Beckwith, T., Marangoni, R., Lienhard, J., *Mechanical Measurements*, 5th Ed., Addison-Wesley Publishing Company, Reading, MA, 1995.
- Binnig, G. and Quate, C. F., "Atomic Force Microscope," *Physical Review Letters*, vol. 56, pp. 930-933, 1986.
- Davis, C. Freeman, D., "Using a Light Microscope to Measure Motions with Nanometer Accuracy," *Optical Engineering*, vol. 37, no. 4, pp. 1299-304, 1998.
- Fenyman, R. "There's Plenty of Room at the Bottom," *Journal of MEMS*, vol. 1. no. 1, pp. 60-66, 1992.
- Hall, N., Degertekin, L., "Integrated optical interferometric detection method for micromachined capacitive acoustic transducers," *Applied Physics Letters*, Vol. 80, pp. 3859-61, 2002.
- Hemmert, W., Mermelstein, M. S., Freeman, D.M., "Nanometer Resolution of Three-Dimensional Motions Using Video Interference Microscopy," *IEEE International MEMS99*, Orlando FL, January 17-21, 1999.
- Hornbeck, L., "Projection displays and MEMS: timely convergence for a bright future," *Proceedings of SPIE - The International Society for Optical Engineering*, vol. 2640, p 2, 1995.
- Humberstone, C., "Pseudo-Floating Point PID in FPGA," *National Instruments Corporation*, Austin, TX, 2003.
- Jordan, S., Lawrence, E. M., "Vibration nullification of MEMS device using input shaping," *Proceedings of SPIE - The International Society for Optical Engineering*, vol. 5052, pp. 326-334, 2003.
- JDS Uniphase Corporation, "Product Catalog", JDS Uniphase Corporation, San Jose, CA, 2003.
- Kim, B., Razavi, A., Degertekin, L., and Kurfess, T., "Microinterferometer for Noncontact Inspection of MEMS," *The 3rd International Workshop on Microfactories*, pp. 77-80, 2002.
- Kim, B., Schmittiel, M., Kurfess, T. Degertekin, L., "Deformable Diffraction Grating for Scanning Micro Interferometer Arrays," *Proceedings of 2004 SPIE Symposium on MOEMS Display and Imaging Systems*, Vol. 5348, pp. 98-107, 2004.

- Kim, B., Schmittiel, M., Kurfess, T. Degertekin, L., "Scanning Grating Microinterferometer for MEMS Metrology," ASME Journal of Manufacturing Science and Technology, submitted February, 2004, under review.
- Kim, B., "Miniaturized Diffraction Based Interferometric Distance Measurement Sensor," Ph.D. Thesis, Georgia Institute of Technology, Atlanta, GA, 2004.
- Kirkland, E. Liang, S., Kurfess, T., "A Nano Coordinate Machine for Optical Dimensional Metrology," First Humanoid, Nanotechnology, Information Technology, Communication and Control Environment and Management (HNICEM) International Conference, Manila, Philippines, March 29-31, 2003.
- Larrabee R., Postek M., "Parameters characterizing the measurement of a critical dimension," Proceedings of SPIE - The International Society for Optical Engineering, vol. CR52, pp. 2-24, 1994.
- Lee, W., Hall, N. Degertekin, F., "Micromachined Acoustic Sensor Array with Diffraction-Based Optical Interferometric Detection," Proceedings of SPIE Symposium on MOEMS Display and Imaging Devices, Vol. 4985, pp. 140-151, 2003.
- Madou, M., *Fundamentals of Microfabrication*, CRC Press LLC, Boca Raton, FL., 1997.
- Melles Griot Corporation, "Product Catalog", Melles Griot Corporation, Carlsbad, CA, 2002.
- Meyer, G. and Amer, N. M., "Novel Optical Approach to Atomic Force Microscopy," Applied Physics Letters, vol. 53, pp. 1045-1047, 1988.
- Michelson, A., "Determination experimentale de la valeur du metre en longuers d'ondes lumineuses," Trav. Mem. Bur. Int. Poids Mes, vol. 11, pp. 1-42, 1895.
- Murphree, J., Brzezinski, B., Parker, J., "Using a Fixed-Point Digital Signal Processor as a PID Controller," Proceedings of the 2002 American Society for Engineering Education Annual Conference & Exposition, Session 2359, Montreal, Canada, June, 2002.
- NEC / Tokin Corporation, "Multilayer Piezoelectric Actuator Datasheet," Vol. 03, Tokyo, Japan, 2003.
- Nichols, J., "Metrology of High Aspect Ratio MEMS," Ph.D. Thesis, Georgia Institute of Technology, Atlanta, GA, 2004.
- Ogata, K., *Modern Control Engineering*, Prentice Hall, Inc., Upper Saddle River, NJ, 1997.

Peggs, G., Lewis A., Oldfield S., "Design for a compact high-accuracy CMM," CIRP Annals - Manufacturing Technology, vol. 48, no. 1, pp. 417-420, 1999.

Polytec Corporation, "Manual for Vibrometer," VIB-MAN-3001-97-e01/01.

Rembre, C., Rishi, K., Muller, R., "Optical Measurement Methods to Study Dynamic Behavior in MEMS," Proceedings of SPIE - The International Society for Optical Engineering, vol. 4400, pp 127-137, 2001.

Shilling, M., "Two Dimensional Analysis of Mesoscale Parts Using Image Processing Techniques," Master's Thesis, Georgia Institute of Technology, Atlanta, GA, 2003.